New Applications and Challenges of GNSS Variometric Approach

A DISSERTATION PRESENTED
BY
GIORGIO SAVASTANO
TO
THE UNIVERSITY OF ROME "LA SAPIENZA"

IN PARTIAL FULFILLMENT OF THE REQUIREMENTS
FOR THE DEGREE OF
DOCTOR OF PHILOSOPHY
IN THE SUBJECT OF
INFRASTRUCTURES AND TRANSPORTS
SECTION: INFRASTRUCTURES AND GEOMATICS

THESIS ADVISOR: PROF. MATTIA GIOVANNI CRESPI
THESIS COADVISORS: DR. ATTILA KOMJATHY AND DR. AUGUSTO MAZZONI

UNIVERSITY OF ROME "LA SAPIENZA"
ROME, ITALY
FEBRUARY 2018

© 2018 - Giorgio Savastano
All rights reserved.

Thesis advisor: Prof. Mattia Giovanni Crespi Giorgio Savastano

New Applications and Challenges of GNSS Variometric Approach

Abstract

Global Navigation Satellite Systems (GNSS) are nowadays widely used in several technical and scientific activities. Since the early stages of development (mid 1980 s), given the high level of accuracy achieved in determining the coordinates of the receiver, it became clear that the extensive deployment of GPS stations all over the world would have improved many tasks in geodesy and geodynamics.

The use of GNSS signals is now not only limited to the estimation of the receiver's position, but it has eventually become a key instrument for ionospheric and tropospheric remote sensing studies, and for soil features (GNSS reflectometry). In particular, GNSS can be used to monitor the ionosphere at different time and space scales. On a global scale, GNSS signals are used to generate Global Ionosphere Maps (GIM) by measuring the total electron content from stations located around the world. On a regional scale, the same signals can be used to detect fast ionospheric disturbances, including those generated by natural hazards, such as tsunami and earthquakes.

The Variometric Approach is a processing algorithm for GNSS observations which allow a GNSS receiver to provide valuable real-time information in a stand-alone operative mode. This approach is based on single time differences of suitable linear combinations of GNSS carrier-phase measurements, using a stand-alone GNSS receiver and standard GNSS broadcast products (orbits and clocks corrections) that are available in real-time. This thesis investigates the possibility to apply the Variometric Approach to the monitoring of the ionosphere, in order to detect in real-time ionospheric disturbances generated by tsunami.

The first chapter of this thesis will serve as a preface to define fundamental concepts that we will refer to throughout the rest of this work.

The rest of this thesis is divided into two main parts. In the first part (chapter 2), we present some advances and applications of the VADASE (Variometric Approach for Displacements Analysis Standalone Engine) algorithm to estimate in real time ground velocities and displacements using stand-alone GNSS receivers. This algorithm was eventually appointed as an effective strategy to contribute to GNSS seismology. In this section we used the 2016 Meinong earthquake occurred in Taiwan as a case study and we estimated coseismic displacements and propagation properties of the surface waves in a real-time scenario using low-cost GNSS receivers.

The second part of this work (chapters 3, 4, and 5) is devoted to a new GNSS processing algorithm, VARION (Variometric Approach for Real-Time Ionosphere Observation), which is capable of estimating changes in the ionosphere's Total Electron Content (TEC) using stand-alone GNSS receivers in real time. In chapter 4, the effectiveness of VARION was proven on the following study cases: 2012 Haida Gwaii earthquake and tsunami event, 2015 Chile earthquake and tsunami event, 2013 U.S. East Coast meteotsunami event, and 2017 Mexico tsunami and geomagnetic storm events. Finally, some conclusions and relevant prospects for future VARION developments are outlined.

VARION may represent a significant contribution to science because the ionosphere is strongly coupled to the dynamics of the Earth's surface, neutral atmosphere, and geomagnetic field. In particular, these ionospheric perturbations can be used to detect in real time detection atmospheric gravity waves due to tsunamis.

During the NASA funded GNSS Tsunami Early Warning System 2017 workshop held in Sendai, Japan, July 25-27 2017, the VARION algorithm was appointed as the first real-time GNSS tsunami tracking and warning system based upon NASA's Global Differential GPS system.

Contents

Listing of figures

Sai ched’é la statistica? É na’ cosa
che serve pe fá un conto in generale
de la gente che nasce, che sta male,
che more, che va in carcere e che spósa.

Ma pé me la statistica curiosa
é dove c’entra la percentuale,
pé via che, lí, la media é sempre eguale
puro co’ la persona bisognosa.

Me spiego: da li conti che se fanno
seconno le statistiche d’adesso
risurta che te tocca un pollo all’anno:
e, se nun entra nelle spese tue,
t’entra ne la statistica lo stesso
perch’é c’é un antro che ne magna due.

Trilussa, *La statistica*.

Acknowledgments

In primis, vorrei ringraziare la mia famiglia e in particolare i miei fantastici genitori: Stella e Antonio, che nonostante le difficoltá nell'avermi lontano da casa, sono sempre rimasti incredibilmente positivi e presenti. Grazie per tutto quello che avete sempre fatto e che continuerete sempre a fare per me.

I would like to thank a new member of my family, Diane, for giving me the support and inspiration during the last year, for patiently listening to my speeches before all my presentations and for kindly correcting my English. You probably never imagined to become a GNSS/ionospheric expert. Thanks Diane, also for making LA more like my new home.

I would also like to thank my advisor and mentor, Prof. Mattia Crespi. Thanks for being for me a scientific and human model and for teaching me the most important thing of all: the "pleasure of finding things out". Also, thanks to my two coadvisors: Dr. Attila Komjathy, who made this collaborations between JPL and "La Sapienza" possible, I hope I will keep learning from you during the next years; and Dr. Augusto Mazzoni for being always willing to discuss GNSS topics, especially in front of a good glass of wine.

Finally, I would like to thank all my friends in Rome, in Pasadena and in Taiwan. Writing down a list of all of you will be impossible.

In the new era, thought itself will be transmitted by radio.

Guglielmo Marconi, 1931

1

Global Navigation Satellite System

This first chapter is devoted to GNSS (Global Navigation Satellite System) and it is split into 6 sections. The first one dives into the evolution of this satellite system from the origin (when just GPS was available) to the present day (a multi constellation system). Section 1.2 provides a description of the GNSS observables. This chapter also gives a physical description of the Earth's atmosphere 1.3 and explains the ionospheric effects on the GNSS signal 1.4. Section 1.5 describes the linear combinations of GNSS observables which will be used in the following chapters. The last section 1.6 describes the satellite orbits parameters and the algorithm used to compute the satellite position in real-time.

1.1 INTRODUCTION

GNSS is a set of artificial satellite constellations which are nowadays used for countless different applications. Generally speaking, these systems were designed to allow the instantaneous determination of position and velocity (i.e. navigation) and time of a generic user receiving signals broadcast by satellites which are set in orbit around the Earth.

The first system to be developed and deployed was the US NAVigation Satellite Time and Ranging (NAVSTAR) GPS. It was originally set up by the Department of Defense (DoD) of the United States (US) for military purposes. In a first stage, to prevent real-time use of GPS by non U.S. Army (including real-time civilian use), the GPS signals were scrambled by artificial satellite clock dithering (Selective Availability (S/A)) in such a way that only the military were able to fully exploit the system. Things changed on May 1^{st} 2000, when U.S. president Bill Clinton decided to turn off S/A by "pushing a button", tearing down the position accuracy from 100 meters to less than 10 meters and giving birth to commercial development of GPS.

Ever since the early stages of development (mid 1980s), given the high level of accuracy achieved in determining the coordinates of the receiver, it became clear that the extensive deployment of GPS stations all over the world would have improved many tasks in geodesy and geodynamics. At that time, the observations were typically acquired every 30 seconds (or with a lower rate) and the data were combined together to achieve one position solution per day. These solutions were then stacked in time series of coordinates and, as a matter of fact, they revealed as an invaluable tool to monitor long-period large-scale geophysical and geodynamical events such as crustal deformation, sea-level changes, post-glacial crustal rebound and coseismic and postseismic deformations. A meaningful breakthrough came in the mid and late 1990s, when the advances achieved in GPS receiver technology, together with the increased data storage capability, generated the possibility to acquire and store satellite observations with much higher (up to 20 *Hz*) sampling rates. As a consequence, conventional geodetic models were upgraded in order to analyze data at high sampling rates ($\geq 1\ Hz$) and to solve for the receiver position at every observation epoch. This allowed to observe for the first time the much faster shacking produced by surface waves (S waves) radiated from the earthquake source. This combination of events can be considered as the birth of GPS Seismology, which can be thought of as employing high-rate GPS data and solving for the real-time kinematic positions of the receiver. In recent years, several studies have demonstrated the effective use of GPS in estimating coseismic displacement waveforms induced by an earthquake with accuracies ranging from a few millimeters to a few centimeters. This contribution is particularly relevant as it supports the estimation of important seismic parameters (e.g. seismic moment and magnitude Mw) without the problems of saturation that commonly affect seismometers and accelerometers close to large earthquakes. These studies were developed mainly in post-processing, analyzing observations acquired during strong earthquakes. Then, well-known processing strategies (single Precise Point Positioning (PPP), and differential positioning) have been developed to reduce as far as possible the latency between earthquake occurrence and coseismic displacement waveforms estimation.

1.1.1 From GPS to GNSS

The wide success of GPS has led to the development of other similar systems operated from different countries. The ensemble of such systems is referred to as GNSS. The main reason for the development of alternative systems to GPS is to ensure access to GNSS signals that are not under the control of any single nation, with implications for the military in times of war and national emergencies, and for civilian institutions that have stringent requirements on guaranteed access to a sufficient number of GNSS signals at all times.

Nowadays, the list of global and regional satellite-based positioning systems displays a continuous growth. New GNSS, such as the European Galileo or the Chinese BeiDou, are going to join the already existing GPS and GLONASS constellations. Moreover, the Russian system is again fully operational with 24 active satellites ever since October 31, 2011. In addition, these systems are supplemented by Space-based Augmentation Systems (SBAS) (e.g. Wide-area Augmentation Systems (WAAS), European Geostationary Navigation Overlay Service (EGNOS) or Ground-based Augmentation Systems (GBAS).

1.2 GNSS Observables

This section reviews some of the most important aspects of the observation equations for pseudoranges and carrier phases. Generally speaking, and keeping in mind the differences between various GNSS, it is possible to say that all satellite transmissions are derived from a fundamental frequency which is made available by onboard atomic clocks. Any further detail about signal generation and modulation would be system dependent and is out of the scope of this work. For a detailed description of the signal structure of the Global Navigation Satellite System used in the present work (i.e. GPS, GLONASS and Galileo) it is possible to refer to [40], [28], [25].

GNSS observables are nowadays used for several applications. This chapter focus on positioning and ionospheric remote sensing applications.

Overall, the satellite based positioning concept is founded on the principle of "trilateration", which is the method of determining position by measuring distances to points of known position. In the case of GNSS, the known points would be the positions of the satellites orbiting around the Earth and the distances could be measured as the time difference between the receiver local clock and the atomic clock onboard a satellite, multiplied by the speed of light.

In principle, just three satellites are required in order to solve the system with three equations and three receiver's position unknowns (X_R, Y_R, Z_R). But in order to take into account the receiver local clock, a fourth unknown has to be introduced in the system. In fact, the process used to measure distances from GNSS satellites to receivers is similar to the one performed by a rangefinder. In particular, ranging methods without accurate time synchronization of the receiver are called pseudorange and are the one used in GNSS positioning. The main difference between the two instruments is that the GNSS receiver is a passive instrument and distances are measured as time difference between the receiver local clock and the atomic clock onboard a satellite multiplied by the speed of light. The accuracy required for time differences measurements is very strict, in fact an error of just $3.3 * 10^{-6}$ seconds on the travel time would leads to an error on the distance of about 1 km. For this reason, each satellite is equipped with an atomic clock which has a very well modeled drift and maintains the synchronization with the reference GPS time (the atomic time scale implemented by the atomic clocks in the GPS ground control stations and the GPS satellites themselves). It is not possible to maintain this synchronization also for the receivers clocks and a fourth unknown parameter δt_R (the receiver clock offset) is added in the system.

The GNSS based ionospheric remote sensing process is radically different from the GNSS positioning one. For GNSS positioning, all the satellites take part into the least square estimation process in order to obtain receiver positions or velocities. For GNSS ionospheric remote sensing, each satellite-receiver link is processed autonomously and provide independent time series of total electron content (see section 3.3 for a more detailed explanation). Also, each link senses a different region of the sky and each receiver observes a variety of different physical processes at the same time.

1.2.1 CODE PSEUDORANGE

The pseudorange between a generic satellite S and a generic receiver R is measured as the time difference between the epoch of signal transmission, tagged by the internal satellite clock (t^S), and the epoch of signal reception, tagged by the internal receiver clock (t_R). This difference is then multiplied by the speed of light (c) to obtain a measure in length units (meters). Practically speaking, the satellite sends its clock time by multiplying the carrier phase by a known sequence of $+1$ and -1 (i.e. the so called "pseudorandom code"). The receiver internally generates an identical replica of the code and performs a cross-correlation with the incoming signal to compute the time shift necessary to align the two codes. This time difference, multiplied by the speed of light, gives the pseudorange measurement.

By assuming a reference common time system for satellite and receiver clocks, both ones suffer a delay, δt^S and δt_R respectively, with respect to the common time system. Assuming the signals are traveling in the vacuum, the pseudorange observation equation can be obtained as:

$$P_{iR}^{S}(t) = c(t_R + \delta t_R - t^S - \delta t^S) \tag{1.1}$$

where P_R^S is the pseudorange between the satellite and the receiver, i is the frequency of the carrier phase used to modulate the code, t_R is the time tag of the receiver clock, δt_R is the delay of the receiver clock from the reference time system (i.e. receiver clock error), t^S is the time tag of the satellite clock, δt^S is the delay of the satellite clock from the reference time system (i.e. satellite clock error), and c is the speed of light.

The difference $\Delta t = t_R - t^S$ is the true signal travel time and, if multiplied by the speed of light, returns the geometric distance $\rho_R^S(t)$ between the position of the satellite at epoch t^S and the position of the receiver at epoch t_R

$$\rho_R^S = \sqrt{(X_R - X^S)^2 + (Y_R - Y^S)^2 + (Z_R - Z^S)^2} \tag{1.2}$$

where X_R, Y_R, Z_R and X^S, Y^S, Z^S are the coordinates of the receiver and the satellite, respectively. Hence, the final pseudorange equation for a signal propagating in the vacuum reads as follows

$$P_{iR}^{S}(t) = \rho_R^S(t) + c(\delta t_R - \delta t^S) \tag{1.3}$$

1.2.2 PHASE PSEUDORANGES

Phase observable results from the difference between the phase of the incoming carrier wave (upon which the code is modulated) and the phase of a signal internally generated by the receiver which is synchronized with the receiver clock [11]. If the recording starts at epoch t_0, the receiver is capable to measure only the fractional part of the carrier phase that arrives from the satellite. Hence, the integer number of cycles between the satellite and the receiver at the initial epoch t_0 (the so called "integer ambiguity" N) is unknown. In unit of cycles the carrier phase observable reads as follows

$$\Phi_{iR}^{\ S}(t) = \frac{f_i}{c}\rho_R^{\ S}(t) + N_{iR}^{\ S} + f_i(\delta t_R - \delta t^S) \tag{1.4}$$

where i is the frequency index of the carrier wave, Φ_R^S is the phase observation between satellite S and receiver R, c is the speed of light, ρ_R^S is the geometric distance between the position of the satellite at epoch t^S and the position of the receiver at epoch t_R, N_R^S is the integer ambiguity and δt_R and δt^S are the receiver clock and the satellite clock errors, respectively. The carrier phase can be scaled to length unit multiplying Eqn. 1.5 by the wavelength of the carrier wave i, $\lambda_i = c/f_i$. The final carrier phase equation for a signal propagating in the vacuum reads as follows

$$L_{iR}^{\ S}(t) = \rho_R^{\ S}(t) + \lambda_i N_{iR}^{\ S} + c(\delta t_R - \delta t^S) \tag{1.5}$$

The integer ambiguity $N_{iR}^{\ S}$ refers to the first epoch of observations t_0 and remains constant during the period of observations if the tracking of the satellite is continuous (i.e. without loss of lock). Hence, the generic carrier phase observation at epoch t is given by

$$\Phi_{iR}^{\ S}(t) = \Delta\Phi_{iR}^{\ S}(t)|_{t_0}^{t} + N_{iR}^{\ S} \tag{1.6}$$

where $\Delta\Phi_{iR}^{\ S}$ is the (measurable) fractional part of the carrier phase at epoch t augmented with the integer number of cycles passed from the initial epoch t_0.

The carrier phase observation (Eqn. 1.6) is about 100 times more precise than the code pseudorange. However, the major drawback of the carrier phase observation stands in the integer ambiguity, which should be resolved exactly (using the so called "ambiguity resolution" techniques) to achieve the best possible accuracy in geodetic positioning.

1.3 STRUCTURE AND SUBDIVISION OF THE ATMOSPHERE

Before writing the remaining terms of the GNSS observation equations 1.3 and 1.5, it is necessary to describe the characteristics of the Earth's atmosphere.

The Earth's atmosphere is categorized into different layers according to their physical properties and influences onto the electromagnetic waves. With respect to the electromagnetic structure, the atmosphere is divided into the neutral atmosphere (or *troposphere*) and the *ionosphere*.

1.3.1 THE TROPOSPHERE

The troposphere, the gaseous atmosphere where the daily weather takes place, is heated from the Earth's surface. For this reason, the troposphere is warmest at the bottom and it is coldest at its top, where it meets up with the layer above (the stratosphere) at a boundary region called the tropopause. When a weather phenomenon called "temperature inversion" occurs, temperature in some part of the troposphere gets warmer with increasing altitude, contrary to the normal situation. Typically, the temperature drops about $6.5^o\ C$ with each increase in altitude of 1 kilometer. Horizontal temperature gradients are only a few degrees/100 km. Charged particles are virtually absent. The uncharged atoms and molecules are well mixed, and thus the troposphere is practically a neutral gas. The index of refraction is slightly greater than 1. It decreases with increasing height and becomes nearly 1 at the upper limit of the troposphere, corresponding to the continuously decreasing density of the medium. Nearly 90% of the atmospheric mass is below 16 km altitude, and nearly 99% is below 30 km [50]. For electromagnetic waves in the radio-frequency spectrum the troposphere is not a dispersive medium. The index of refraction does not depend on the frequency; it depends on air pressure, temperature, and water vapor pressure. Because of the dynamic behavior of tropospheric conditions it is difficult to model the index of refraction.

1.3.2 The ionosphere

1.3.2.1 History

The history of the discovery of the ionosphere is intimately connected with the history of radio wave propagation, and with Guglielmo Marconi's life. Marconi was expired by Hertz's work on radio waves and he was just 20 years old when he carried out valuable experiments at home on the transmission and reception of Hertzian waves. Marconi was obsessed by the idea of transmitting signal using these waves and on December 12, 1901, he maid an historic announcement: he received the first trans-Atlantic radio signal in St. John's, Newfoundland (now in Canada) using a 152.4 m (500 ft) kite-supported antenna for reception. The transmitting station in Poldhu, Cornwall, used a spark-gap transmitter to produce a signal with a frequency of approximately 500 kHz and a power of 100 times more than any radio signal previously produced. The message received was the Morse code for the letter S.

It is interesting to notice that even Marconi was not able of providing a convincing explanation for his experiment. The scientific community was debating on how this electromagnetic waves, which travels in straight lines, could have been detected by Marconi on the other part of the Earth. In fact, during his lecture at the Royal Institution in London entitled "Wireless telegraphy" of 2 February 1900 (this was nearly two years before the transatlantic experiment), in referring to some transmission experiments which he had carried out in England over a sea path of 85 miles, Marconi noted that owing to the Earth' s curvature there was between the transmitter and the receiver a "hill of water" (as he put it) 1000 feet high, and he commented that if the Hertzian waves travelled in straight lines the signals would not have been received, so the curvature of the Earth is no obstacle to the transmission and the Hertzian waves must either go over or round the dome of water or pass through it.

In other words, Marconi have not realized yet that he had just discovered the ionized region of the atmosphere, now known as ionosphere, capable of reflecting electromagnetic waves.

In the first year after G. Marconi's experiment in 1901, some pioneers of wireless communication, such as A. E. Kennelly, O. Heaviside and J. Erskine-Murrey, designated the upper atmospheric region which supposedly played a part in long distance radio transmission as the "upper reflecting surface" or the "conducting layer".

On the evening of Thursday, 11 December 1924, Marconi gave his inaugural lecture in London as President of the Royal Society of Arts and made the remark, "it is my belief that the whole theory and practice of long-distance wireless communication is just now undergoing a most important and radical change". Little did he know that on that very same Thursday evening, indeed perhaps at that very hour, Appleton and Barnett were on their way to Oxford to set up the receiving equipment for their historic experiment to be carried out on the following night which would indeed initiate the "era of the ionosphere."

As a matter of fact, the term "ionosphere" was suggested by Watson-Watt and E. V. Appleton in place of what had been loosely termed the "upper conducting layer" on November, 1926.

1.3.2.2 GEOPHYSICS

In order to provide a good description of the ionosphere, we need to briefly introduce the concept of *plasma*. Let us suppose to increase the temperature of a solid. If the temperature exceeds a certain value (which depends on the characteristics of the solid), the crystalline lattice structure will be destroyed and the solid will become a liquid. If we furthermore increase the temperature of the liquid, than the kinetic energy of the atoms will increase and subsequently also the distance between atoms will increase, until the liquid will turn into a gas. Solid, liquid and gas are the three states of matter that everyone knows. If we keep increasing the temperature (e.g. $T \geq 10000\ K$), the kinetic energy of the gas atoms will become so high that when they collide, the electrons would be stripped away. *Plasma*, the fourth state of matter, becomes a collection of ions and electrons. In other words, a plasma is an ionized gas formed because of the temperature of the gas is sufficiently high that the electrons can be stripped away from atoms. Plasma is an ionized gas that is *globally neutral* and that displays *collective effects*.

The ionosphere is a plasma. It represents the electrically charged component of the higher atmosphere. It can be characterized by the evolution of the free, neutral, and charged particles, as a function of the time of day. The ionization of the ionosphere is caused by solar and cosmic radiation. It lies 75-1000 km above the Earth. Because of the high energy from the Sun and from cosmic rays, the atoms in this area have been stripped of one or more of their electrons, or "ionized", and are therefore positively charged. The ionized electrons behave as free particles. The Sun's upper atmosphere, the corona, is very hot and produces a constant stream of plasma and UV and X-rays that flow out from the Sun and affect, or ionize, the Earth's ionosphere. Only half the Earth's ionosphere is being ionized by the Sun at any time.

1.3.2.3 THE EFFECTS OF IONOSPHERE ON RADIO SIGNAL

Because it is a plasma, the ionosphere has a strong influence on electromagnetic wave propagation. The plasma frequency is the low-frequency cutoff for radio wave propagation and depends on the local electron density n_e as

$$\omega_p = \left(\frac{n_e e^2}{m_e \varepsilon_0} \right)^{0.5} \tag{1.7}$$

where e, m_e are the electron charge and mass, ε_0 is the permittivity of vacuum. Typical ionospheric plasma frequency range from 1 to 20 MHz and the maximum occurs at the maximum of ionization.

Ionospheric sounding techniques are based on measurements of either the reflection of radio waves below the maximum plasma frequency or the refraction delay of higher-frequency signals transmitted across the ionosphere from satellites (e.g. GNSS).

It is important to highlight that the ionosphere is a dispersive medium with respect to the GNSS radio signal. Dispersion is the dependency of the phase velocity and, thus, of refraction, on the frequency. If dispersion occurs, a medium is called dispersive, e.g., the ionosphere is a dispersive medium at 1.5 GHz, while the troposphere is not. This means that the ionospheric effect on GNSS signal is frequency-dependent.

In a dispersive medium, the phase velocity differs from the group velocity. The group velocity describes the velocity of the envelope of a group of electromagnetic waves. The ionized gases in the ionosphere cause the phases of the electromagnetic waves to shift. The phase advance leads to a phase velocity greater than the speed of light. This does not contradict Einstein's postulate of the universal characteristic of the speed of light, since no information is transmitted by a single electromagnetic wave. The phase advance and the group delay are equal in size but different in sign. Practically speaking, code pseudoranges become longer and phase pseudoranges get shorter [7].

1.3.2.4 THE IONOSPHERIC LAYERS

The ionosphere has major importance to us because, among other functions, it influences radio propagation to distant places on the Earth, and between satellites and Earth. The generation of ions and electrons is proportional to the radiation intensity of the sun, and to the gas density. A diagram indicating the number of ions produced as a function of height shows a maximum in ion production rate. Such a diagram is called the Chapman-profile.

The ionosphere is composed of three main parts, named for historical reasons: the D, E, and F regions. The altitude and thickness of these three regions vary with time:

- D region: it represents the inner layer extending from 50 to 90 km; due to its small electron density (about 10^3 $electrons/cm^3$) this region does not reflect, but it strongly attenuates the average radio frequency waves (MF or MW), therefore below 3 MHz. The presence of this region in the atmosphere is strictly correlated with the incidence of solar radiation (α hydrogen Lyman radiation). Thus, the D region disappears during the night compared to the daytime.

- E region: this layer extends from about 90 to 150 km above Earth's surface with maximum electron density equal to $5 * 10^5$ *electrons*/*cm*^{3}. Solar radiation highly influences E region's extension, which becomes weakened during nighttime.

- F region: it is the highest region of the ionosphere (150-1000 km altitude) and also the most ionized (up to about 10^6 *electrons*/*cm*^{3}). Contrary to the other layers it exists during both daytime and nighttime. During the day it is ionized by solar radiation, during the night by cosmic rays. During daylight hours, it is almost always divided into two sub-regions, called F1 layer (about 200 km height, with a maximum electron density up to $5 * 10^5$ *electrons*/*cm*^{3}) and F2 layer (from 200 to 1000 km height).

- Besides these four regions, there is often a thin layer, located near the F region, called sporadic E layer (symbol E_s, whose general characteristics are extremely irregular.

The impact of the state of the ionosphere on the propagation of GNSS signals is represented by the quantity *sTEC* (slant total electron content):

$$sTEC = \int_R^S n_e(s) ds \tag{1.8}$$

where n_e is the electron density with the unit [*number of electrons*/m^3]. The integral contains the total number of electrons that are included in a column with a cross-sectional area of 1 m^2, counted along the signal path s between the satellite S and the receiver R. The unit of measurement of sTEC is the TECU (*Total Electron Content Unit*):

$$1\ TECU = 1\ *\ 10^{16}\ el/m^2$$

We assume that the highest ionospheric delay's contribution comes from the F2 region of the ionosphere, where the electron density is maximum. For this reason, the sTEC observation is defined by the intersection between the satellite-receiver line-of-site and a plane located at the height of F2 peak. This point is called ionospheric pierce point (IPP). In other words the sTEC value, which is an integrated quantity, is collapsed into one point. Ionospheric remote sensing using GNSS observations depends on the time and space evolution of the IPP.

1.4 Atmospheric Delays

So far, we considered signals propagating in the vacuum (see Eqn.s 1.3 and 1.5). However, we learned that GNSS signals propagate through atmospheric regions (troposphere and ionosphere) of different nature and variable state, and thus experience different kind of delays. Perturbations may occur to the direction of propagation, to the velocity of propagation and to the signal strength. For positioning application in satellite geodesy the atmosphere introduces unwanted perturbations. The main impact on the observational results are, in many cases, due to the ionosphere. Consequently, ionospheric influences have to be eliminated directly by measurements (ionosphere-free combination see section 1.5.1) or through corrections [44]. On the other hand, information on the state of the ionosphere can be obtained by retrieving the ionospheric delay in the GNSS signals (geometry-free combination see section 1.5.2).

To consider these terms in the code and the phase observations it is necessary to revise Eqn.s 1.3 and 1.5 as follows:

$$P_{iR}^{S}(t) = \rho_{R}^{S}(t) + c(\delta t_{R} - \delta t^{S}) + T_{R}^{S}(t) + \Delta_{igr}^{Iono}(t) \tag{1.9}$$

$$L_{iR}^{S}(t) = \rho_{R}^{S}(t) + \lambda_{i} N_{iR}^{S} + c(\delta t_{R} - \delta t^{S}) + T_{R}^{S}(t) + \Delta_{iph}^{Iono}(t) \tag{1.10}$$

where T_R^S is the tropospheric delay, Δ_{gr}^{Iono} and Δ_{ph}^{Iono} are the ionospheric delay due to ionospheric refraction.

1.4.1 THE IONOSPHERIC REFRACTION

As shown in Eqn. 1.7, electromagnetic waves having frequency greater than 20 *MHz* propagate through the ionosphere, although the ray path is still influenced by it. The ionospheric refraction is modeled as a function of the electron density represented by the total electron content (TEC). The TEC is influenced by the solar activity, diurnal and seasonal variations, and the Earth's magnetic field.

Following ([24]: p. 54), the series

$$n_{ph} = 1 + \frac{c_2}{f^2} + \frac{c_3}{f^3} + \frac{c_4}{f^4} + \ldots \tag{1.11}$$

approximates the phase refractive index. The coefficients c_2, c_3, c_4 do not depend on frequency but on the quantity n_e denoting the number of electrons per cubic meter (i.e., the electron density) along the propagation path. Using an approximation by cutting off the series expansion after the quadratic term, that is

$$n_{ph} = 1 + \frac{c_2}{f^2} \tag{1.12}$$

differentiating this equation leading to

$$dn_{ph} = -\frac{2c_2}{f^3} df \tag{1.13}$$

and substituting 1.12 and 1.13 into the equation from [7]: p. 118:

$$n_{gr} = n_{ph} + f\frac{dn_{ph}}{df} \tag{1.14}$$

which links the phase with group refractive index leads to

$$n_{gr} = 1 - \frac{c_2}{f^2} \tag{1.15}$$

It can be seen from 1.12 and 1.15 that the group and the phase refractive indices deviate from unity with opposite sign. Eqn.s 1.12 and 1.15 also indicate that the group and phase refractive index, and thus the time delays of signal propagation, are proportional to the inverse of the squared frequency and that higher frequencies are less affected by the ionosphere. Hence, GNSS constellation transmits data on two frequencies (e.g. GPS: L_1 and L_2) so that, at least to the first order, the effect of ionospheric refraction on positioning is eliminated by a particular combination of dual-frequency phase or code observations (ionosphere-free combination).

With an estimate for c_2 ([24]: p. 54),

$$c_2 = -40.3\, n_e \qquad [Hz^2] \tag{1.16}$$

the relation $n_{gr} > n_{ph}$ and, thus, $v_{gr} < v_{ph}$ follows because the electron density n_e is always positive. As a consequence of the different velocities, a group delay and a phase advance occur. In other words, GNSS ranging codes are delayed and the carrier phases are advanced. Therefore, the measured code pseudoranges are too long and the measured carrier phase pseudoranges are too short compared to the geometric range between the satellite and the receiver. The amount of the difference is the same in both cases.

According to Fermat's principle, the measured range s is defined by

$$s = \int n ds \tag{1.17}$$

where the integral must be extended along the real path of the signal. The geometric range s_0 along the straight line between the satellite and the receiver may be obtained analogously by setting n = 1:

$$s_0 = \int ds \tag{1.18}$$

The difference Δ^{Iono} between measured (Eqn. 1.17) and geometric range (Eqn. 1.18) is called ionospheric refraction:

$$\Delta^{Iono} = \int (n-1) ds \tag{1.19}$$

which may be written for a phase refractive index n_{ph} from Eqn. 1.12 as

$$\Delta_{ph}^{Iono} = \int (n_{ph} - 1) ds = \int \frac{c_2}{f^2} ds \tag{1.20}$$

and for a group refractive index n_{gr} from Eqn. 1.15 as

$$\Delta_{gr}^{Iono} = \int (n_{gr} - 1) ds = - \int \frac{c_2}{f^2} ds \tag{1.21}$$

results, which can also be written as

$$\Delta_{ph}^{Iono} = - \frac{40.3}{f^2} \int n_e ds \tag{1.22}$$

$$\Delta_{gr}^{Iono} = \frac{40.3}{f^2} \int n_e ds \tag{1.23}$$

where Eqn. 1.16 has been substituted. Substituting Eqn. 1.8 into Eqn.s 1.22 and 1.23 yields

$$\Delta_{ph}^{Iono} = - \frac{40.3}{f^2} TEC_R^S = -I_R^S \tag{1.24}$$

$$\Delta_{gr}^{Iono} = \frac{40.3}{f^2} TEC_R^S = I_R^S \tag{1.25}$$

and substituting Eqn.s 1.22 and 1.23 into Eqn.s 1.9 and 1.10 we obtain:

$$P_{iR}^{S} = \rho_R^S + c(\delta t_R - \delta t^S) + T_R^S + I_{iR}^S \tag{1.26}$$

$$L_{iR}^{S} = \rho_R^S + \lambda_i N_{iR}^S + c(\delta t_R - \delta t^S) + T_R^S(t) - I_{iR}^S \tag{1.27}$$

For a numerical example, the delay $I_R^S = 0.18$ m is obtained if a frequency of say 1.5 GHz and one TECU is substituted.

Values of TEC vary between 10^{16} and 10^{19} electrons per m^2 along the radio wave path ([24]: p. 51). The electron density is highly variable and depends mainly on: geographic location, time of the day, season of the year and solar activity. Regions of highest TEC are located approximately ±15 to ±20 degrees each side of Earth's magnetic equator. The day to day variability has a standard deviation of ±20% to 25% of monthly average conditions (Klobuchar, 1996). Short term variations are *travelling ionospheric disturbances* (TID) with a period of minutes to about 1 hour, and *ionospheric scintillation* with a period of seconds.

A more complete version of Eqn.s 1.26 and 1.27 includes the sum of relativistic effects, phase center variations, and phase windup, which can all be grouped in the term ${p_R}^S$; and the multipath and noise terms, which can be written as ${m_R}^S$ and ${\varepsilon_R}^S$, respectively. Now we can rewrite Eqn. 1.27 as

$$\begin{aligned} L_{iR}^{S}(t) = \rho_R^S(t) + c(\delta t_R(t) - \delta t^S(t)) + T_R^S(t) - I_{iR}^{S}(t) \\ + \lambda_i N_{iR}^{S}(t) + {p_R}^S(t) + m_{iR}^{S}(t) + {\varepsilon_R}^S(t) \end{aligned} \tag{1.28}$$

1.5 LINEAR COMBINATIONS

Linear combinations of the original phase or code pseudorange observations are often used in order either to eliminate systematic biases (e.g. ionosphere-free combination) or to estimation atmospheric parameter (e.g. geometry free combination to estimate the ionospheric delays). The main drawback of the linear combinations is that the noise of the observable is higher than the original ones. The formulation of the generic linear combination reads as follows

$$L_{LC} = \alpha\, L_i + \beta\, Lj \tag{1.29}$$

where α and β are the real coefficients of the combination and L_i and L_j represent the original observations (either the code or phase pseudoranges) in length units and with frequencies i and j, respectively.

Starting from Eqn. 1.27 for phase pseudorange observations with the explicit notation of the dependency of the ionospheric delay on signal frequency (see Eqn.

1.25)

$$L_{iR}^{S} = \rho_{R}^{S} + \lambda_i N_{iR}^{S} + c(\delta t_R - \delta t^S) + T_R^S - \frac{A}{f_i^2} TEC_R^S \tag{1.30}$$

and grouping the terms that are not frequency dependent, equation 1.29 becomes

$$\begin{aligned} L_{LC} = (\alpha + \beta)\left[\rho_R^S + c(\delta t_R - \delta t^S) + T_R^S\right] + \Big[\alpha\, \lambda_i N_{iR}^S \\ + \beta\, \lambda_j N_{jR}^S\Big] - \left[\alpha\, \frac{A}{f_i^2} TEC_R^S + \beta\, \frac{A}{f_j^2} TEC_R^S\right] \end{aligned} \tag{1.31}$$

where $A = 40.3\ [m^3\, el^{-1}\, s^{-2}]$. Epoch tag, multipath and noise terms have been eliminated for the sake of simplicity.

The noise of the linear combination can be expressed as

$$\sigma_{LC} = \left(\sqrt{\alpha^2 + \beta^2}\right)\sigma_0 \tag{1.32}$$

with the assumption that both the original observations have the same level of noise σ_0.

For the interest of this work we focus on the ionosphere-free combination and the geometry-free combination, which are used by the VADASE algorithm (section 2) and the VARION algorithm (section 3), respectively.

1.5.1 IONOSPHERE-FREE COMBINATION

The ionosphere-free combination is the most efficient method to eliminate the ionospheric delay by using two signals with different frequencies. This method can be thought of as the main reason for the GNSS signals to be broadcast with (at least) two different frequencies. The ionosphere-free combination is formed from equation 1.31 using the following coefficients

$$\alpha = \frac{f_i^2}{f_i^2 - f_j^2} \qquad \beta = -\frac{f_j^2}{f_i^2 - f_j^2} \tag{1.33}$$

where $\alpha + \beta = 1$. Now, the ionosphere-free combination for two carrier phase observations with frequencies i and j is formed as follows

$$\begin{aligned} L_{IF} = {} & [\, \rho_R^S + c(\delta t_R - \delta t^S) + T_R^S \,] + (\, \alpha\, \lambda_i N_{iR}^S + \beta\, \lambda_j N_{jR}^S \,) \\ & - (\, \alpha\, \frac{A}{f_i^2} TEC_R^S + \beta\, \frac{A}{f_j^2} TEC_R^S \,) \end{aligned} \tag{1.34}$$

where the acronym *IF* stands for Ionosphere-Free. Tacking into account the last term of Eqn. 1.34 and substituting Eqn. 1.33 we obtain

$$\left[\frac{f_i^2}{f_i^2 - f_j^2} \right] \frac{A}{f_i^2} TEC_R^S - \left[\frac{f_j^2}{f_i^2 - f_j^2} \right] \frac{A}{f_j^2} TEC_R^S = 0 \tag{1.35}$$

As Eqn. 1.35 shows, the ionosphere-free combination cancels the ionospheric delay. It is worth to remember that we consider the first approximation of the ionosphere dependency upon the frequency, stopping at the first order term and neglecting higher terms from Eqn. 1.11. The major drawback of this combination is that the bias due to the ambiguity is no longer an integer value. We can define the ionosphere-free ambiguity N_{IF} as follows

$$N_{IF} = \frac{(f_i^2 \lambda_i N_{iR}^S + f_j^2 \lambda_j N_{jR}^S)}{f_i^2 - f_j^2} \tag{1.36}$$

and substituting the term N_{IF} into Eqn. 1.34 yields

$$L_{IF} = \rho_R^S + c(\delta t_R - \delta t^S) + T_R^S + N_{IF} \tag{1.37}$$

1.5.2 GEOMETRY-FREE COMBINATION

The geometry-free combination is used to remove terms that are non-dispersive with respect to the GNSS frequency, like the geometry, clocks and the tropospheric delay. For this reason this combination is insensitive to receiver motion. The geometry-free combination is formed from Eqn. 1.31 using the following coefficients

$$\alpha = 1 \qquad \beta = -1 \tag{1.38}$$

The geometry-free combination for two carrier phase observations with frequencies i and j is formed as follows

$$L_{GF} = (\ \lambda_i N_{iR}^{\ S} - \lambda_j N_{jR}^{\ S}\ ) - (\ \frac{A}{f_i^2} TEC_R^S - \frac{A}{f_j^2} TEC_R^S\ ) \tag{1.39}$$

where epoch tag, multipath and noise terms have been eliminated for the sake of simplicity.

1.6 SATELLITE ORBITS IN REAL-TIME

All satellite applications (from navigation to remote sensing) require satellite orbits to be known with a certain level of accuracy. For positioning purposes, in case a single receiver is used, any orbital error is highly correlated with the position error. On the contrary, for ionospheric remote sensing using GNSS observations, orbit errors do not affect the TEC estimation process [81].

Generally, the orbital motion of a satellite is the result of all forces acting on the satellite, the Earth's gravitational attraction being the most signicant one. From the mathematical point of view, the equations of motion for satellites are differential equations that are solved by numerical integration over time. For a complete dissertation on theory and practice of satellites orbits determination and prediction it is wise to refer to [60].

GNSS positions are available to the users in real-time as a specific part of the satellite message: the so called "broadcast ephemerides" are a set of parameters which allows the orbit computation with an accuracy ranging from one meter up to several meters, according to the considered constellation (i.e. GPS, GLONASS, Galileo). These parameters effectively describe satellite orbits for a short period of time; then, they rapidly become inaccurate.

For the scopes of this work it is sufficient to describe the algorithms used to compute GNSS orbits employing the broadcast ephemerides. The discussion is limited to satellite systems implemented and tested with the VADASE and VARION softwares at the moment of writing: GPS, GLONASS and Galileo.

1.6.1 Broadcast ephemerides

A master station on Earth compute the broadcast ephemerides based on observations acquired by other monitoring stations. These parameters are uploaded from the master station to all the satellites. Satellite broadcasts the ephemerides globally through the navigation signal. Generally, the broadcast ephemerides contain records with general information about the satellite, records with orbital information and records with information on the satellite clock.

1.6.1.1 GPS and Galileo

As regards GPS and Galileo constellations the orbit information contained in the broadcast ephemerides encompass the orbital Keplerian parameters and their temporal variation. At the same time, the information on the satellite clock is given in the terms of coefficients that can be used to model the clock offset with polynomials of second order.

Based on broadcast ephemerides, whose parameters are described in table 1.6.1, GPS and Galileo coordinates computation is performed using the algorithm described in table 1.6.2 [25, 40]; where t is the GPS/Galileo system time at epoch of transmission (i.e. GPS/Galileo time corrected for time of flight). t_k is the actual total time difference between the time t and the epoch time t_{oe} and must account for beginning or end of weeks crossovers.

Satellite clock error at observation epoch t can be computed applying the following second order polynomial

$$\delta t^s(t) = a_0 + a_1(t - t_{oe}) + a_2(t - t_{oe})^2 + \Delta t_r \tag{1.40}$$

Parameter	Explaination	Units
M_o	Mean (M.) Anomaly (Reference Time)	semi-circles (sc)
Δn	M. Motion Diff. From Computed Value	sc/sec
e	Eccentricity	dimensionless
$\sqrt{A}$	Square Root of the Semi-Major Axis	$\sqrt{\text{meters}}$
Ω_o	Longitude of Ascending Node (weekly)	sc
i_o	Inclination Angle at Reference Time	sc
ω	Argument of Perigee	sc
$\dot{\Omega}$	Rate of Right Ascension	sc/sec
$IDOT$	Rate of inclination angle	sc/sec
C_{rc}, C_{rs}	Corr. Terms (C.T.) – Orbit Radius	meters
C_{uc}, C_{us}	C.T. – Argument of Latitude	radians
C_{ic}, C_{is}	C.T. – Angle of Inclination	radians
t_{oe}	Reference Time for Ephemeris	seconds
$IODE$	Issue of Data (Ephemeris)	

Table 1.6.1: GPS and Galileo Keplerian parameters in broadcast orbits

where a_0 $[s]$ is the satellite clock bias, a_1 $[s/s]$ is the satellite clock drift, a_2 $[s/s^2]$ is the satellite frequency drift, t_{oe} $[s]$ is the clock data reference time, Δt_r $[s]$ is the correction due to relativity effects and t is the current time epoch.

Parameter	Description
Reference Ellipsoid	WGS84
Numerical Constants	
$\mu = 3.986005 \cdot 10^{14}\ [m^3 s^{-2}]$	Gravitational Constant
$\mathbf{\Omega_e} = 7.2921151467 \cdot 10^{-5}\ [rad\, s^{-1}]$	Earth Rotation Rate
$\pi = 3.1415926535898$	
Computation formulas	
$t_k = t - t_{oe}$	Time from Ephemeris Epoch
$A = (\sqrt{A})^2$	Semi-Major Axis
$n_0 = \sqrt{\mu / A^3}$	Computed Mean (M.) Motion
$n = n_0 + \Delta n$	Corrected (Corr.) M. Motion
$M_k = M_0 + n t_k$	M. Anomaly (An.)
$E_k = M_k + e sin\, E_k$	Eccentric An. (by iteration)
$v_k = tan^{-1} \frac{\sqrt{1-e^2} sin E_k}{cos E_k - e}$	True An.
$u_k = \omega_0 + v_k$	Argument of Latitude (Lat.)
$\delta u_k = C_{uc} cos\, 2u_k + C_{us} sin\, 2u_k$	Argument of Lat. Correction
$\delta r_k = C_{rc} cos\, 2u_k + C_{rs} sin\, 2u_k$	Radius Correction
$\delta i_k = C_{ic} cos\, 2u_k + C_{is} sin\, 2u_k$	Inclination Correction
$\omega_k = \omega_0 + \delta u_k$	Corr. Argument of Perigee
$r_k = A(1 - e cos\, E_k) + \delta r_k$	Corr. Radius
$i_k = i_0 + i t_k + \delta i_k$	Corr. Inclination
$x_k = r_k cos(\omega_k + v_k)$	x-coordinate – Orbital Plane
$y_k = r_k sin(\omega_k + v_k)$	y-coordinate – Orbital Plane
$\Omega_k = \Omega_0 + \dot{\Omega} t_k - \Omega_e (t - t_0)$	Corr. Ascending Node Long.
$X_k = x_k cos \Omega_k - y_k sin\, \Omega_k cos\, i_k$	ECEF Sat X Coordinate
$Y_k = x_k sin \Omega_k + y_k cos\, \Omega_k cos\, i_k$	ECEF Sat Y Coordinate
$Z_k = y_k sin\, i_k$	ECEF Sat Z Coordinate

Table 1.6.2: GPS and Galileo satellite coordinates computation

Error component	Mean square error	
	coordinates [m]	velocity [cm/s]
Along track	7.0	0.03
Cross track	7.0	0.03
Radial component	1.5	0.20

Table 1.6.3: Accuracy of transmitted coordinates and velocities of GLONASS-M satellites [28]

1.6.1.2 GLONASS

The GLONASS broadcast navigation message is generally transmitted as a half hourly satellite state vector, expressed in the PZ90 geocentric cartesian coordinate system [83]. Ephemeris parameters are periodically computed and uploaded to the satellites by the control segment. Mean square errors of transmitted coordinates and velocities of the satellites are given in table 1.6.3.

Given the state vector in the broadcast ephemeris at epoch t_b, satellite positions and velocities for the generic epoch t_0, with $|t_b - t_0| \leq 15$ min, can be computed by numerical integration of the differential equation of motion. Integration over short interval leads to the simplification of the force model by neglecting perturbing forces acting on the satellite but the lunar-solar effect which is assumed to be constant.

Without going through all the intermediate steps (which are duly reported in [28]), the final form of the satellite's equations of motion in the PZ90 system can be computed using the simplified algorithm [29]

$$\begin{aligned}
\dot{x} &= V_x \\
\dot{y} &= V_y \\
\dot{z} &= V_z \\
\ddot{x} &= \tfrac{\mu}{r^3}\,x - \tfrac{3}{2}\,J_2\tfrac{\mu a_e^2}{r^5}\,x\left(1 - \tfrac{5\,z^2}{r^2}\right) + \omega^2 x + 2\omega V_y + (\ddot{x})_{S+M} \\
\ddot{y} &= \tfrac{\mu}{r^3}\,y - \tfrac{3}{2}\,J_2\tfrac{\mu a_e^2}{r^5}\,y\left(1 - \tfrac{5\,z^2}{r^2}\right) + \omega^2 y - 2\omega V_x + (\ddot{y})_{S+M} \\
\ddot{z} &= \tfrac{\mu}{r^3}\,z - \tfrac{3}{2}\,J_2\tfrac{\mu a_e^2}{r^5}\,z\left(3 - \tfrac{5\,z^2}{r^2}\right) + (\ddot{z})_{S+M}
\end{aligned} \tag{1.41}$$

where $(\ddot{x}, \ddot{y}, \ddot{z})_{S+M}$ are the accelerations due to the lunar-solar gravitational perturbations and remain constant during the integration interval (15 min), $\mu = 3.98574405\,10^{14}$ $[m^3/s^2]$ is the Earth gravitational constant (mass of the Earth's atmosphere included), $a_e = 6378136$ $[m]$ is the semi-major (equatorial) axis of the PZ-90 Earth's ellipsoid, $J_2 = 1082625.7\,10^{-9}$ is the second zonal harmonic of the Earth's gravitational potential and $\omega = 7.292115\,10^{-5}$ $[rad/s]$ is the Earth rotation rate. The system can be written

$$\vec{\dot{Y}}(t) = F(t, \vec{Y}(t)) \tag{1.42}$$

where the initial condition for the equation 1.42 is the components of the satellite state vector $\vec{Y}(t_b)=\left[x(t_b), y(t_b), z(t_b), \dot{x}(t_b), \dot{y}(t_b), \dot{z}(t_b)\right]$ at epoch t_b. The numerical integration is performed using 4^{th} order Runge-Kutta technique ([70], pp. 710-715). The Runge-Kutta method is based in the following iterative algorithm:

$$\begin{aligned}
\vec{K}_1 &= F(t_n, \vec{Y}_n) \\
\vec{K}_2 &= F(t_n + h/2, \vec{Y}_n + \vec{K}_1 h/2) \\
\vec{K}_3 &= F(t_n + h/2, \vec{Y}_n + \vec{K}_2 h/2) \\
\vec{K}_4 &= F(t_n, \vec{Y}_n + \vec{K}_3 h)
\end{aligned} \tag{1.43}$$

where h is the integration step in seconds. The state vector computed at the generic epoch $n+1$ can be computed as follow

$$\vec{Y}_{n+1} = \vec{Y}_n + (\vec{K}_1 + 2\vec{K}_2 + 2\vec{K}_3 + \vec{K}_4)h/6\,. \tag{1.44}$$

Algorithm	Integration interval	
	5 [min]	15 [min]
Simplified	0.03 − 0.42	0.05 − 0.77

Table 1.6.4: Position prediction errors [m] at various intervals [min] [29]

Table 1.6.4 from [29] provides the SV's center of mass position prediction errors obtained through the numerical integration using the Runge-Kutta 4^{th} order method with a 1 minute increment for the identical initial data for the simplified algorithms after different integration intervals.

I learned very early the difference between knowing the name of something and knowing something.

Richard Feynman

2

VADASE Algorithm for Earth Science

In recent years, extensive work has been done to effectively exploit GNSS for estimating important earthquake parameters such as the seismic moment and magnitude (i.e. GNSS Seismology). The rapid and accurate assessment of these parameters is of crucial importance to achieve reliable tsunami generation scenarios and eventually dispatch an early warning. In this framework, Geodesy and Geomatics division (AGG) of University of Rome "La Sapienza" developed a new approach to obtain in real-time the 3D displacements of a single GNSS receiver. This solution, called VADASE (Variometric Approach for Displacement Analysis Standalone Engine), utilizes the broadcast orbits and the time differences of the high-rate (i.e. 1 Hz or more) carrier phases observations to ascertain the receiver movements over short intervals at a few centimeters accuracy level in real-time.

Next section 2.1 summarizes the state-of-art of VADASE. Section 2.2 illustrates the most recent developments of the algorithm, which include the leave-one-out and the augmented strategies. Section 2.3 shows the possible applications of the VADASE software in Earth science studies.

2.1 VADASE FUNDAMENTALS

VADASE is an algorithm able to estimate, on the basis of carrier phase observations and broadcast orbits, the velocity of a GNSS receiver between two observations epochs. The receiver displacements waveforms, for short intervals (few minutes), can be retrieved from the estimated velocities by simple integration. Here we recall the functional model of the least square estimation of the variometric approach in order to better assess the developments discussed in the next subsections. For a complete description of the VADASE estimation model, please refer to [9, 12, 18].

Starting from Eqn. 1.27, and being p_r^s the sum of the relativistic effects, phase center variations, and phase windup; and m_r^s and ε_r^s represent the multipath and the noise, respectively. Equation 1 is the difference in time (”Δ) between two consecutive epochs (t and $t+1$) of carrier phase observations in the ionospheric-free combination (α and β are the standard coefficients of L_{IF} combination, see Eqn. 1.33)

$$\begin{aligned}\alpha[\Delta L_{1r}^s] + \beta[\Delta L_{1r}^s] = {} & (\mathbf{e}_r^s \bullet \Delta\xi_r + c\Delta\delta t_r) + \\ & + ([\Delta\rho_r^s]_{OR} - c\Delta\delta t^s + \Delta T_r^s) + \\ & + ([\Delta\rho_r^s]_{EtOl} + \Delta p_r^s) + \Delta m_r^s + \Delta\varepsilon_r^s \end{aligned} \tag{2.1}$$

where where $\mathbf{e_r^s}$ is the unit vector from the satellite to the receiver, $\Delta\xi_r$ is the (mean) velocity of the receiver in the interval t and $t+1$, $[\Delta\rho_r^s]_{OR}$ is the change of the geometric range due to the satellite's orbital motion and the Earth's rotation, $[\Delta\rho_r^s]_{EtOl}$ is the change of the geometric range due to the variation of the solid Earth tide and ocean loading.

The term $(\mathbf{e_r^s} \bullet \Delta\xi_r + c\Delta\delta t_r)$ contains the four unknowns parameters (the 3D velocity $\Delta\xi_r$, and the receiver clock error variation $\Delta\delta t_r$); $([\Delta\rho_r^s]_{OR} - c\Delta\delta t^s + \Delta T_r^s)$ is the largest part of the known term that can be computed on the basis of known orbits and clocks and for the chosen tropospheric model; $([\Delta\rho_r^s]_{EtOl} + \Delta p_r^s)$ is an additional much smaller known term that can be computed with proper models for all of the considered effects; and Δm_r^s and $\Delta\varepsilon_r^s$ are the multipath and the noise term, as described previously.

The least squares estimation of the 3-D velocities is based upon the entire set of variometric equations 2.1, which can be written for two generic consecutive epochs (t and $t+1$). The number of variometric equations depends on the number of satellites common to the two epochs, and at least four satellites are necessary in order to estimate the four unknown parameters for each consecutive epoch couple.

2.2 ADVANCES

2.2.1 LEAVE-ONE-OUT CROSS VALIDATION

A strategy to detect outliers in the observations during the real-time estimation was defined on the basis of the Leave-One-Out Cross Validation (LOOCV) [13]. Standard techniques for outliers detection as the well known Baarda data snooping, do not generally supply statistical tests of proper power, due to the low redundancy of the epoch by epoch solution; on the contrary, LOOCV is more powerful, at the cost of n-repeated least squares epoch by epoch solutions (being n the number of satellite common in view in two consecutive epochs), which are however still feasible from the computational point of view (VADASE-LOO). Therefore if n is the number of variometric equations, where the number of the set of equations depends on the number of satellites common to the two epochs, the Leave- one-out-LOO method applied to VADASE algorithm involves the iterative application of the algorithm using all the satellites except one, different in each iteration. The satellite left out is considered outlier on the basis of statistical test.

2.2.2 AUGMENTED VADASE

Discrete integration of 3D estimated velocities obtained of VADASE-LOO was often impacted by trends. It was clearly identified a strong spatial correlation of these trends among close GNSS stations (within 100 km) due to the common errors in the satellite broadcast orbits and clocks. For this reason it was introduced a new strategy, called augmented strategy (A-VADASE) in order to filter out these trends. The approach used to filter the trend is based on the computation of the statistical index of the spatial median of the displacements epoch by epoch considering all station involved in the phenomena.

2.3 2016 MEINONG EARTHQUAKE, TAIWAN

On February 5, 2016 at 19:57:27 UTC, a M 6.4 earthquake occurred east of Tainan in southern Taiwan as the result of oblique thrust faulting at shallow-mid crustal depths (around 20 km) (USGS summary). Focal mechanisms indicate rupture occurred on a fault oriented either northwest-southeast, and dipping shallowly to the northeast, or on a north-south striking structure dipping steeply to the west. Taiwan lies in a region of complex tectonics, at the boundary between the Philippine Sea and Eurasia plates. To the north and east, the Philippine Sea plate subducts beneath Eurasia towards the north-northwest, along the Ryukyu Trench. South of the island, the South China Sea (on the the Eurasia plate) subducts to the east beneath the Philippine Sea plate at the Manila Trench. Moving north, subduction tectonics transition to arc-continent collision along the western side of Taiwan. At the location of the earthquake, the two plates converge in a northwest-southeast direction at a velocity of about 80 mm/yr.

Taiwan is the location of frequent seismicity, and 90 M 6.4+ events have occurred within 250 km of the February 5, 2016 event over the preceding century. Several of these earthquakes occurring beneath Taiwan (rather than in the subduction zone northeast of the island) have been destructive.

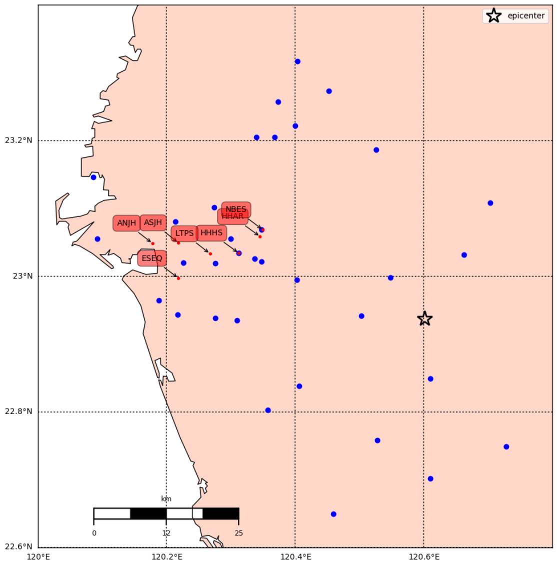

Figure 2.3.1: 34 dual frequency GNSS receivers (blue) and 7 single frequency (red) receivers alongside the Hsinhua fault.

2.3.1 DATASET

Taiwan has a very dense network of GNSS dual frequency receivers. A project from the Department of Earth Science in National Cheng-Kung University (NCKU), Tainan, aims to densify the existing network of GNSS receivers along the Hsinhua fault using single frequency low-coast receivers. Fig. 2.3.1 shows the dual frequency network (blue) and the installed single frequency receivers (red) near the epicenter location. In this study we used GNSS data with 1 Hz observation rate for a time interval of 300 seconds. In order to compare the solutions coming from single and dual frequency receivers, we processed all the data using only L1 observations only and broadcast orbits and clocks.

2.3.2 COMMON TRENDS REMOVAL

Fig. 2.3.2 shows the VADASE displacements solutions (East, North, Up components) before and after removing the trends. We computed the median over 30

GNSS receivers (blue curve) in order to fit common trends (upper three plots). These trends were then removed from 5 single frequency receivers (lower three plots).

2.3.3 REAL-TIME COSEISMIC DISPLACEMENTS ESTIMATION

This sections describes a prototypal real-time statistical testing procedure to estimate coseismic displacement. The main statistical hypothesis is that the standard deviation of the solutions is equal before and after the earthquake. In this way we can compute the earthquake's duration by applying the F-test of equality of variances [52].

Figure 2.3.3 shows the estimated coseismic displacement computed from the low-coast receiver HHHS. The blue curve represents the original solutions, the black one the median computed over 30 GNSS station, and the red curve is the de-trended solution. The coseismic displacement computed using the de-trended solution was +4.9 cm and -1.8 cm in the East and North components, respectivelly.

Figure 2.3.4 shows the estimated coseismic displacement computed from the low-coast receiver NBES. The blue curve represents the original solutions, the black one the median computed over 30 GNSS station, and the red curve is the de-trended solution. The coseismic displacement computed using the de-trended solution was -4.9 cm and -6.1 cm in the East and North components, respectivelly.

2.3.4 S WAVES VELOCITY ESTIMATION

Fig. 2.3.5 shows how it is possible to combine together the real-time solutions coming from single (light blue) and dual (red) frequency GNSS receivers in order to estimate the propagation speed of the surface waves (dark blued line). The high-rate GNSS velocity were organized with increasing epicentral distances for the East-West and North-South components. We fitted the arrival times of the wave at different location using a least-square regression line. The slope of this

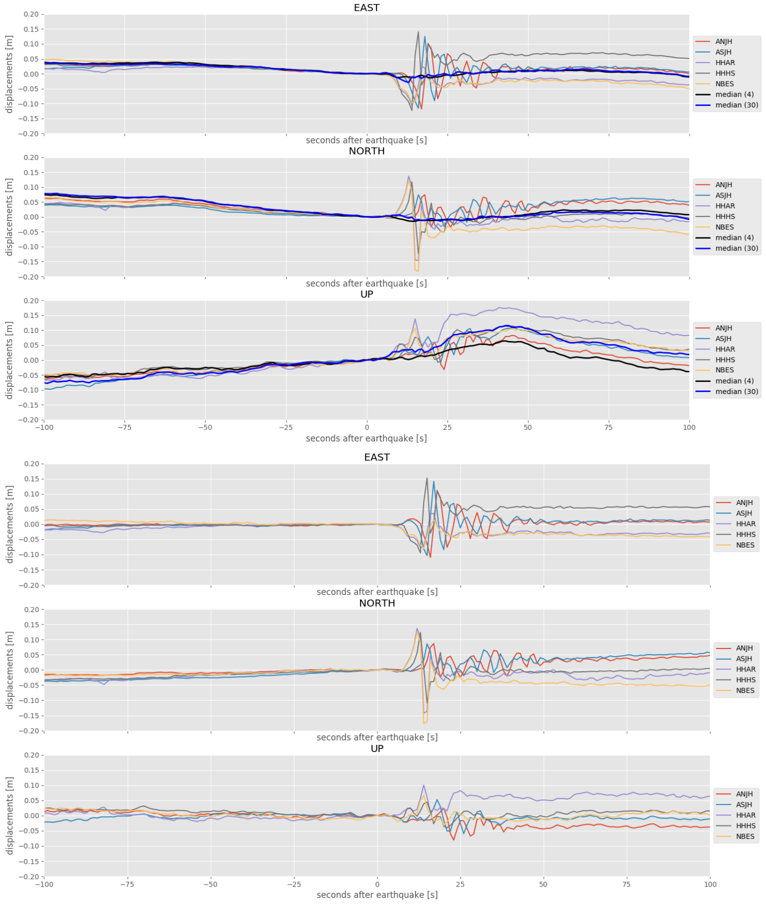

Figure 2.3.2: VADASE displacements solutions (East, North, Up components) before and after removing the trends. The upper three plots show the median computed over 30 GNSS receivers (blue curve). Lower three plots show the de-trended displacements for 5 single frequency receivers.

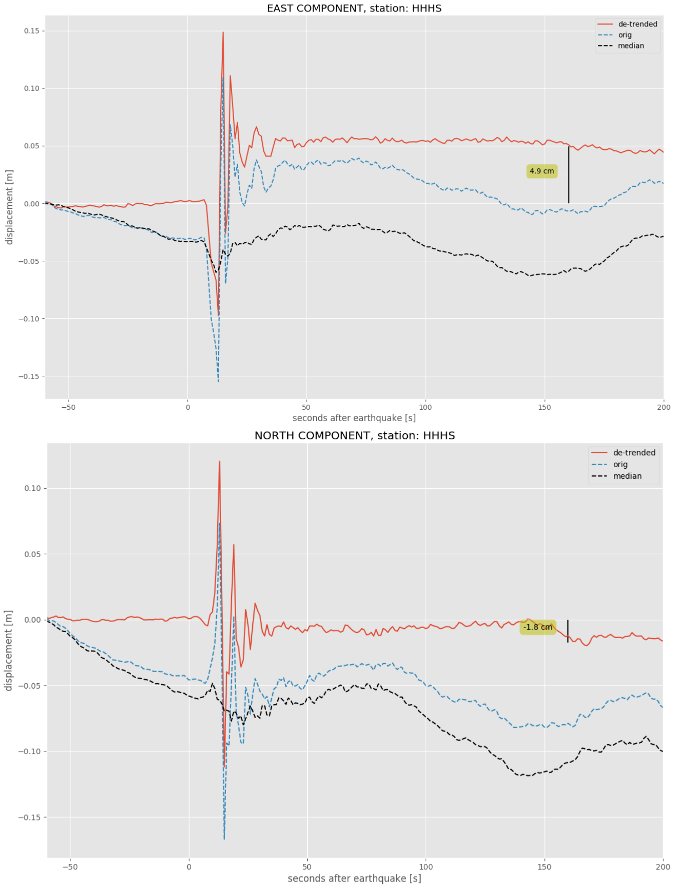

Figure 2.3.3: Coseismic displacement at the low-coast receiver HHHS. The blue curve represents the original solutions, the black one the median computed over 30 GNSS station, and the red curve is the de-trended solution

Figure 2.3.4: Coseismic displacement at the low-coast receiver NBES. The blue curve represents the original solutions, the black one the median computed over 30 GNSS station, and the red curve is the de-trended solution.

line represents the velocity of the S waves. We found that the S waves moved away from the epicenter with an estimated velocity around 3.22-3.89 km/s.

2.3.5 Conclusions

The knowledge of coseismic deformations due to earthquakes represents the fundamentals on which studies on seismic cycle and fault source mechanism are based on. A–VADASE–LOO strategy can be considered as a new approaches, based on the GNSS monitoring, to compute the coseismic displacements in real time. This approach is based on the analysis of 1 Hz GPS data as differences of average between two moving windows of 30x30 size immediately before and immediately after the earthquake mainshock applying at the two windows a statistical test, based on the hypothesis of a constant mean level noise of the VADASE velocity estimates over few minutes.

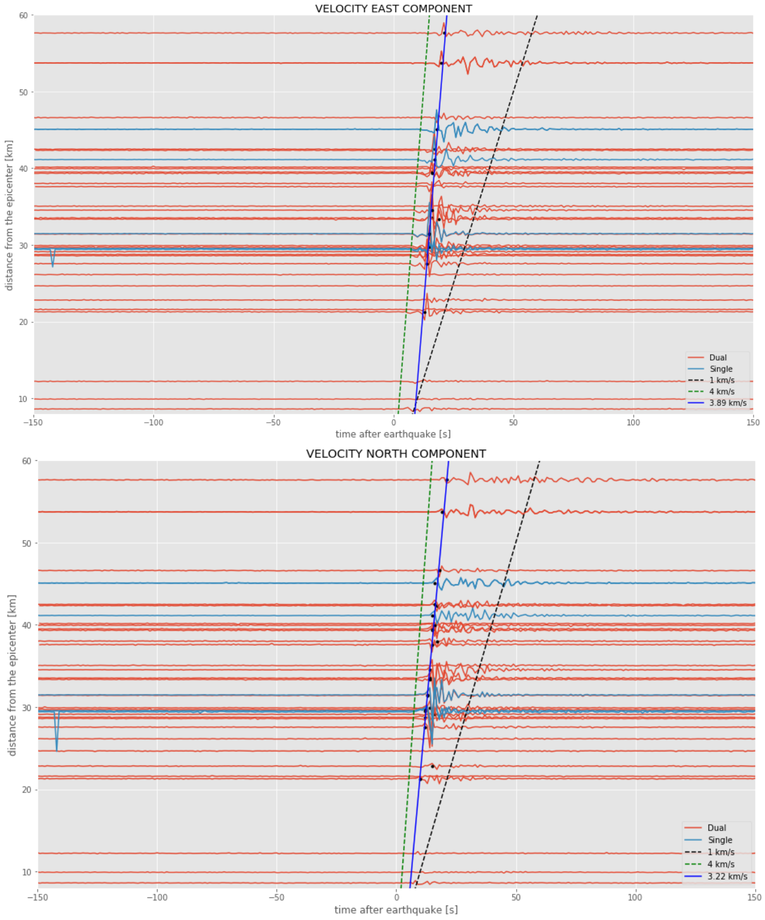

Figure 2.3.5: Estimation of the S waves propagation velocity from single (light blue) and dual (red) GNSS receivers. High-rate GNSS velocity were organized with increasing epicentral distances for the East-West and North-South components.. The arrival times of the wave at different locations were fitted using a leas-square regression line. The slope of this line represents the velocity of the wave.

All right, but apart from the sanitation, the medicine, education, wine, public order, irrigation, roads, the fresh-water system, and public health, what have the Romans ever done for us?

Monty Python's Life of Brian

3

VARION Algorithm for Natural Hazards

Section 3.1 gives a description of the physical mechanisms behind the perturbations in the Earth's ionosphere caused by different natural hazards. Section 3.2 provides a description of the main characteristics of two of the main natural hazards studied in this work: tsunami and meteotsunami. Section 3.3 is devoted to our new GNSS processing algorithm, named VARION (Variometric Approach for Real-Time Ionosphere Observation) with a focus on the real-time detection of TIDs caused by tsunami atmospheric gravity waves. Section 3.4 describes the effects of the observations geometry on the sTEC estimations.

3.1 Natural Hazards from the Ionosphere

TEC variations in GNSS signals can be exploited to detect perturbations in the ionosphere caused by a wide variety of sources. Natural hazards such as earthquakes, tsunamis, volcanic eruptions, or deep convective events (large hurricanes or tornadoes), generate atmospheric perturbations. Man-made sources such as explosions and rocket ascents are also detectable. External sources as such geomagnetic storms, aurora, and plasma instabilities, are also observable. This analysis can be performed at ground-based GNSS receivers by estimating the relative change of the ionospheric TEC over time directly from the GNSS phase observations. The GPS approach was first used to detect small electron density and TEC variations generated by surface displacements resulting from the 1994 M6.7 Northridge, California earthquake [23],[15]. These TEC anomalies occur following the deformation of the solid Earth indicates that there exists a coupling between the Earth's surface and the atmosphere. Two of the main mechanisms by which motions of the Earth's surface induce variations in electron density in the ionosphere are acoustic waves and gravity waves. Large-scale vertical motions of the Earth's surface may also generate gravity waves from the buoyancy forces on the vertically displaced air. If these waves have a frequency smaller than the Brunt-Vaisala frequency they will propagate upwards from the source and reach the ionospheric layers. Over some periods these acoustic and gravity wave modes are coupled and both may need to be considered [78], [2]. The compressions and rarefactions of the ionospheric electron density produce deviations in TEC from the dominant diurnal variation. For many applications, such as TID detection, is the deviations (also known as fluctuations or perturbations) from the background level that are of interest. The precision of the measurements of deviations from the background is around 0.01 to 0.1 TECU [26].

3.1.1 Acoustic waves

Pressure-induced TEC anomalies from earthquakes have been widely observed in the last decade, for example, coseismic traveling ionospheric disturbances (CIDs) were documented with the 2003 M_W 8.3 Tokachi-oki, Japan and the 2008 M_W 8.1 Wenchuan, China earthquakes [76] observed at Japanese GEONET sites (Sagiya et al 2000). CIDs produced by the 2011 M_W 9.0 Tohoku-oki, Japan earthquake were widely reported by several independent research groups (e.g. [27],[45], [75]. Volcanic eruptions can also excite acoustic waves and induce anomalies in the TEC measurements [20], [82]. When an earthquake occur, direct (or shock) acoustic waves (SAWs) are produced in the proximity of the epicenter (within 500 km), and secondary acoustic waves caused by surface Rayleigh waves propagating far from the epicenter. These pressure waves, upon reaching the ionosphere, will locally affect electron density through particle collisions between the neutral atmosphere and the electron plasma [43]. Motions of the Earth's surface produce SAWs, which are pressure waves that propagate upwards through the atmosphere at the local speed of sound. The onset of the anomalies following the geophysical event is typically about 10min [20], [26] and reflects the time needed for the first acoustic waves to propagate at the speed of sound to the F layer density peak. Many studies have found the horizontal propagation speed of the anomaly to be around 600-1000 m/s, in agreement with the speed of sound at typical F layer heights [6], [27], [49]. High amplitude surface waves, particularly Rayleigh waves, are also capable of generating acoustic waves [5]. As the surface wave travels away from the epicenter, they becomes a moving source of coupled atmospheric acoustic and gravity waves, which propagate upwards to the ionosphere. It is important to highlight that only acoustic waves which have a frequency greater than the cut-off frequency can propagate up to the ionosphere [22]. Such frequency is defined as $\omega_a = \frac{\gamma g}{2c_S}$ where c_S is the speed of sound, γ and g are respectively the ratio of specific heats and gravitational acceleration [3], [84]. Thus, the waves with a frequency greater than the cut-off one reach the ionosphere and their amplitude grows of a factor 10^4-10^5 as the atmosphere density decreases with altitude; such amplification is due to the conservation of kinetic energy. Otherwise amplitude decreases exponentially with altitude [3] and in this case, the waves are named evanescent. The typical values of cut-off frequency fall within the range 2.1-3.3 mHz [3], [20].

3.1.2 GRAVITY WAVES

Gravity waves form when air parcels are lifted due to particular fluid dynamic and then pulled down by buoyancy in an oscillating manner. This can occur when air passes over mountain chains [67] or when a "mountain", which is read as tsunamis wave, is moving with a certain velocity. Let us imagine the displacement of a volume of atmospheric air from its equilibrium position, it will then find itself surrounded by air with different density. Buoyant forces will try to bring the volume of air back to the undisturbed position but these restoring forces will overshoot the target and lead it to oscillate about its neutral buoyancy altitude. It will continue this oscillation about an equilibrium point, generating a gravity wave that can propagate up through the ionosphere.

Perturbations at the surface that have periods longer than the time needed for the atmosphere to respond under the restoring force of buoyancy will successfully propagate upwards. This is known as the Brunt-Vaisala frequency N and represents the maximum frequency for vertically propagating gravity waves. In an isothermal atmosphere where $\partial T/\partial z = 0$, $N \approx 0.02\ s^{-1}$ and the buoyancy period is about 5 min. Holton [72] gives $N \approx 0.012\ s^{-1}$ for average tropospheric conditions, so that the buoyancy period is about 8 min. The buoyancy period is about 5 min at the Earth's surface [26]. Tsunamis have periods longer than this frequency and thus excite gravity waves in the atmosphere. The notion that gravity waves generated by tsunami waves (even with wave heights of few centimeters in deep ocean) can propagate upward in the atmosphere and ultimately cause perturbations in the total electron content (TEC) of the ionosphere was first established by Daniels [19], and was theoretically further developed by Hines [34],[35]. Peltier and Hines [68] subsequently showed that these TEC variations can be detected through ionosonde measurements. The vertical propagation speed of an atmospheric gravity wave at these periods is 40-50 m/s [4], so these perturbations should first be observed about 2 h after the onset of the tsunami. The TEC anomalies can be identified by their horizontal propagation speed, which is much slower (200-300 m/s) than that of the acoustic TID or Rayleigh-wave-induced anomalies and follows the propagation speed of the tsunami itself, which is, much like the Rayleigh waves in the acoustic case, a moving source of gravity waves. However, following the 2011 M_W 9.0 Tohoku-oki, Japan event, which provided dense near-field TEC observations, it was noted that the onset of the gravity-wave-induced TEC anomalies was shorter, at about 30 *min* after the start of the earthquake, and not the 1.5-2 *h* predicted by previous theoretical computations [27]. This is explained as evidence that it might not be necessary for the gravity wave to reach the F layer peak (around 300 km altitude) for the TEC disturbance to be measurable. Rather, disturbances at lower altitudes within the E layer and the lower portion of the F layer might be substantial enough to be seen in the TEC observations. This is supported by previous modeling results that showed significant TEC perturbations over a broad area around the F layer peak [75]. Through comparisons with tsunami simulations of the event it was convincingly demonstrated that the tsunami itself must be the source of the observed gravity waves [27]. In light of these observations, ionospheric soundings may be used to monitor tsunamis and issue warnings in advance of their arrival at the coast [45], [62], [81].

3.2 TSUNAMI AND METEOTSUNAMI CHARACTERISTICS

As illustrated in section 3.1.2, tsunamis excite gravity waves in the atmosphere that can propagate upward and induce perturbations in the ionosphere. This section describes the main physics characteristics of tsunami and meteotsunami.

3.2.1 TSUNAMI

A tsunami is a series of ocean waves that are typically generated by an underwater geological event such as an earthquake, volcanic eruption, or a submarine landslide. The resulting abrupt change in sea-surface height sends a set of long waves propagating outward from the point of origin. As the waves approach the coastline and the water shoals, they are amplified and can be extremely destructive, depending on the shape of the coastline and the bathymetry.

Earthquakes are the most common source of tsunamis. The types of earthquakes that generate tsunamis are typically dip-slip events of magnitude (M) 6.5 or greater. Because earthquakes generate tsunamis primarily through vertical coseismic displacement of the seafloor and overlying water column, dip-slip earthquakes are more efficient at generating tsunamis than strike-slip earthquakes (e.g., [90], [66]). They frequently occur in the Pacific, where dense oceanic plates slide under the lighter continental plates. When these plates fracture they provide a vertical movement of the seafloor that allows a quick and efficient transfer of energy from the solid earth to the ocean. Because earth movements associated with large earthquakes are thousand of square kilometers in area, any vertical movement of the seafloor immediately changes the sea-surface. The resulting tsunami propagates as a set of waves whose energy is concentrated at wavelengths corresponding to the earth movements ($\sim$ 100 km), at wave heights determined by vertical displacement ($\sim$ 1 m), and at wave directions determined by the adjacent coastline geometry. Because each earthquake is unique, every tsunami has unique wavelengths, wave heights, and directionality. From a tsunami warning perspective, this makes the problem of forecasting tsunamis in real time daunting

3.2.2 Meteotsunami

A meteotsunami is very similar to a tsunami in that they are shallow-water gravity waves that are affected by ocean depth, and propagate and evolve in the same manner; however, the origin of these waves differs. Meteotsunamis are generated by traveling atmospheric disturbances, such as frontal passages, gravity waves, squall lines, and significant pressure jumps. The pressure perturbations associated with these disturbances have been identified as sources of atmospheric forcing that translate energy to the ocean surface [32], [58], [57]. A pressure change causes a minor change in sea level due to the inverted barometer effect. For example, a pressure jump of 3 mb causes the sea level to drop by about 3 cm. It is important to note that a passing disturbance will not necessarily trigger a meteotsunami unless resonance occurs.

3.2.2.1 External Resonance

Resonance occurs when the speed of the pressure perturbation matches the speed of the ocean wave. At this point, the atmospherically-forced energy transfer can generate and energize long ocean surface waves, inducing a significant sea level response [73], [89], [59]. Proudman resonance [71], is the most important type for meteotsunami generation (e.g. on the U.S. East Coast) and is produced when the speed of the atmospheric disturbance, U, matches the phase speed of the ocean wave, c:

$$U = c = \sqrt{gH} \tag{3.1}$$

where g is gravity and H is the depth of the water column beneath the traveling pressure perturbation. This external resonance alone will not necessarily result in a destructive meteotsunami. As the waves propagate towards shore, the potential for coastal inundation will be maximized when internal resonance occurs.

3.2.2.2 Internal Resonance

A semi-enclosed water body has a natural resonance, and if the resonance frequency matches that of the incoming ocean wave then strong amplification can occur. The strength of the amplified wave is dependent on the size, shape, and depth of the water body. Stronger oscillations occur in long, narrow inlets, as these tend to be systems with a low rate of energy dissipation. Inlets that rapidly shoal are also susceptible, as the wave is forced to slow down with the decrease in water column depth, and its height grows. The potential for a strong meteotsunami is also maximized if the water body is oriented towards the oncoming wave [59].

3.3 VARION Methodology

VARION is an open source, entirely Python-based software (`https://github.com/giorgiosavastano/VARION`). It was derived from the VADASE (Variometric Approach for Displacements Analysis Standalone Engine) algorithm that was successfully applied to estimate in a real-time scenario the ground velocities and displacements induced by several earthquakes (e.g. the Tohoku-Oki earthquake, USGS Mw 9.0, 11 March 2011, 05:46:24 UTC; the Emilia earthquake, USGS Mw 6.0, 20 May 2012, 02:03:52), using a stand-alone GNSS receiver [9, 12, 18]. The VADASE algorithm was later modified and applied to geometry-free combinations of GNSS carrier-phase measurements for estimating TEC variations. Using the VARION algorithm each dual-frequency GNSS receiver is expected to provide time series of real-time TEC variations in a stand-alone operational mode.

The VARION approach is based on single time differences of geometry-free combinations of GNSS carrier-phase measurements, using a standalone GNSS receiver and standard GNSS broadcast products (orbits and clocks corrections) that are available in real-time. We start from the carrier-phase observation 1.28, which in length units is

$$\begin{aligned} L_{iR}^{S}(t) = \rho_{R}^{S}(t) + c(\delta t_R(t) - \delta t^S(t)) + T_{R}^{S}(t) - I_{iR}^{S}(t) \\ + \lambda_i N_{iR}^{S}(t) + p_{R}^{S}(t) + m_{iR}^{S}(t) + \varepsilon_{R}^{S}(t) \end{aligned} \tag{3.2}$$

where i is the index of the signal frequency, subscript R refers to a particular receiver and superscript S refers to a satellite. λ is the carrier phase wavelength; ρ_R^S is the geometric range; c is the speed of light; δt_R and δt^S are the receiver and the satellite clock errors, respectively; T_R^S and I_R^S are the tropospheric and the ionospheric delays along the path from the satellite to the receiver, respectively; N_{iR}^S is the phase ambiguity; p_R^S is the sum of the other effects (relativistic effects, phase center variations, and phase windup); and m_R^S and ε_R^S represent the multipath and the noise, respectively.

If no cycle slips occurred, the unknown carrier phase ambiguity can be considered constant between two consecutive epochs. The receiver and the satellite Inter-Frequency Biases (IFB) in the carrier-phase ionospheric observable are also assumed as constant for a given period [Bishop, G. et al., 1994 [10], Sardon and Zarraoa 1997 [79], Brunini, C. et al. 2005 [14], Ciraolo, L. et al. 2007 [16]]. For these reasons, differentiating (Eqn. 3.2) in time between two consecutive epochs (t and t+1), and applying the geometry-free combination (Eqn. 1.39), we obtain the geometry-free time single-difference observation equation (Eqn. 3.3), with no need of estimate in real-time the phase ambiguity and the IFB

$$L_{GF}(t+1) - L_{GF}(t) = \frac{f_1^2 - f_2^2}{f_2^2}\left[I_{1R}^{S}(t+1) - I_{1R}^{S}(t)\right] \tag{3.3}$$

where the subscript L_{GF} refers to the geometry-free combination and f_1 and f_2 are the two GNSS frequencies, which for GPS are 1575.42 MHz and 1227.60 MHz respectively.

Taking into account the ionospheric refraction along the geometric range, we compute the sTEC variations between two consecutive epochs (Eqn. 3.4)

$$\delta\, sTEC(t+1,t) = \frac{f_1{}^2 f_2{}^2}{A(f_1{}^2 - f_2{}^2)}\left[L_{4R}^{S}(t+1) - L_{4R}^{S}(t)\right] \tag{3.4}$$

where $A = 40.3\ [Hz^2][m^3]/[n.\ of\ electrons]$ comes from the coefficient of the first order term of the dispersion formula (an explicit derivation can be found in [30]) and f is the carrier frequency of the GNSS signal; the discrete derivative of $sTEC$ over time can be simply computed dividing $\delta sTEC$ by the interval between epochs t and (t+1). A complete description of VARION algorithm is provided in [81].

It is important to remember that $sTEC$ is an integrated quantity representing the total number of electrons included in a column with a cross-sectional area of 1 m^2, counted along the signal path s between the satellite S and the receiver R; the unit of measurement of $sTEC$ is the $TECU$ (see section 1.3.2.4). Anyway, looking at the distribution of the electron content with the height, we know that the largest ionospheric delay's contribution comes from the F2 region. For this reason, the $sTEC$ observations are modeled by collapsing them to the point of intersection between the satellite-receiver line-of-sight and a surface located at the height of F2 peak (approximately 300-350 kms), where the electron density is approximated to be maximum (section 1.3.2.4). The intersection point is also known as ionospheric pierce point (IPP) and its position can be computed in real time using standard GNSS broadcast orbits. Therefore, the total electron content variations $\delta sTEC$ (and its discrete derivative) provided by VARION are also referred to the

IPP.

It is also important to emphasize that, since we are using the geometry-free combination [7], the receiver motion does not affect the *sTEC* estimation process. For this reason, ship-based GNSS receivers could also be used to increase the ionosphere monitoring coverage over the oceans.

In order to understand how the detection of the tsunamis (or other natural hazard) works in practice using the $\delta sTEC$ discrete derivative provided by VARION, we need to elaborate more on the physical meaning of this quantity. This quantity is a total derivative over time, therefore encompassing both the partial time derivative and the variation over time due to the IPP displacements as well as the *sTEC* space wise variation, as standard in analytical mechanics:

$$\frac{d\, sTEC(t,s)}{dt} = \frac{\partial sTEC(t,s)}{\partial t} + \vec{V}_{ipp} \cdot \nabla sTEC(t,s) \tag{3.5}$$

where $\vec{V}_{ipp}$ is the IPP's vector velocity field and $\nabla sTEC(t,s)$ is the spatial gradient of sTEC. Note that the IPP does not follow the ions velocity field, since the IPP velocity vector is driven by the satellite orbit and the receiver location/motion on the ground. It is clear that the ionospheric remote sensing based on GNSS ground-based observations depends on the time-dependent position of the IPPs. To get the total $\Delta sTEC$ variation over a certain interval while the IPP is moving along its path, Eqn. 3.5 is integrated over time (from t_0 to t_f):

$$\Delta sTEC(t_f, t_0) = \int_{sTEC_0}^{sTEC_f} d\, sTEC(t,s) \tag{3.6}$$

Eqn. 3.6 is used to detect tsunami-TIDs in real-time. The results are filtered using a finite duration impulse response (FIR) high-pass filter (see section 5.1).

It is worth to underline the main difference between VADASE and VARION algorithm. In fact, the VADASE algorithm uses all the variometric observation equations 2.1 in order to estimate the 4 unknowns parameters (the 3D velocity, and the receiver clock error variation). If we assume that n satellites are viewed by the receiver both at epochs t and $t+1$, the problem is overdetermined and $n-4$

is referred to as the redundancy of the system.

The VARION algorithm uses a different approach in order to estimate the unknown parameters $\delta sTEC$. Each VARION equation 3.4 can be written for a specific satellite-receiver link, for two generic consecutive epochs (t and $t+1$). The only unknown parameter ($\delta sTEC$) is different for each satellite-receiver link. This means that if we assume that n satellites are viewed by the receiver both at epochs t and $t+1$, the system has n equations and n unknown parameters and the redundancy of the system is zero. For this reason, each satellite-receiver link is processed as an independent thread.

3.4 HOW GEOMETRY AFFECTS OBSERVATIONS

This section describes the GNSS ionospheric remote sensing geometry. Physical explanations of the impacts of the observation geometry on the sTEC observations are provided in this section.

3.4.1 IONOSPHERE SINGLE LAYER MODEL

A frequently used model for sTEC data geolocation in satellite geodesy is the single layer ionospheric model. In our model, this layer is represented by a surface having a constant ellipsoid height h_I above the reference ellipsoid that approximates the earth's surface. We assume that the highest ionospheric delay's contribution comes from the F_2 region of the ionosphere ($h_I = 350\ km$), where the electron density is maximum. For this reason, the sTEC observation is defined by the intersection between the satellite-receiver line-of-site and the layer located at the height of F_2 peak. This point is called ionospheric pierce point (IPP). In other words the sTEC value, which is an integrated quantity, is collapsed into one point. Ionospheric remote sensing using GNSS observations depends on the time and space evolution of the IPP.

In order to understand the effect of the IPP motion on the sTEC observations, we need to know the time evolution of the IPP velocity (see Eqn. 3.5).

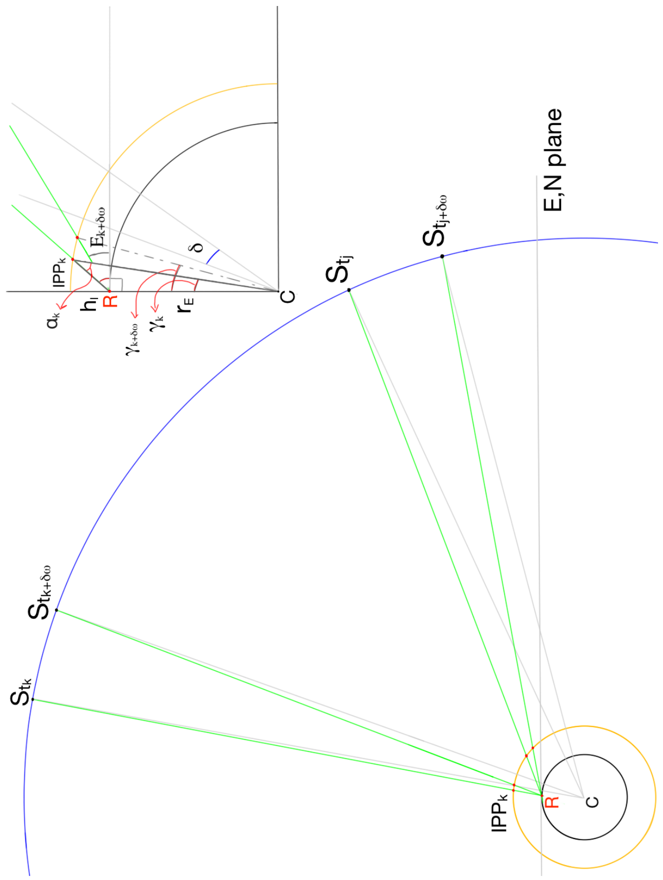

Figure 3.4.1: Spherical representation of the ionosphere single layer model, where r_E is the Earth's radius, C is the Earth's center of gravity, and E is the elevation angle of satellite S from an observer R. Here we considered R to lie in the S-C plane.

3.4.1.1 IPP POSITION FROM OBSERVATIONS

This section explains the numerical method implemented in VARION in order to compute in real time the IPP coordinates (and then SIP).

Starting from the ECEF (earth-centered, earth-fixed) coordinates of the GNSS receiver (X_R, Y_R, Z_R) and the satellite (X^S, Y^S, Z^S) at a certain epoch t, we can compute the midpoint M_i between the receiver and the satellite (X_M, Y_M, Z_M). Subsequently, we convert this point into geographical coordinates $(\varphi_M, \lambda_M, h_M)$, and for each iteration, the h_M value is checked against the height of ionospheric layer h_I (e.g. 350 km):

1. if $h_M > h_I$ (condition always true at the first iteration), then a new midpoint M_{i+1} between the receiver and the previous midpoint M_i is computed
2. when $h_M < h_I$, then the midpoint M_k is computed between the two previous midpoints M_{k-1}, M_{k-2}

This algorithm stops when the condition $h_M - h_I < \varepsilon$ is met, where ε was set to 10 km. This new algorithm, compare with e.g. Klobuchar algorithm [44], has the advantage that the IPP is surely located on the line of sight satellite-receiver.

3.4.1.2 IPP MOTION FROM MODEL

Under the spherical Earth approximation, the satellite is moving with a constant angular velocity ω describing a circular orbit around the Earth. Fig. 5.3.1 shows a schematic representation of the spherical ionospheric single layer model used here to compute the IPP velocity knowing the satellite elevation angle E. Here we considered the Receiver R to lie in the plane defined by the Satellite S (and so of the IPP) and the Earth's center of gravity C. In this way we can make the problem two-dimensional in a plane perpendicular to the horizontal plane (E-N plane) defined at the Receiver (see Fig. 5.3.1). An extension of this algorithm for a receiver lying on different planes will be investigated in the future.

First we compute the IPP Earth angle at epoch t_k using the equation:

$$\gamma_k = 90 - E_k - a_k \tag{3.7}$$

where E_k is the elevation angle and a_k can be computed as:

$$a_k = arcsen\left(\frac{r_E}{r_E + h_I} cosE_k\right) \tag{3.8}$$

where r_E is the mean Earth's radius. Subsequently we can compute the distance c of the IPP from the receiver

$$c_k = -R\, sin(E_k) + (R + h) cos(a_k) \tag{3.9}$$

After a time interval Δt (e.g. 30 s) the satellite sweeps out an angle $\delta = \omega \Delta t$ with respect to the center of the Earth. The IPP Earth angle at epoch $t_k + \Delta t$ is given by:

$$\gamma_{k+\Delta} = \gamma_k + \delta \tag{3.10}$$

Now, we can compute the elevation angle $E_{k+\Delta}$ at the new epoch using the equation:

$$E_{k+\Delta} = arctan\left(cos(\gamma_{k+\Delta}) - \frac{r_E}{r_E + h_I}\right) / sen(\gamma_{k+\Delta}) \tag{3.11}$$

Using Eqn 3.8 and Eqn 3.9 we can compute the angle $a_{k+\Delta}$ and the distance $c_{k+\Delta}$, respectively.

Using a linear approximation for short time intervals Δt, we are able to compute the 2D distance (assuming that the trajectory is all include into a plane) traveled by the IPP between the two epochs

$$d_{k,k+\Delta} = \sqrt{(c_k cosE_k - c_{k+\Delta} cosE_{k+\Delta})^2 + (c_k sinE_k - c_{k+\Delta} sinE_{k+\Delta})^2} \tag{3.12}$$

Figure 3.4.2 shows IPP velocity vs satellite elevations angle. The colored dots represent the IPP velocity values computed from the observations with the algorithm described in 3.4.1.1. The black curve represents the modeled IPP velocity

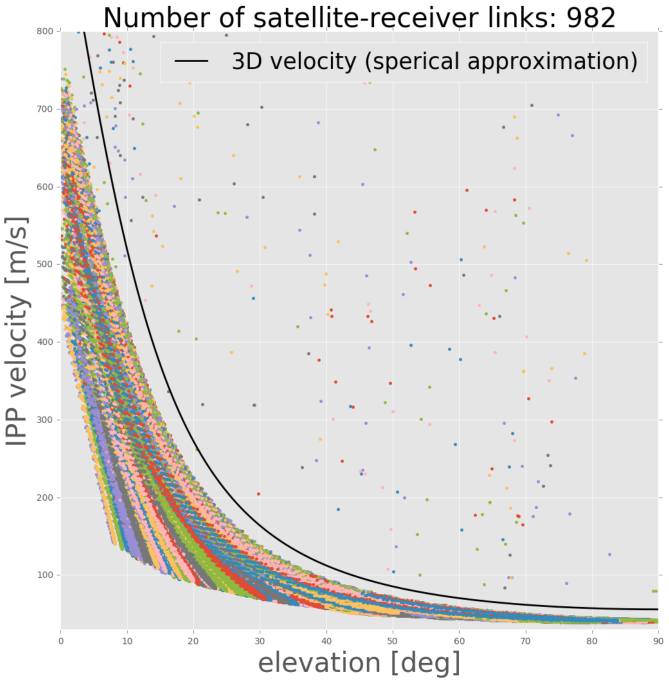

Figure 3.4.2: The IPP velocity magnitude increment for low elevation angles is clearly visible for 982 satellite-receiver links. The black curve represents the modeled IPP velocity using an Earth spherical approximation algorithm described in section 3.4.

using an Earth spherical approximation 3.4.1.2. An increment of the $\vec{V}_{ipp}$ magnitude for low elevation angles is clearly visible for a big data set of observations (982 satellite-receiver links).

In other words, IPP accelerates when the satellite rises or sets. This has two main consequences: sTEC observations experience a Doppler shift which varies with time; trends and higher background noise appear for lower elevation angle in the GNSS sTEC observations.

3.4.2 DOPPLER EFFECT

The fact that the IPP moves with a certain velocity $\vec{V}_{ipp}$ implies the fact that any ionospheric perturbations detected from GNSS remote sensing observations ex-

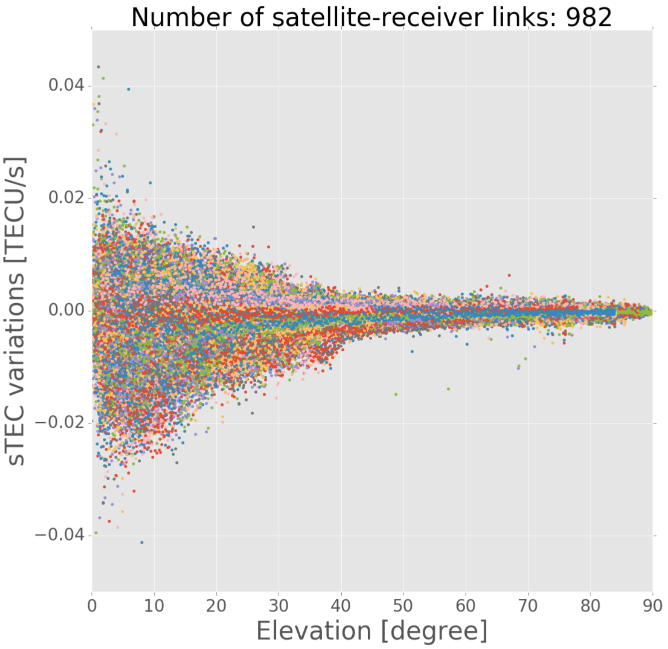

Figure 3.4.3: The sTEC variations dispersion increment for low elevation angles is clearly visible for 982 satellite-receiver links.

perience a Doppler shift.

Recalling the concept seen in 3.1.1, when an earthquake occur, direct (or shock) acoustic waves are produced in the proximity of the epicenter. These pressure waves, upon reaching the ionosphere, will locally affect electron density through particle collisions between the neutral atmosphere and the electron plasma [43]. An observer moving with a velocity $\vec{V}_{ipp}$ will "hear" a frequency

$$f_{observed} = \frac{v + V^{s}_{ipp}}{v} f_{source} \tag{3.13}$$

where v is the value of the sound speed at a certain temperature T, and V^{s}_{ipp} is the velocity component along the source direction.

If we consider the ionospheric height to be located at 350 km, the acoustic wave to have a frequency of 8.33 mHz, the V^{s}_{ipp} to be 300 m/s, then the observed fre-

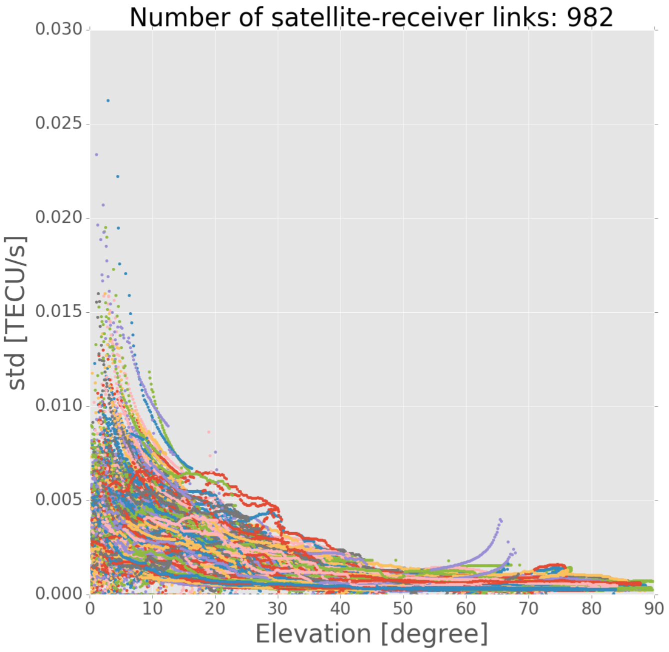

Figure 3.4.4: The sTEC observations background noise increment for low elevation angles is clearly visible for 982 satellite-receiver links.

quency $f_{observed}$ have a value of 1.21 mHz, which means a change of about 45 percent from the f_{source} value. Since the $\vec{V}_{ipp}$ has not a constant value with time, also $f_{observed}$ will change with time.

3.4.3 TRENDS AND NOISE

The fact that the module of the vector $\vec{V}_{ipp}$ changes with elevation, imply the fact that the term $\vec{V}_{ipp} \cdot \nabla sTEC^b$ of equation 6.1 becomes significant below 40 degrees elevation angle. This term represents the spatial trend's component in the sTEC observations (see Fig. 3.4.3). This section presents a statistical analysis over 186 receivers located in New Zealand (see Fig. 4.4.1 from section 4.4). For this analysis we considered the day September 9, 2017, which had not particular strong geomagnetic activity. Fig. 3.4.3 shows sTEC variations vs satellite elevations angle. Fig. displays a running standard deviation computed on a moving windows

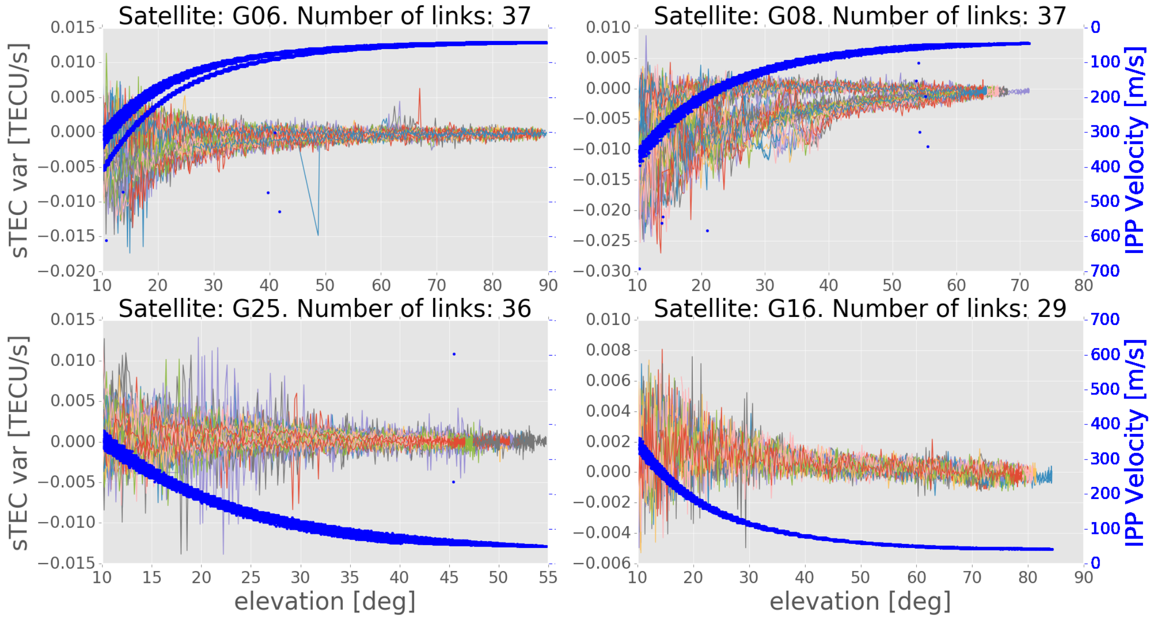

Figure 3.4.5: *sTEC* variations and $\vec{V}_{ipp}$ magnitude (blue) plotted as a function of elevation angle. The four panels show 4 different satellites in view from different stations (different colors). It is clear a strong correlation between the $\vec{V}_{ipp}$ magnitude and the *sTEC* variations.

of 60 consecutive epochs. An increment in the noise for low elevation angles is clearly visible for 982 satellite-receiver links.

Fig. 3.4.5 shows the impact of the IPP motion on the GNSS sTEC observations, which is highly correlated with the time evolution of the IPP velocity (see Eqn. 6.1). The four panels show 4 different satellites in view from different stations (different colors). The blue line represents the $\vec{V}_{ipp}$ magnitude computed in real-time (see section 3.4.1.1).

Table 3.4.1 shows the mean standard deviation computed on subsets of *sTEC* observations sorted by common elevation angle ranges. A significant increment of the background noise is clearly visible starting from $E \approx 40[deg]$.

Table 3.4.1: Mean standard deviation computed for different elevation angle ranges. A significant increment of the background noise is clearly visible starting from $E \approx 40[deg]$.

Intervals [deg]	***90 - 80***	***80 - 70***	***70 - 60***	***60 - 50***
Mean std [TECU/s]	0.000369	0.000389	0.000394	0.000438
50 - 40	***40 - 30***	***30 - 20***	***20 - 10***	***10 - 0***
0.000497	0.000734	0.001209	0.002047	0.003153

Oh! Responsive, too! In real time! I love it!

Rick and Morty [1.04]

4

VARION Case Studies in Real-Time Scenario

The notion that gravity waves generated by tsunami waves (even with wave heights of few centimeters in deep ocean) can propagate upward in the atmosphere and ultimately cause perturbations in the total electron content (TEC) of the ionosphere was first established by Daniels [19], and was theoretically further developed by Hines [34], [35]. Peltier and Hines [68] subsequently showed that these TEC variations can be detected through ionosonde measurements.

Using this solid foundation and the abundance of GPS observations, researchers have set out goals to develop models and establish observational systems to provide reliable tsunami forecasts before the actual tsunami waves reach coastlines. It has been demonstrated that effects of an ocean tsunami can potentially be remotely observed as traveling ionospheric disturbances (TIDs) produced by the gravity waves. These TIDs were detected using different methods of observations, including ground-GPS [4], [77], [27], Jason-1 radar altimeter [65], [53], incoherent scatter radar (ISR) [48] and space-based measurements [17] and [94].

Additional investigations highlighted that the detection of tsunami-driven TIDs is not always straightforward since there exists several other causes for TIDs, such as intense or large-scale tropospheric weather [36], [41],[93], geomagnetic and auroral activity [74], [61], earthquakes [23], [2], [42], and even unknown mechanisms [88]. Therefore, the relationship between detected TIDs and those that are induced by a tsunami has to be proven, for example by verifying that the horizontal speed, direction and spectral bandwidth of the TIDs match that of the ocean tsunami [27].

While there has been progress in experimental work, along with theoretical modeling of the interactions between the ocean surface, atmosphere, and ionosphere [65], [63], [64], [33], [56], recent reviews [39] and [46] concluded that the core scientific problems regarding the nature of the coupling between the ocean and ionosphere are still not sufficiently understood. To provide useful geophysical data on the inferred amplitude, period, and velocity of a tsunami, based on the estimated gravity waves induced TIDs, a number of real-time TEC monitoring systems are being developed utilizing the present capabilities of GNSS technology and infrastructures. As a matter of fact, up to now TEC variations are routinely estimated and geolocated in a post-processing mode.

The existing tsunami warning systems currently rely on numerical modeling (as MOST) and buoy observations [27]. Since the 2003 Rat Island tsunami, the NOAA Center for Tsunami Research (NCTR) has developed a real-time model-forecast methodology ingesting deep-ocean tsunami measurements into the MOST model to produce timely and accurate tsunami forecast for potentially vulnerable U.S. coastal communities [86], [80], [92], [91], [85]. As a major model component of this forecast system, MOST has been used to develop a database of tsunami propagation model results for nearly 2,000 unit tsunami sources covering all subducting zones on earth. Based on an inversion algorithm [69], the forecast method rapidly estimates the tsunami source to obtain a best fit between the pre-computed tsunami propagation database and the real-time tsunami measurements supported by a global tsunameter system composed of 65 deep-ocean bottom pressure sensors. Ground-GNSS observations processed in real-time may have the potential to enhance the current system by providing the tsunami speed and amplitude.

4.1 2012 HAIDA GWAII EVENT

4.1.1 INTRODUCTION

The work presented in this section was focused on real-time detection of the TIDs caused by tsunami atmospheric gravity waves with stand-alone GNSS Receivers [81]. Using the VARION algorithm (Section 3.3) we compute TEC variations at 56 GPS receivers in Hawaii as induced by the 2012 Haida Gwaii tsunami event. We used GPS observations collected at 56 Plate Boundary Observatory (PBO) sites located on the Hawaiian Islands (`https://www.unavco.org/instrumentation/networks/status/pbo`). All the GPS permanent stations are located in Big Island, (see Figure 4.1.1) and acquired observations at 15 and 30 seconds rate. We observe TEC perturbations with amplitudes of up to 0.25 TEC units and traveling ionospheric perturbations (TIDs) moving away from the earthquake epicenter at an approximate speed of 277 m/s. We perform a wavelet analysis to analyze localized variations of power in the TEC time series and we find perturbation periods consistent with a tsunami typical deep ocean period. Finally, we present comparisons with the real-time tsunami MOST (Method of Splitting Tsunami) model produced by the NOAA Center for Tsunami Research and we observe variations in TEC that correlate in time and space with the tsunami waves.

4.1.2 RESULTS AND DISCUSSION

We processed the GPS observations from the 56 PBO GPS stations to estimate TEC variations at 15 s and 30 s rate with both VARION and JPL algorithms [47]. These two algorithms are designed to directly estimate two different parameters.

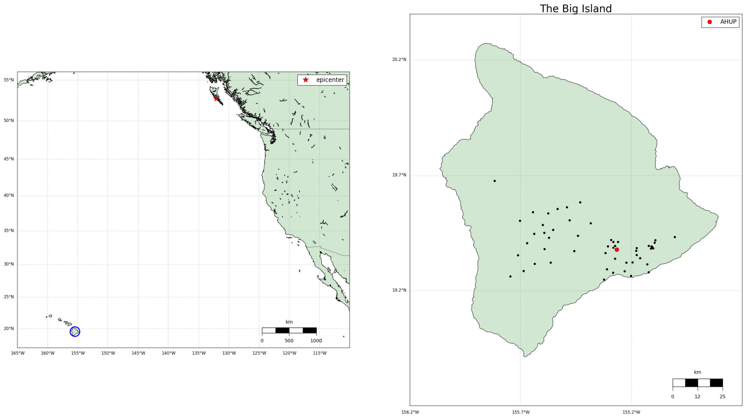

Figure 4.1.1: Map indicating the epicenter of the 10/27/2012 Canadian earthquake (left panel) and zoomed-in image of the Hawai'i Big Island, where all the 56 used GPS stations are located. The map has been generated using the matplotlib Basemap toolkit (Hunter, 2007 [37]).

The JPL algorithm is able to directly obtain the absolute TEC values, after estimating highly precise satellite and receiver Inter-Frequency Biases (IFBs) using about 200 GPS receivers distributed worldwide [e.g., refs [54], [55]]. On the other hand, the direct outputs of the VARION algorithm are the sTEC total derivative (Equation 3.5), subsequently integrated over a certain time period; the variometric approach overcomes the problem of estimating the phase initial ambiguity and the IFBs, thus being ideal for real-time applications. In order to highlight the TIDs, the TEC time series for each satellite were filtered to remove the TEC low-frequency variations (such as diurnal variations and multiple hour trends due to changing satellites elevation angles); VARION results were filtered using an 8th order polynomial, while the JPL algorithm uses a band-pass filter (0.5 to 5 mHz) [95].

Figure 4.1.2 shows the sTEC time series for two hours (08:00 to 10:00 UT - 28 October 2012) for 7 satellites in view from the AHUP station obtained with the two approaches. The vertical black line represents the time when the tsunami arrived at the Hawaiian Islands according to the MOST model. Very good agreement

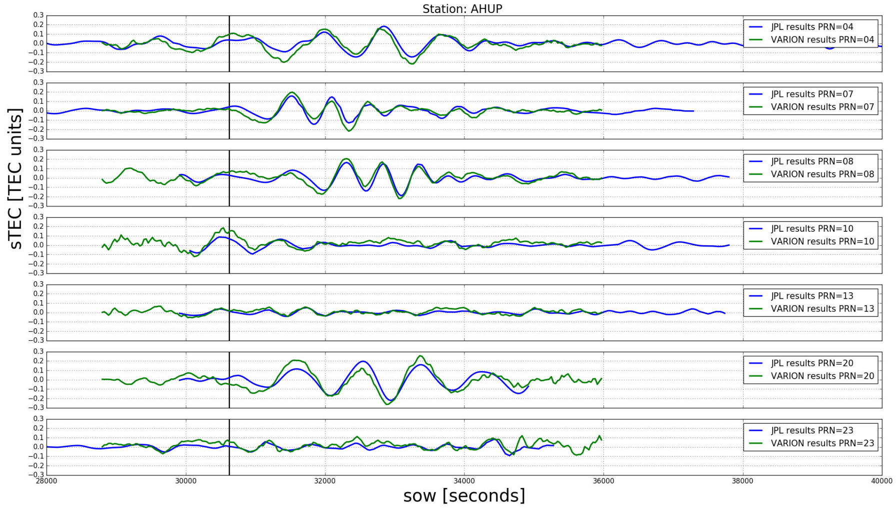

Figure 4.1.2: Comparison between TEC time series obtained from the VARION and JPL techniques. The TEC variations are computed for 7 satellites (PRNs 4, 7, 8, 10, 13, 20, 23) in view from the AHUP station on the Hawaiian Islands (latitude: 19.379 degrees, longitude: −155.266 degrees, height: 1104.881 meters). The black vertical line represents the time when the tsunami reached the Hawaiian Islands. TIDs were clearly detected, with good agreement between the two approaches.

(RMS differences at the level of few hundredths TEC units) is evident, the differences are mostly due to the different data filtering methods applied. Moreover, we see significant TIDs for 5 satellites (PRNs 4, 7, 8, 10, 20) at different times due to the different locations of the ionospheric piercing points (IPPs) and the sub-ionospheric points (SIPs : IPPs projections onto the ellipsoid). In particular, for the satellite PRN 10 the TEC perturbation occurred before the tsunami reached the Hawaiian Islands; this is in fact due to the geometry corresponding to the particular elevation and azimuth angles of satellite PRN 10 as the tsunami-generated TIDs were detected when tsunami the wave front was still about 150 km away from the coast. For satellites PRN 13 and 23 no significant TIDs were detected, likely due to elevations and azimuthal positions with respect to the tsunami as a possible cause of the TIDs. We performed a wavelet analysis using the Paul wavelet (that gives better time localization than the Morlet one) and we determine both the dominant modes of variability and how those modes vary in time [87]. This technique allows us to highlight and evaluate the TIDs wave periods. Here, the wavelet analysis has been performed in python using scripts running the wavelet software provided by C. Torrence and G. Compo, and available at `http://atoc.colorado.edu/research/wavelets/`. We processed 260 sTEC time series, for all the satellites in view at the 56 GPS permanent stations. We found periods in the range of 10 to 30 minutes, similar to the periods of the tsunami ocean waves, which can range from 5 min up to an hour with the typical deep ocean period of only 10-30 wavelengths around 400 km, and the velocity approximately 200 m/s.

Figures 4.1.3 / 4.1.4 show the sTEC time series wavelet analysis for the 7 satellites in view at the station AHUP. The upper panels show the sTEC time series obtained with the VARION software in a real-time scenario, as plotted in Figure 4.1.2. The bottom panels indicate the wavelet spectra. The colors represent the intensity of the power spectrum and the black contour encloses regions of greater than 95 % of confidence for a red noise process. We can identify 5 satellites (PRNs 4,7,8,10,20) with peaks consistent in time and period with the tsunami ocean waves. These results clearly show TIDs appearing after the tsunami reached the islands.

Figure 4.1.5 displays a map of the region around the Hawaiian Islands, the area of our focus in order to highlight the most significant sTEC variations. The colored tracks show the positions of the SIPs (equal to corresponding IPPs, when seen on the map) for each of the 7 satellites considered in Figure 4.1.2 as seen from the 56 GPS permanent stations during an observation span of two hours (8:00 to 10:00 UT, 28 October 2012). The colors represent the variation in sTEC, obtained by VARION processing; the TIDs are clearly visible in the interval of significant sTEC variations (from positive to negative values and vice-versa).

Figure 4.1.6 shows time sTEC variations for two hours (08:00 to 10:00 UT – 28 October 2012) at the IPPs vs. distance from the Haida Gwaii earthquake epi-

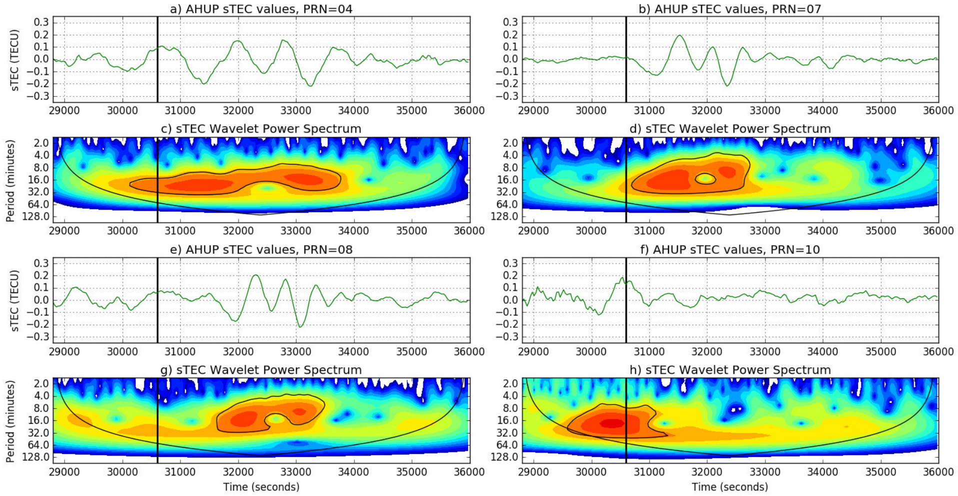

Figure 4.1.3: (a), (b), (e), (f) Four of 260 time series used for the wavelet analysis, station AHUP, satellite PRN 4,7,8,10. (c), (d), (g), (h) The wavelet power spectrum used the Paul wavelet. The vertical axis displays the Fourier period (in min), the horizontal axis is time (s). The black vertical line represents the time when the tsunami reached the Hawaiian islands. The color panels represent the intensity of the power spectrum; the black contour encloses regions of greater than 95% confidence for a red-noise process with a lag-1 coefficient of 0.72 [87]; the external black line indicates the " cone of influence" , the limit outside of which edge effects may become significant. We clearly see the increase of the power spectrum for periods between 10 and 30 minutes during the TIDs.

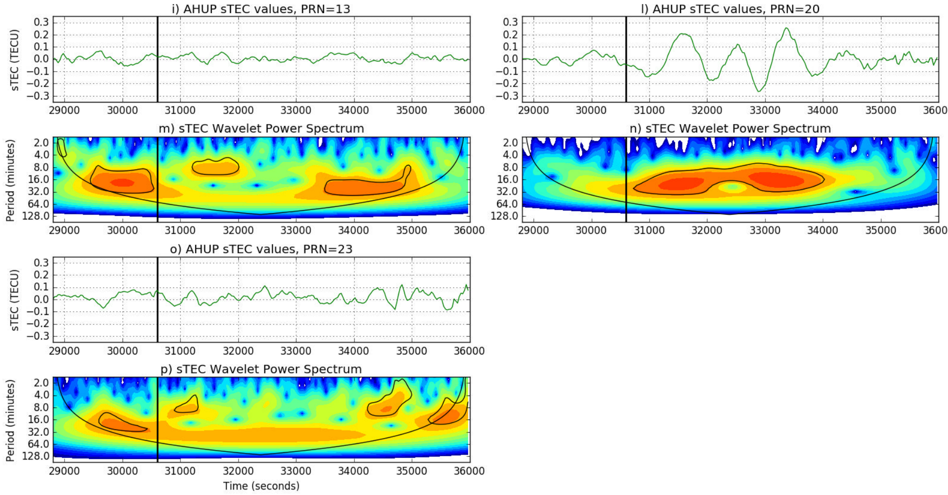

Figure 4.1.4: (i), (l), (o) Three of 260 time series used for the wavelet analysis, station AHUP, satellite PRN 13,20,23. (m), (n), (p) The wavelet power spectrum used the Paul wavelet. The vertical axis displays the Fourier period (in min), the horizontal axis is time (s). The black vertical line represents the time when the tsunami reached the Hawaiian islands. For satellites PRN 13 and 23 we do not see significant increase of the power spectrum for periods between 10 and 30 minutes during the TIDs.

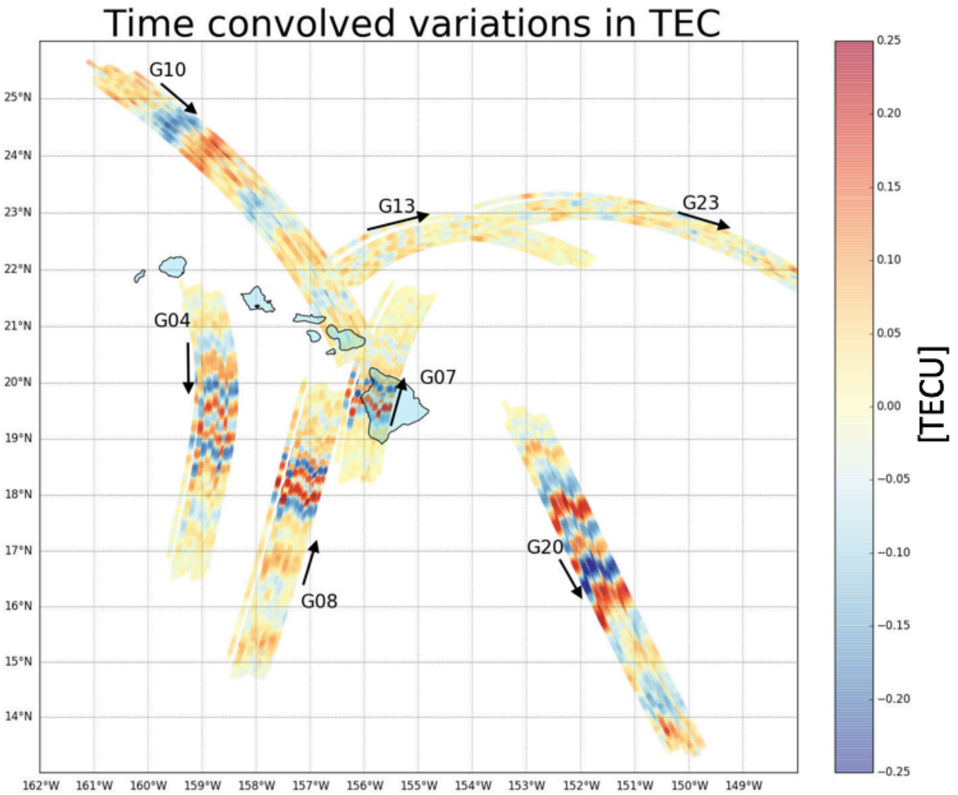

Figure 4.1.5: Space–time sTEC variations for two hours (08:00 to 10:00 UT – 28 October 2012 – cut–off angle set to 18^o) at the SIPs (same positions of the corresponding IPPs on the map) for the 7 satellites seen from the 56 Hawaii Big Islands GPS permanent stations, after the Haida Gwaii earthquake. The TIDs are clearly visible in the interval of significant sTEC variations (from positive to negative values and vice-versa). It is also shown that PRN 10 detected TIDs prior to the tsunami arrival at Hawaii Islands (08:30:08 UT). The map has been generated using the matplotlib Basemap toolkit (Hunter, 2007 [37]).

center, for the same 7 satellites under consideration. The TIDs are clearly visible in the interval of significant sTEC variations (from positive to negative values and vice-versa). The vertical and horizontal black lines represent the time (when the tsunami arrived at the Hawaii Islands) and the distance (between the epicenter and the Big Island), respectively. In this way, we identify the green rectangle as the alert area and it is evident that satellite PRN 10, the closest to the earthquake epicenter detected TIDs before the tsunami arrived at Hawaiian Islands (08:30:08 UT). In the distance vs time plots (also called hodochrons) the slope of the straight line, fitted considering corresponding sTEC minima for different satellites, represents the horizontal speed estimate of TIDs. This plot indicates that the linear least-squares estimated speed of the TIDs is about 316 m/s and it is found to be in good agreement with a typical speed of the tsunami gravity waves estimated with ground-based GNSS receivers (see Appendix B). We note that such speed determinations via hodochron are not available in real-time, but neither are these estimates needed for real-time tsunami detection.

Figure 4.1.7 displays a sequence of maps of the region around the Hawaiian Islands showing the variations in sTEC (determinable in real-time) at IPP/SPI locations on top of the MOST model sea-surface heights. Note that, just as the MOST model wavefronts are moving past the IPPs, the sTEC variations in the region become pronounced, correlated with the passage of the ocean tsunami itself. In particular, at 08:22:00 GPS time (08:21:44 UT) we are able to see sTEC perturbations from 56 stations looking at satellite PRN 10. The propagation of the MOST modeled tsunami passes the ionospheric pierce points located NW of the Big Island and offers insight with regard to the ionospheric response to the tsunami-driven atmospheric gravity wave. These perturbations are detected before the tsunami reached the islands as seen from the locations of the SIP points. The following frames indicate the tsunami-driven TIDs detected from the other 4 satellite (PRNs 4,7,8,20) tracking the propagating tsunami (see supplementary video SV1 online).

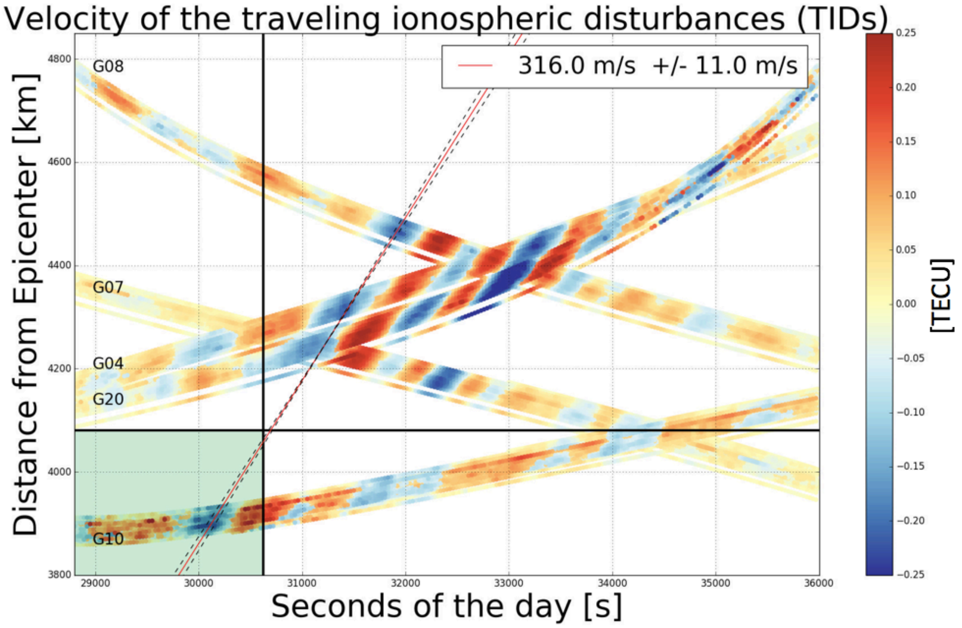

Figure 4.1.6: sTEC variations for two hours (08:00 to 10:00 UT – 28 October 2012) at the IPPs vs. distance from the Haida Gwaii earthquake epicenter, for the 7 satellites observed from the 56 Hawaii Big Islands GPS permanent stations. The TIDs are clearly visible in the interval of significant sTEC variations (from positive to negative values and vice-versa). The vertical and horizontal black lines represent the time (when the tsunami arrived at the Hawaii Islands) and the distance (between the epicenter and the Big Island), respectively; it is evident that PRN 10 detected TIDs before the tsunami arrived at Hawaii Islands (08:30:08 UT). The slope of the straight line fitted, considering a linear least-squares regression for corresponding sTEC minima for different satellites, represent the TIDs mean propagation velocity.

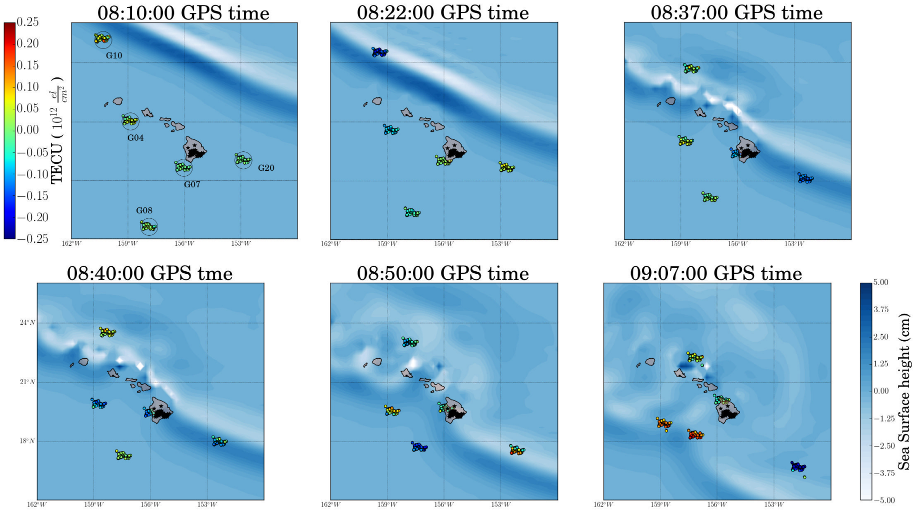

Figure 4.1.7: Space-time sTEC variations at 6 epochs within the two hours interval (08:00 to 10:00 UT – 28 October 2012) at the SIPs for the 5 satellites showing TIDs, over-plotted the tsunami MOST model. TIDs are consistent in time and space with the tsunami waves. The maps have been generated using the matplotlib Basemap toolkit [37].

Under the flat Earth hypothesis, it is possible to show that there is a direct dependence of the TID estimated speed on the modeled ionospheric layer height. Taking into account Figure 4.1.8, where the subscript e and r represent estimated and real values, the estimated TID speed v_{tide} using ground-based GNSS observations will no necessary be equal to the real TID speed v_{tidr}. The two values are directly proportional as shown in Eqn. 4.1.

$$\frac{v_{tide}}{v_{tidr}} = \frac{h_{model}}{h_{real}} = r \tag{4.1}$$

where r represents the ratio between the modeled ionospheric height layer the height at which we have the maximum of the electron density, respectively.

In particular, the ionospheric shell height used in this case has a constant value of 350 km while the electron density profiles obtained using, e.g., the International Reference Ionosphere (IRI), a standard empirical model of the global ionosphere

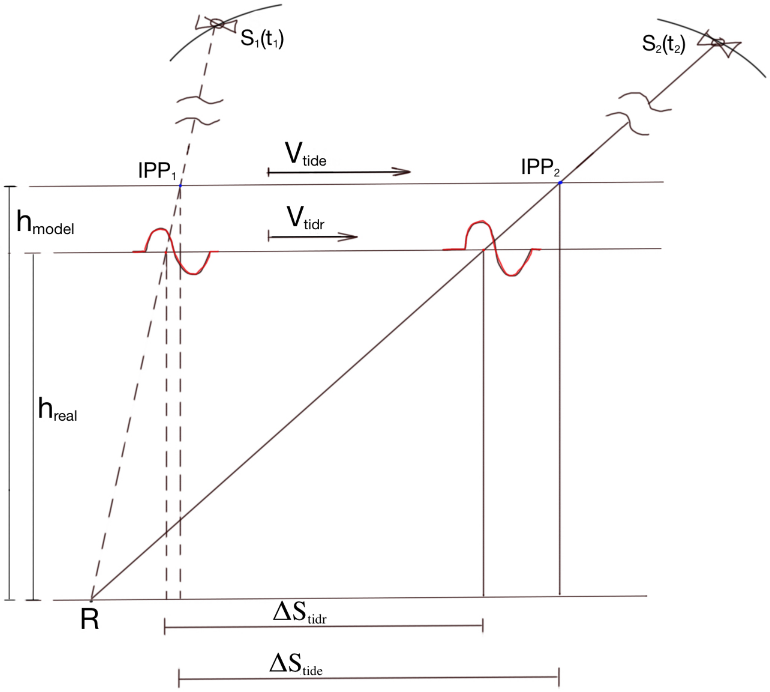

Figure 4.1.8: Schematic representation of the TID detection at t_1 and $t_2 = t_1 + \Delta t$ by two different satellites S_1 and S_2. R represents the receiver, h_{model} and h_{real} represent the modeled ionospheric layer and the real ionospheric layer. In this case the two layers are located at 300 and 350 km, respectively.

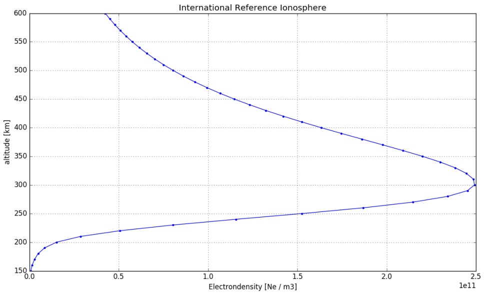

Figure 4.1.9: Electron density profile obtained with the IRI model computed at the Hawai'i Big Island (10:00 UT - 28 October 2012). The model indicates a maximum electron density value to occur at 300 km.

(available at `http://omniweb.gsfc.nasa.gov/vitmo/iri_vitmo.html`), indicates a maximum electron density value to occur at 300 km (see Figure 4.1.9). If we consider the TID speed to be almost equal to the tsunami speed, we can conclude that the best TID speed estimation using GNSS observations will be around 300 m/s.

4.1.3 CONCLUSIONS

We have found observational evidence of variations in GPS sTEC measurements in the range of $0.1-0.2$ TEC units (on the order of 1% of the background TEC value) that are associated with the Haida Gwaii tsunami of 28 October 2012. We compared two independent signal processing techniques, one available in real-time and one available in post-processing, and a good agreement was found between the JPL (post-processed) and VARION (real-time capable) results. We performed a wavelet analysis and we observed sTEC variations with a typical period between 10 and 30 minutes, consistent with the ocean tsunami waves. We estimated the speed of the TIDs generated by the tsunami-driven IGWs and we found a typical speed of about 316 km/s. From the comparison between the MOST model results and TECs measurements we have validated our results in time and space. Using signals from 56 GPS stations located on the Hawaiian Islands, we have detected

TEC perturbations before the actual tsunami arrival; this is due to the geometry of the satellite PRN 10 (elevation and azimuth angles) and so the position of the SIPs at that time.

We have demonstrated that the real-time capable VARION algorithm is able to detect the TIDs generated by tsunami-driven gravity waves and may be considered as a novel contribution to future integrated operational tsunami early warning systems.

We are currently implementing the VARION algorithm in JPL's Global Differential GPS System (GDGPS) providing real-time access to 1-Hz data streams from about 30 global real-time stations collecting data from multiple constellations including GPS, Galileo, GLONASS and BeiDou (see Section 5.3). With real-time streams of data the polynomial fit has been implemented as a finite duration impulse response (FIR) high-pass filter (see Section 5.1).

A real-time tsunami detection system could be designed using VARION combined with real-time data from different sources (e.g. seismometers, buoys, GNSS receivers). Once an earthquake is detected in a specific location, such a system will begin processing the real-time TEC outputs using multiple stations located near the epicenter searching for ionospheric signals that may be correlated with the tsunami propagation. The measurements would be collected and processed by a central processing facility also providing risk assessments and maps related with a particular earthquake event. The use of multiple independent data types will be expected to contribute significantly to the robustness of the system.

4.2 2015 Chile Earthquake and Tsunami Event

This section summarize the results for the 2015 Chile event which I obtained in collaboration with Michela Ravanelli during her M.Sc. thesis, when I was Michela's thesis coadvisor. In this study, both the VARION (Section 3.3) and the VADASE algorithm (Section 2) were applied in order to estimate in real time the earthquake-induced sTEC variations and ground shacking, respectively.

4.2.1 Introduction

On September 16, 2015, a 8.3 magnitude earthquake was registered in Central Chile, 46 km West of the Illapel city, (31.570°S, 71.654°W, depth of 25.0 km). It occurred at 22:54:32 UTC, generating a tsunami observed all over the Pacific region and causing serious damages in the areas affected. Amidst all the destruction and chaos, this event allowed the gathering of data related to the sTEC variation caused by the earthquake itself (CID), giving us the opportunity to improve our knowledge of the phenomena involved and also to test the VARION algorithm.
Dataset. GPS observations were collected from a dataset of about 90 stations spread all over the South American continent. The GPS stations located in Chile were provided by *Centro Sismológico Nacional, Universidad de Chile*, while the data of the other stations were collected from *International GNSS service* (IGS) or from *Système d'Observation du Niveau des Eaux Littorales* (SONEL) network. These GPS receivers collected data at 15 and 30 second rate.

4.2.2 Results and Discussion

4.2.2.1 Ionosphere Response

sTEC time series were analyzed during the time interval ranging from 22:45:00 to 23:59:59 UTC. Observations at middle-high elevations (elevation cut-off angle of 20 °) were used in this study.
In order to highlight possible asymmetry in the ionospheric response to the earthquake, the area of study was split into six parts, being he epicenter the center of the area, as it is possible to see in Figure 4.2.1. The oblique straight lines, dividing the third region from the fourth one and the fifth region from the sixth one, have an inclination of 45 degree (they are the bisector lines of the quadrants).

Subsequently hodochrons were plotted accounting for the IPP located in each different region. Hodochrons are a particular kind of graph in which sTEC variations at the IPPs are represented in a time vs distance from the epicenter plot. The colors represent the variation in sTEC, obtained using the VARION algo-

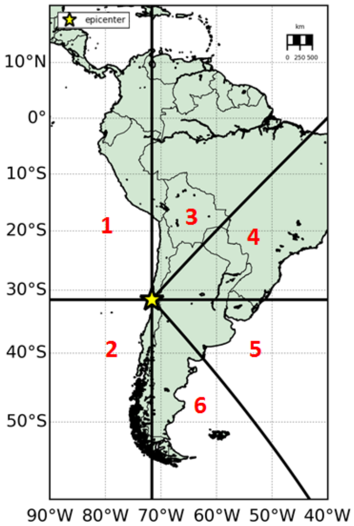

Figure 4.2.1: This map shows the six areas of study chosen for the 2015 Chile event. The epicenter of the earthquake occurred at 31.570°S, 71.654°W, depth of 25.0 km

rithm. The vertical black line denotes the time of the earthquake occurrence. The hodochrons of each region are depicted in Figure 4.2.2. It is clear that the hodochrons for the northern regions (the first, the third and the fourth zone) better highlight the phenomena under investigation than the ones of the southern regions (the second, the fifth and the sixth zone).

Indeed, in the northern areas a well-defined variation in sTEC is shown, characterized by an oblique pattern involving both minimum (blue pattern) and maximum (red pattern) values. By interpolating this oblique pattern with a straight line, whose slope represents the phenomenon speed, it is possible to determine the disturbance velocity. These velocity magnitudes fall within the range of 600 - 760 m/s and are consistent with the physical phenomenon as it possible to notice in Figure 4.2.3.

The hodochrons show a clear north - south asymmetry in the ionospheric perturbation. According to [31], such directivity may be due to the interaction of the

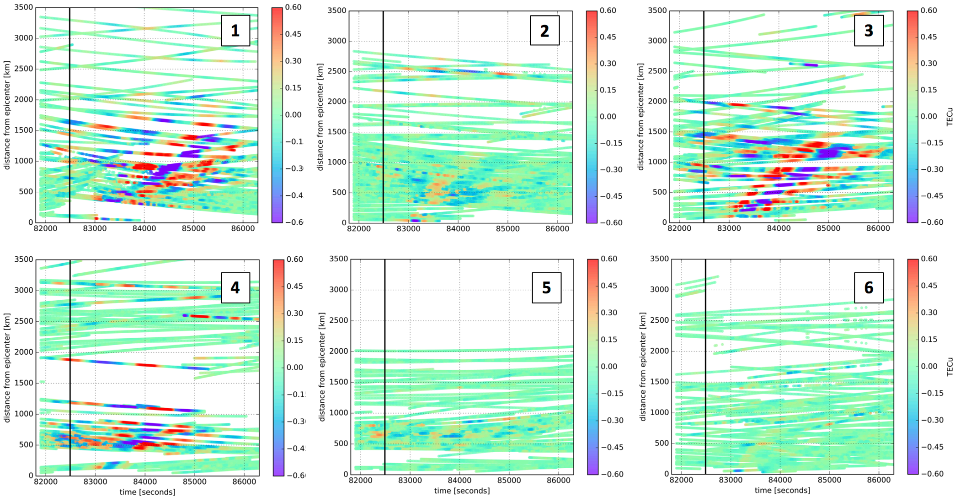

Figure 4.2.2: Hodochron plots computed for the 6 regions identified in 4.2.1. It is clear that regions 1, 3, and 4, show a stronger ionospheric perturbation.

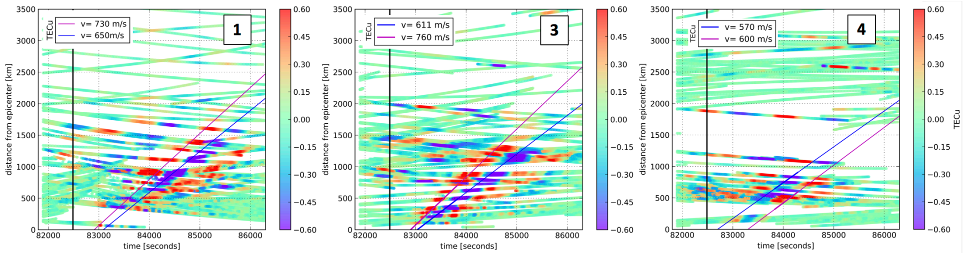

Figure 4.2.3: Hodocron plots for regions 1, 3, and 4. The slope of the interpolating lines represent the horizontal velocity of the CIDs. A value around 600 - 760 m/s is clearly visible.

local geomagnetic field or to the azimuthal difference in energy emission in terms of seismic waves. Next section focuses on the study of the second possible cause, and a dedicated procedure was developed to calculate the energy released by the earthquake.

4.2.2.2 Earthquake Energy

In order to estimate the energy released by the earthquake, we processed high-rate GNSS observations (1 Hz) from the same network. These observations were used as input for the VADASE algorithm, which estimates the receiver velocities for the East, North and Up components.

We reduced the East and North components into a single horizontal component. Using Pitagora, we compute the magnitudes of the 2D vector velocity, which represent the shacking of the receiver in the horizontal plane. We applied the F-test of equality of variances [52] to the magnitude of this vector in order to compute the earthquake's duration. In fact, we assume that the population (in this case the horizontal component of the velocity), follows a normal distribution before and after the arrival of the surface waves. This F-test compares the ratio of two variances as reported in Eq. 4.2.

$$F = \frac{S_X^2}{S_Y^2} \tag{4.2}$$

where S_X^2 and S_Y^2 represent the variance of two independent samples taken from two normal distributed populations. In our case, the F test is represented by the ratio between the sample variances computed on 60 values (1 min) before and after the earthquake, assuming that the background noise of the time series is the same before and after the earthquake. We compute the ratio between the variances of a moving window and the variance relative to a fix window before the earthquake time. Choosing a significance level of 1% ($a = 0.01\%$), the test statistic must be lower than 1.84 in order to accept the hypothesis of variance equality (Eq. 4.3).

$$F = \frac{S_{after}^2}{S_{before}^2} < 1.84 \tag{4.3}$$

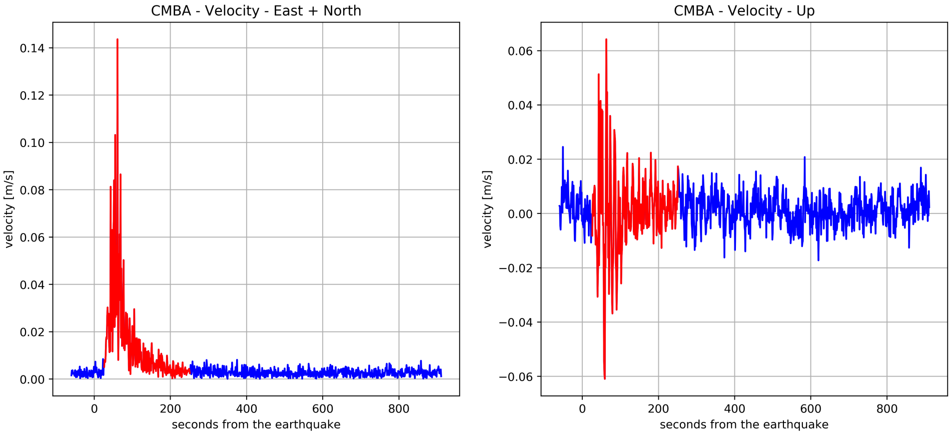

Figure 4.2.4: Horizontal component (left panel) and the Up component (right panel) of the estimated velocity for station CMBA. The red sections of the time series indicate the time interval (around 3 min) when the earthquake was statistically detectable from the GNSS time series.

We assume that when this condition is false, the receiver is still shaking due to the earthquake waves. When this condition becomes true again, the earthquake waves passed and we can estimate the earthquake duration.

Figure 4.2.4 shows the horizontal component (left panel) and the Up component (right panel) of the estimated velocity for station CMBA. The red part of the time series indicates the time interval of the earthquake computed using the F-test. It is important to recall that this duration was evaluated on the planimetric component of the velocity only.

Several studies have shown a high correlation between the ground vertical displacements and seismo-ionospheric disturbance indicates that the Rayleigh ionospheric disturbance is the result of vertical ground motion at the solid Earth [38]. For this reason, for all the GNSS stations, we computed the Power Spectral Density (PSD) of the Up velocity component during the interval of the earthquake. The integral of the PSD over a frequency interval gives the mean-square value of the content of the signal within the frequency interval (this is known as Parseval's The-

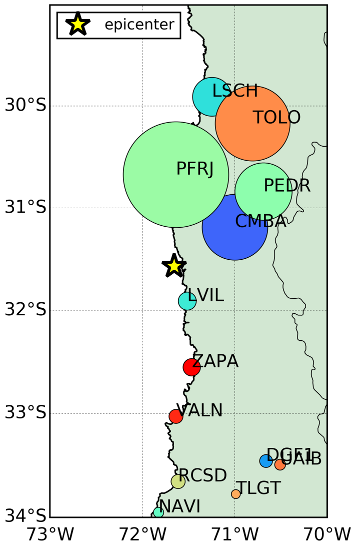

Figure 4.2.5: Rayleigh wave power distribution after the 2015 Chilean earthquake. The size of the markers is proportional to the RMS computed on the Up component of the velocity.

orem). So to get the RMS (root-mean-square) value of a signal from its PSD, we can just compute the area under the PSD and take the square root. The RMS represents the average power of a signal. For this reason, by integrating the PSD with respect to the frequency range and then taking the square root, we can compute the average power of the surface waves in a specific frequency range. In this study, since we are interested in the acoustic waves generated by the Rayleigh waves, we considered a frequency range greater than cut-off frequency for the acoustic waves (around 3 mHz, see section 3.1.1).

Figure 4.2.5 is a representation of the power release from the Rayleigh waves at different locations. The GNSS stations near the epicenter were plotted using a marker's size proportional to their RMS.

4.2.3 Conclusions

It is clear a north-south asymmetry in sTEC perturbations. We showed that this asymmetry can be linked to the different Rayleigh waves power in the Up component of the shaking.

4.3 2013 U.S. EAST COAST METEOTSUNAMI EVENT

4.3.1 INTRODUCTION

The work presented in this section was focused on real-time detection of the TIDs caused by meteotsunami using stand-alone GNSS Receivers.

Meteotsunamis are tsunami-like waves of meteorological origin, rather than of seismic origin. On June 13, 2013, around 15:00 UTC, a storm exited eastward off the New Jersey coastline. The storm had triggered an ocean wave that traveled eastward and reflected off the continental shelf break, causing waves to propagate back to the U.S. East Coast. A huge area was affected, and several NOAA water level stations located along the New Jersey and New England coasts as well as in Bermuda and Puerto Rico captured the meteotsunami oscillations [see [8] for the more technical information].

This section describes the storm that caused the meteotsunami and examines the ionospheric disturbances using the VARION algorithm (Section 3.3) to compute TEC variations at 18 GNSS stations located along the U.S. east coastline. Here we present a first preliminary attempt to detect metotsunamis from the ionosphere using ground-based GNSS receivers.

East Coast meteotsunamis are relatively common, and the coast is at a higher risk of a meteotsunami than a tsunami. Until now, due to the complexity of these events, a reliable forecasts/warnings system has not yet been developed for meteotsunami. In general, these events occurred from a traveling atmospheric disturbance generating a wave that propagated towards the shore, specifically an inlet with certain resonance properties that amplified the wave [see section 3.2.2].

4.3.2 FORMATION AND IMPACT

NOAA technical report [8] shows that the orientation of the line of thunderstorms at 15:00 UTC was parallel with the New Jersey coastline, showing that the force exerted on the water surface by the atmospheric disturbance covered a wide area. By 16:00 UTC the storm system had moved 60 km at a speed of 17 m/s. The average ocean depth was 25 to 50 m within that 60-km distance. This resulted in an ocean wave speed of 16 to 22 m/s, which matches the speed of the storm system. By 17:00 UTC the storm system moved 90 km at a speed of 25 m/s. The average ocean depth was 50 to 100 m, which resulted in an ocean wave of 22 to 31 m/s. The wave speed and storm speed also matched during this time period. Therefore, Proudman resonance was possible after the storm exited the coast.

Until 17:00 UTC, the ocean wave was moving away from the coastline and it would not have impacted the U.S. East Coast. The presence of the mid-Atlantic shelf break had a critical influence on the meteosunami direction. Between roughly 17:00 and 17:30 UTC, the storm system and associated ocean wave started to cross the continental shelf break. The shelf break lies approximately 100-120 km off the New Jersey coast. Here, the water depth increases from around 100 m to as much as 1200 m over a distance of only 20 km. The wave speed is directly proportional to depth; therefore a sharp increase in depth would result in a sudden increase in speed. This strong discontinuity in the phase velocity of the tsunami wave can be thought as a change of transmission medium and the shelf break as a interface between two media. Once the waves encountered the shelf break they reflected back towards the coast. This is one of the unique physical characteristics of a meteotsunami; the generation of a tsunami-like wave from a non-seismic offshore source.

4.3.3 Preliminary Results and Discussion

Let us split the analysis into 4 time periods.The first one being the undisturbed condition, when no signature in the ionosphere is expected; the second one starting from 13:00 to 17:00 UTC being the time period when the storm and ocean wave are moving away from the coastline; the third one from 17:00 to 18:40, being the time period when the meteotsunami is moving back towards the coast; and the last one being the end of the event.

Figures 4.3.1 and 4.3.2 show time sTEC variations for 10 hours (10:00 to 20:00

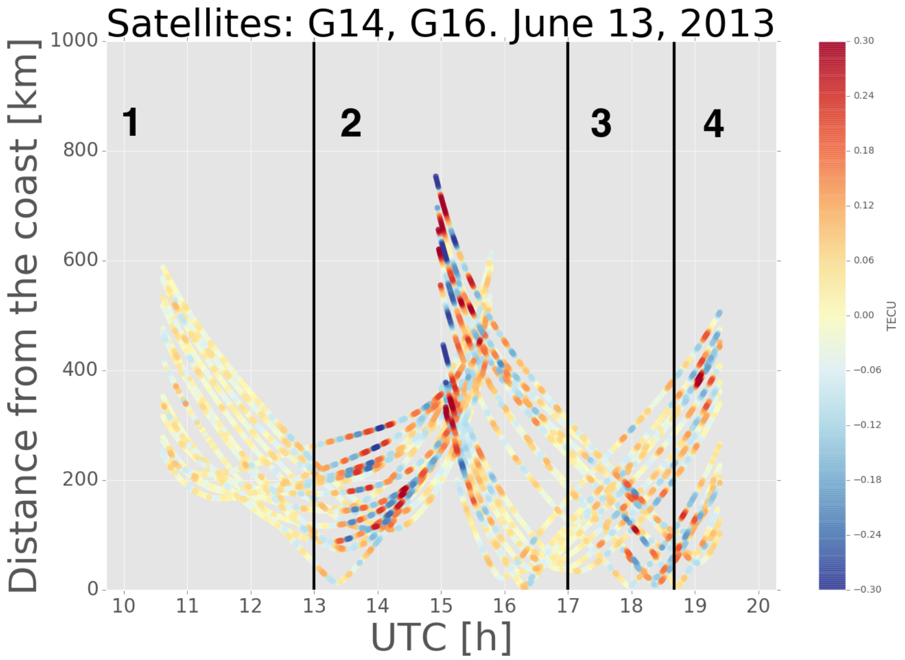

Figure 4.3.1: sTEC variations for ten hours (10:00 to 20:00 UT – 13 June 2013) at the IPPs vs. distance from the U.S. East Coast, for 2 satellites observed from the 18 U.S. GPS permanent stations. The 4 black vertical lines represent the time interval chosen for this analysis.

UT – 13 and 12 June 2013, respectively) at the IPPs vs. distance from the U.S. East Coast, for two satellites. TIDs moving away from the coastline are visible in the second time interval of the day 13 June 2013. The 4 black vertical lines represent the time interval chosen for this analysis.

Figure 4.3.3 displays a map of the region around the U.S. East Coast, the area of our focus in order to highlight the most significant sTEC variations. The colored tracks show the positions of the SIPs (equal to corresponding IPPs, when seen on the map) for each of 2 satellites considered in Figure 4.3.1 as seen from the 18 GPS permanent stations during an observation span of 10 hours (10:00 to 20:00 UT, 13 June 2013). The colors represent the variation in sTEC, obtained by VARION

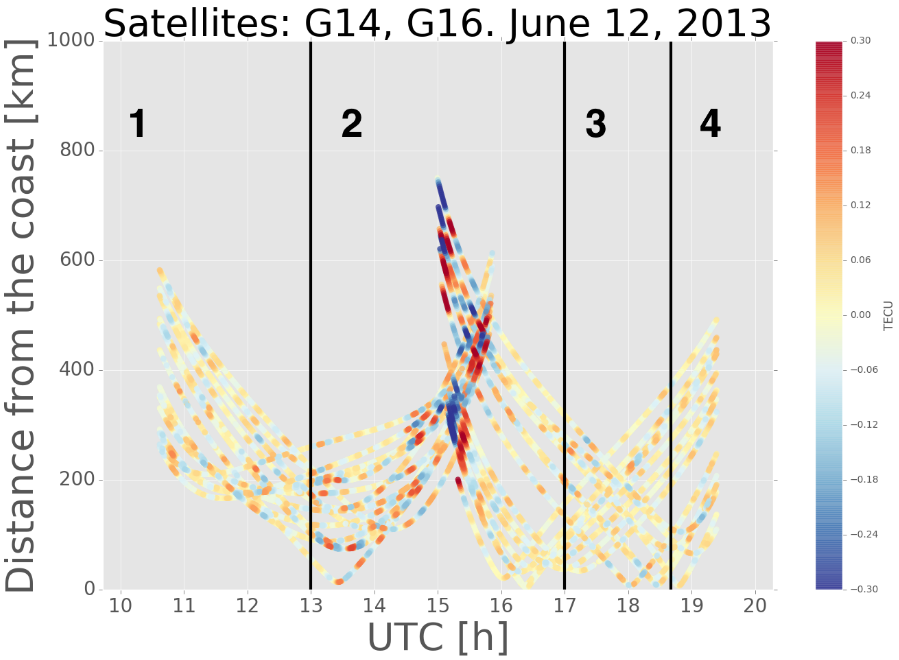

Figure 4.3.2: sTEC variations for ten hours (10:00 to 20:00 UT – 12 June 2013) at the IPPs vs. distance from the U.S. East Coast, for 2 satellites observed from the 18 U.S. GPS permanent stations. The 4 black vertical lines represent the time interval chosen for this analysis.

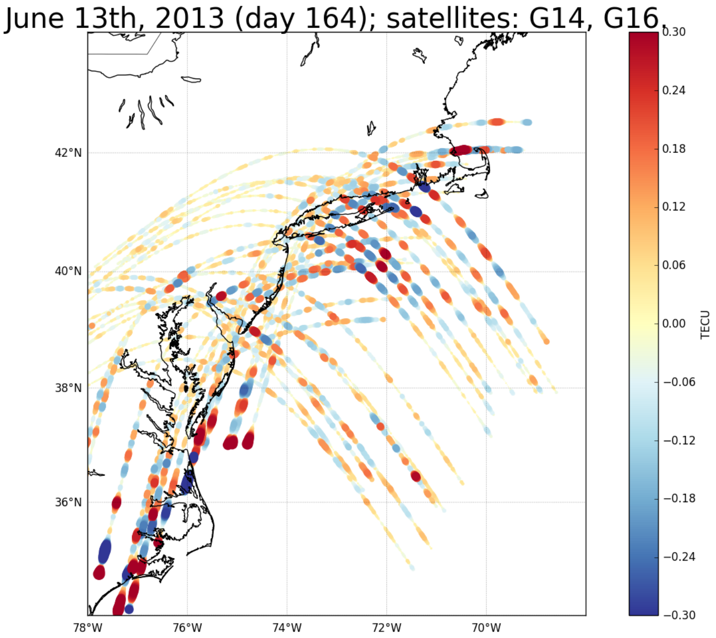

Figure 4.3.3: Space−time sTEC variations for 10 hours (10:00 to 20:00 UT − 13 June 2013 at the SIPs (same positions of the corresponding IPPs on the map) for 2 satellites seen from the 18 U.S. GPS permanent stations. The map has been generated using the matplotlib Basemap toolkit (Hunter, 2007 [37]).

processing.

4.3.4 CONCLUSIONS

We have found preliminary observational evidence of variations in GNSS sTEC measurements in the range of 0.1−0.3 TEC units during the Atlantic meteotsunami of 13 June 2013. We used the VARION software to estimate sTEC variations in real-time scenario. We performed a wavelet analysis and we observed sTEC variations with a typical period between 15 and 30 minutes, consistent with the ocean tsunami waves. More investigation have to be conducted in order to estimated the speed of the TIDs generated by the meteotsunami-driven IGWs.

4.4 2017, Mexico Tsunami and Geomagnetic Storm Events

4.4.1 Introduction

The work presented in this section was focused on the study of the ionospheric response to a tsunami event that occurred during a very strong geomagnetic storm. In fact, on September 8, 2017, two major events occurred simultaneously.

A Mw 8.1 earthquake offshore Chiapas, Mexico (15.068°N 93.715°W), occurred as the result of normal faulting at an intermediate depth, at 2017-09-08 04:49:21 UTC. Tsunami arrived at the Chatham Islands, New Zealand, in approximately 15 hours.

A Coronal Mass Ejection (CME) produced by the X9.3 solar flare on September 6, 2017, reached the Earth at 23:04 UTC on September 7, 2017. A strong geomagnetic storm (G3) started 23:25 and increased to severe (G4) at 23:50 UTC, according with NOAA Space Weather Prediction Center. On September 8, 2017, the geomagnetic K-index threshold of 8 was reached two times, at 01:51 and 13:06 UTC. An active warning for a severe G4 geomagnetic storm was issued by NOAA Space Weather Prediction Center. The area of impact was primarily poleward of 45 degrees Geomagnetic Latitude. Satellite navigation (GNSS) was expected to be degraded or inoperable for hours. Using the VARION algorithm (Section 3.3) we compute sTEC variations at 186 GNSS receivers in New Zealand as induced by the September 7, 2017 geomagnetic storm. We used GNSS observations from the GeoNet's continuous GPS network (cGPS) sites (`http://magma.geonet.org.nz/resources/network/netmap.html`). Most of the GNSS permanent stations are located in the North and South Islands, (see Figure 4.4.1) and acquired observations at 30 seconds rate.

Figure 4.4.2 shows the Auroral Electrojet (AE) [21], index during September 8th. The AE index is employed both qualitatively and quantitatively as a correlative index in studies of substorm morphology, the behavior of communication satellites, radio propagation, radio scintillation, and the coupling between the interplanetary magnetic field and the earth's magnetosphere. The effects of the geo-

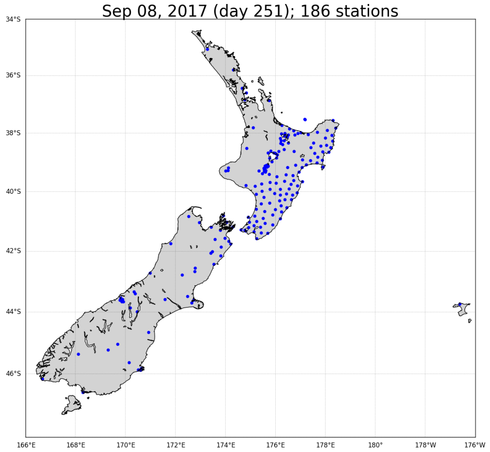

Figure 4.4.1: Map displaying the locations of the 186 GNSS stations from GeoNet. The map has been generated using the matplotlib Basemap toolkit (Hunter, 2007 [37]).

magnetic storm are clearly visible around 01:00 UTC and 13:00 UTC.

4.4.2 Results and Discussion

Figure 4.4.3 shows the sTEC variations computed using the VARION algorithm with a big data set composed by 7253 satellite-receiver links. A strong correlation between the AE index time evolution (Figure 4.4.2) and the sTEC variations is clearly visible.

Figure 4.4.4 displays 6 maps showing the space–time sTEC variations at the sIP (same positions of the corresponding IPPs on the map) for 6 satellites seen from the 186 New Zealand GNSS permanent stations, during the geomagnetic storm. The effects of the geomagnetic storm are clearly visible for all the satellites.

4.4.3 Conclusions

We have found clear observational evidence of variations in GNSS sTEC measurements in the range of 2–4 TEC units during the geomagnetic storm of 08 Septem-

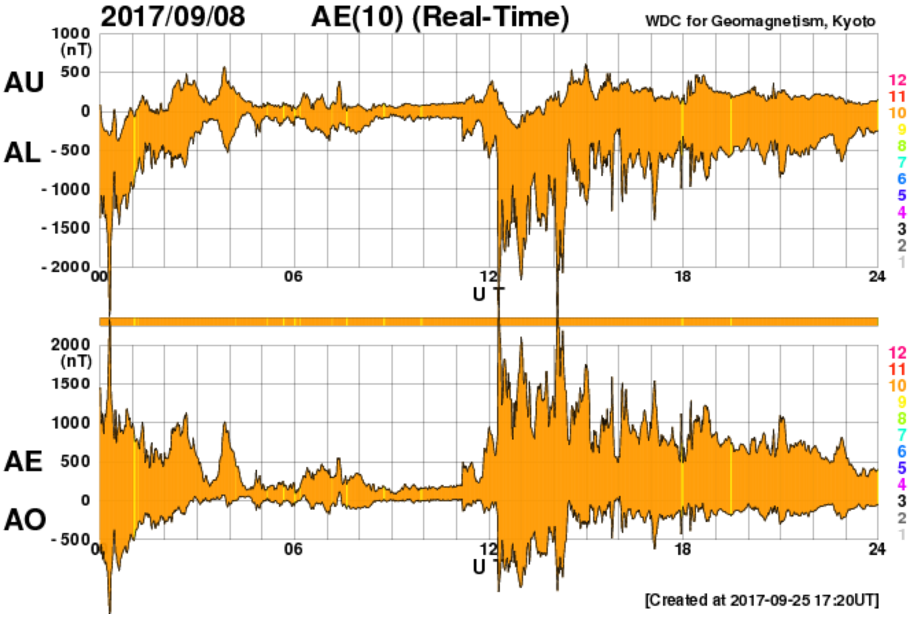

Figure 4.4.2: AE index time evolution during September 8, 2017. Credits: World Data Center for Geomagnetism, Kyoto.

ber, 2017. Using the VARION software we were able to estimate sTEC variations in real-time scenario and in real real-time (see section 5.3). At the moment of writing, we are working on a real-time strategy to filter out the storm effects from the sTEC time series .

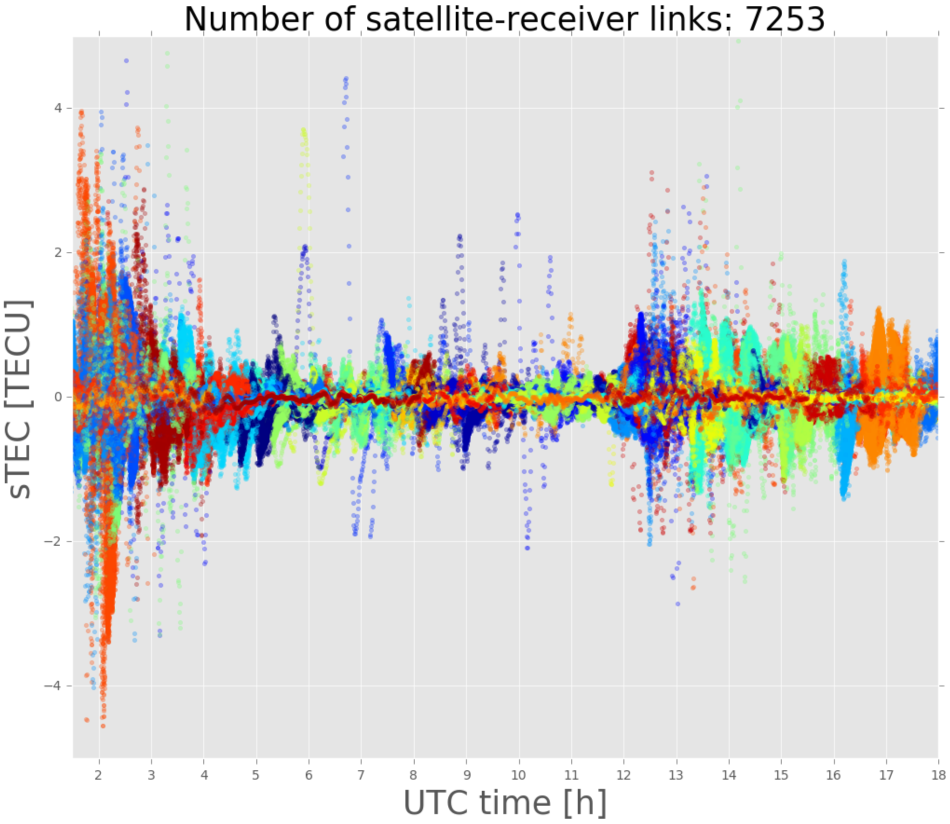

Figure 4.4.3: sTEC variations computed for 7253 satellite receiver links. sTEC variations increments during the pick times of the geomagnetic storm (around 01:00 UTC and 13:00 UTC) were clearly detected.

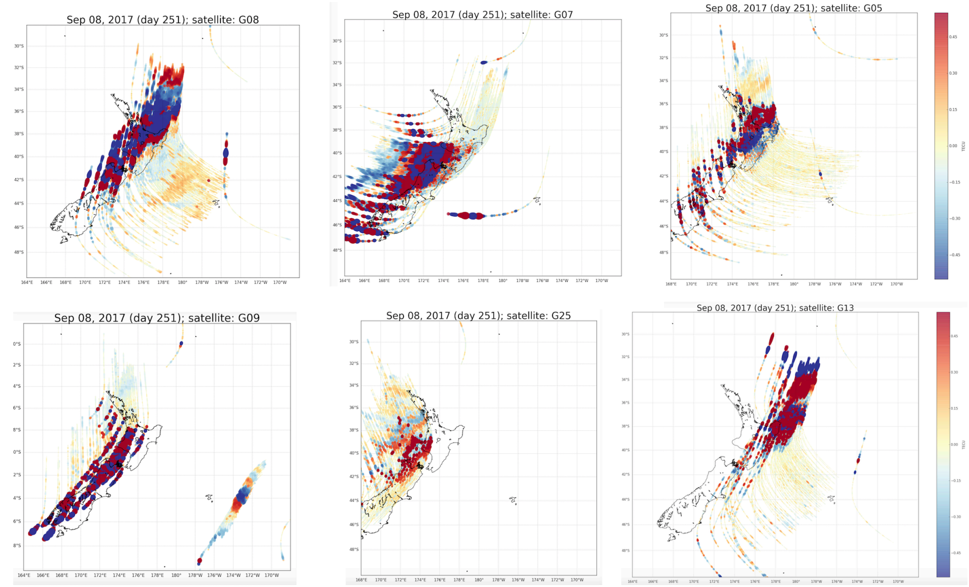

Figure 4.4.4: Space–time sTEC variations at the sIPs (same positions of the corresponding IPPs on the map) for 6 satellites seen from the 186 New Zealand GNSS permanent stations, during the geomagnetic storm. The sTEC variations (from positive to negative values and vice-versa) are clearly visible in the interval of significant. The maps have been generated using the matplotlib Basemap toolkit (Hunter, 2007 [37]).

Profound study of nature is the most fertile source of mathematical discoveries.

Joseph Fourier, The Analytical Theory of Heat (1878)

5

VARION Real-Time Implementation

Section 5.2 presents a real-time simulation based on the 2012 Haida Gwaii event. Section 5.1 deals with the real-time filtering aspect and the finite impulse response (FIR) digital filter is explained throughout this section. The last part of this chapter 5.3 presents our new effort, the VARION website, which uses the VARION algorithm (section 3.3) to process real-time streams of data provided by the global JPL's GDGPS system.

5.1 REAL-TIME DIGITAL FILTER

In the previous chapter 4, we attempted to prove the efficiency of a high-pass filter (polynomial fitting) using other post-processing techniques. In the true real-time case the polynomial fit has been implemented as a finite duration impulse response (FIR) digital filter [1, 51].

The term digital filter indicates a computational process, or algorithm, transforming a discrete sequence of numbers (the input) into another discrete sequence of numbers (the output) having a modified frequency domain spectrum. Any input discrete signals $\{x_n\}$ can be represent in the time or frequency domain using the Fourier direct/inverse transformations. A discrete signal can be seen as formed by multiplying a reference continuous signal with an ideal sampling function. The resulting spectrum is a scaled periodic version of the original spectrum. The scaling factor and the frequency domain repetition period are both the reciprocal of the sampling rate. These considerations lead to the Nyquist'sampling theorem: *if a continuous signal is multiplied by an ideal sampling function, them the signal can be recovered from the sampled version only if the original signal spectrum is enterally contained within a bandwidth of less than half the sampling rate.* This means that if we attempt to recover a signal which has not been sampled at a fast enough rate we will have aliasing.

The term finite impulse response arises because the filter output is computed as a weighted, finite term sum, of past and present (and perhaps future values) of the filter input

$$y_n = \sum_{k=M_1}^{M_2} (x_{n-k} h_k) \tag{5.1}$$

where both M_1 and M_2 are finite. One of the simplest FIR filters we may consider is a 3-term moving average filter of the form

$$y_n = \frac{1}{3}(x_{n+1} + x_n + x_{n-1}) \tag{5.2}$$

where h_k coefficients are all equal to 1/3.

An other important aspect of FIR filter is that it is based on a feed-forward difference equation (see Eqn. 5.3). This means that there is no feedback of past or future outputs to form the present output, just input related terms.

5.1.1 FINITE IMPULSE RESPONSE FILTER

This sections explains how it is possible to implement a FIR filter in order to filter samples in real-time.

Assuming we have a continuous signal which has been sampled in time with a certain sampled frequency f_s and we want to filter out some frequency components. One way would be to apply the fast Fourier transform algorithm to generate the signal spectrum and then multiply it by a filter (e.g. a boxcar function) to remove the unwanted frequencies. The output would be a portion of the original spectrum which can be inverted to generate the new filtered time series.

From Fourier theory we know that multiply in the frequency domain is the same of performing a convolution in time. FIR filter is just an efficient way to implement this convolution in the time domain.

Fig. 5.1.1 shows a input time series of samples flowing from the top (x_{n-k}). Implement the convolution means multiply each of these samples by some coefficients (h_k). This coefficients correspond to samples of the boxcar filter as seen in time domain, which corresponds to a $sinc(t)$ function. Subsequently, we integrate these products in the time domain. which for discrete time series, is a sum. The class of causal FIR filters has difference equation of the form

$$y_n = \sum_{k=0}^{M} (x_{n-k} h_k) \tag{5.3}$$

To deal with the convolution process it is necessary to slice one function by the other one in order to perform the product and the integration as a function of the separation between the two functions. In real-time application time does this work for us. As soon as a new sample flows from the left, all the other samples advance one to the right. The convolution is performed over each new sets of samples and the time series keep flowing from the left. In this way we filter the whole time series using the same filter coefficients (h_k).

In this work, a Python routine which optimize the FIR filtering process has been used.

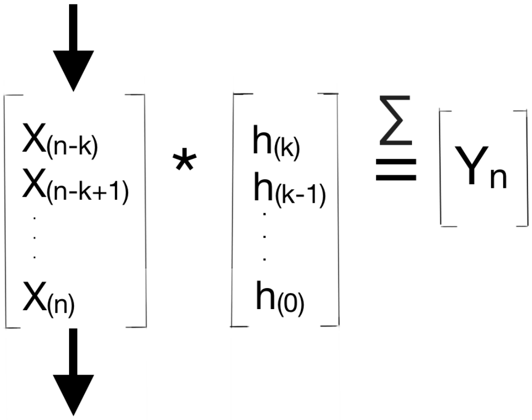

Figure 5.1.1: Schematic representation of the real-time FIR filter.

An important aspect to take into account is the number of coefficients necessary to implement the filter. This number is going to set some limits on the steepness of the filter. With only a finite number of coefficients to represent the filter in the time domain, a perfect brick wall filter with a flat pass band cannot be implemented. Instead, the real filter can have some roll-off around the cut-off frequency and ripples in the stop and/or pass band.

For our application, when using 1 Hz data, a FIR filter is designed with 2048 coefficients, which means an initial delay of 35 minutes ($2048/3600 * 60$). This period is called the transitory phase (TP). When TP ends, the system will proceed in a stationary phase (SP) and will provide continuous realtime estimates of TEC perturbations. This initial delay will not affect the reliability of the system because it occurs when the receiver starts tracking the particular satellite and this will not coincide with the beginning of the TID event.

The key implications of FIR filters this are that they are always stable, and have linear phase responses (as long as the filter's coefficients are symmetrical). This means that there is a constant change in output phase angle as a function of frequency. The resultant filter phase plot vs frequency is a straight line. As such, a linear phase filter's group delay is a constant. Linear phase filters preserve the integrity of the information-carrying signals but the output signal is shifted in time. The number of coefficients used to implement the filter will also determines the phase shift and so the time delay in the filtered signal. For a given filter order, FIR filters have a much more gradual transition region roll-off than digital IIR filters.

5.2 2012 Haida Gwaii Simulation

5.2.1 Introduction

This section describes how we are now able to detect tsunami-induced ionospheric disturbances using a real-time stream of carrier-phase measurements from a standalone GNSS receiver. To simulate the real-time stream of data for the Haida Gwaii event discussed in the section, we acquired L1 and L2 observations at 1 Hz and proceeded to run the VARION algorithm to obtain TEC variations between two consecutive epochs. The outputs are filtered using a FIR filter designed with 2048 coefficients (see section 5.1 for more details).

5.2.2 Results and Discussion

The two green horizontal lines represent the $\pm$ 5 sigma error (99.99994$\%$ confidence) using a "moving" window encompassing the previous 2000 epochs (at 1 Hz rate) of the sTEC time series. This approach demonstrates the real-time computation of the background noise level of sTEC variations. From 00:00 to 00:20 time stamps we show nominal noise levels within the 5 sigma error bound. Subsequently, between 00:20 and 00:40 time stamps we can clearly see the tsunami TIDs exceeding the 5 sigma threshold. After the tsunami passing, the background noise tends to relax back to the undisturbed noise level (as it was shown prior to tsunami arrival). The red time series in Video 2 displays the actual observations collected at station AHUP.

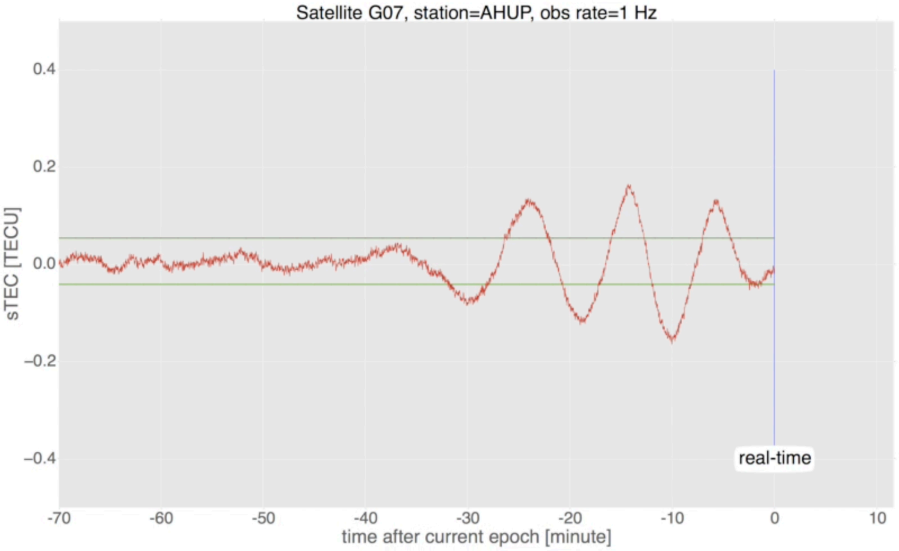

Figure 5.2.1: Real-time detection strategy applied for the 2012 Haida Gwaii Tsunami event. The red time series displays the integrated and filtered sTEC [TECU] values collected at station AHUP. The two green horizontal lines represent the 5 sigma threshold.

5.3 VARION Website

5.3.1 Introduction

Analyzing real-time satellite remote sensing data can be an intricate task. For instance, data gaps can be generated by several external factors (e.g. obstacles along the receiver-satellite line of site or loss of communication) and different noise sources at different locations may affect the observations. The VARION website (`https://iono2la.gdgps.net/`), a web-based tool, facilitates access, visualization and interaction with real-time GNSS ionospheric observations. In our vision, the VARION website will become an important tool for ionosphere monitoring and natural hazard detection. This new infrastructure is divided into three main real-time segments: the stream of GNSS observations, the estimation of line of slight or slant total electron content (sTEC) variations and the detection methodology. Each of these tasks is described in the next sections.

5.3.2 Real-Time Data Stream

The real-time stream of GNSS observations is provided by the JPL's Global Differential GPS (GDGPS) System, which is an extremely robust real-time GNSS monitoring and augmentation system. The 1 *Hz* data are down-sampled to 0.1 *Hz* to reduce the computational time. Different sampling rates may be chosen to detect different types of waves propagating in the ionosphere. We are currently processing 30 stations in real-time which correspond to more than 240 receiver-to-satellite links processed simultaneously.

5.3.3 Real-Time Processing

The real-time processing engine is based on the VARION algorithm (section 3.3). The space-and-time variations of sTEC and the ionospheric pierce points (IPPs) locations are computed in real-time. The sTEC time series are filtered using a digital filter (e.g., FIR filter) in order to analyze a specific portion of the spectrum. Ionospheric perturbations may be caused by a variety of phenomenon. Next section describes how we discern tsunami ionospheric disturbances from other sources of ionospheric disturbances.

5.3.4 REAL-TIME DETECTION METHOD

The real-time detection strategy is divided into three main tasks: first identify the earthquake location, then detect ionospheric anomalies exceeding a certain threshold values and lastly estimate the propagation properties of the ionospheric disturbances.

The earthquake information is continuously monitored from the USGS real-time GeoJSON feed (`https://earthquake.usgs.gov/earthquakes/feed/v1.0/geojson.php`). When a new earthquake appeared on the map, it will be possible to focus the detection on a specific region and visualize all the TEC time series, inspect the signal-to-noise ratio and check the integrity of the real-time solutions.

The second step is to define threshold values in the real-time solutions in order to detect the arrival times of the ionospheric disturbances at different locations. These thresholds will be computed independently for each satellite-receiver link. A 5-sigma level of confidence is computed on the first half part of the filtered sTEC time series. When gravity-wave-induced sTEC disturbances exceed this value, the arrival time will be recorded at that particular location.

As the system continues recording arrival times at several locations, the horizontal velocity of TIDs will be automatically estimated. This estimation will continuously be computed and it is expected to be more accurate as the time passes by. If the horizontal velocity of the TIDs will be $v_{tid} \approx \sqrt{gh}$, where g is the gravity mean value and h is the water depth at that location, a tsunami alert will be issued.

We are also investigating alternative ways to define the background noise using the sTEC time series. Since the GPS satellites have an orbital period of approximately 12 hours, every 24 hours each satellite-receiver link will sense the same portion of the ionosphere at the same local time (-4 min due to sidereal period of GPS orbits). Using this information, we will be able to filter out common noise sources between consecutive days. It is worth to mention that this approach cannot be used for other constellations (e.g. Galileo or GLONASS) which have different orbital periods.

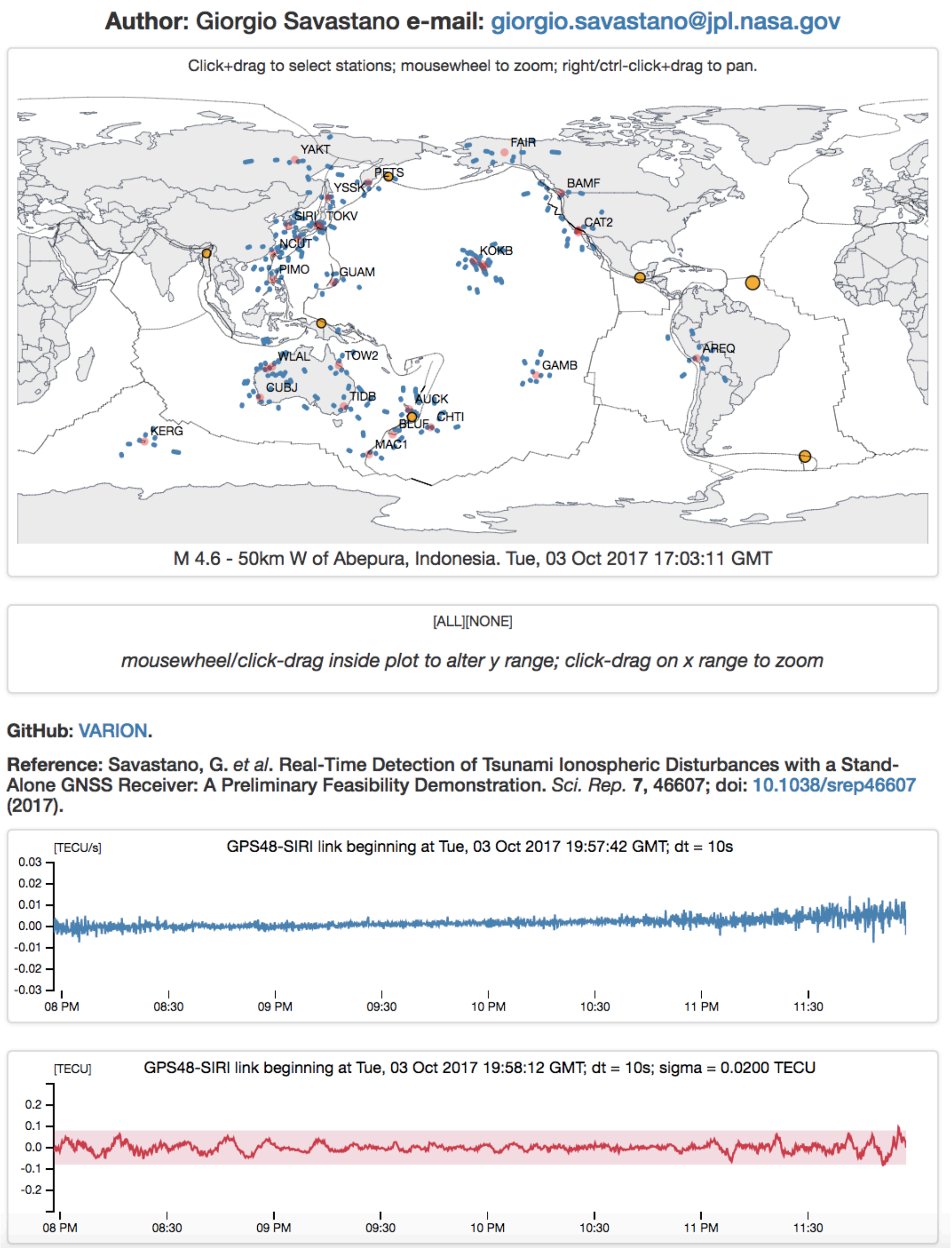

Author: Giorgio Savastano e-mail: giorgio.savastano@jpl.nasa.gov

Click+drag to select stations; mousewheel to zoom; right/ctrl-click+drag to pan.

M 4.6 - 50km W of Abepura, Indonesia. Tue, 03 Oct 2017 17:03:11 GMT

[ALL][NONE]

mousewheel/click-drag inside plot to alter y range; click-drag on x range to zoom

GitHub: VARION.

Reference: Savastano, G. *et al*. Real-Time Detection of Tsunami Ionospheric Disturbances with a Stand-Alone GNSS Receiver: A Preliminary Feasibility Demonstration. *Sci. Rep.* 7, 46607; doi: 10.1038/srep46607 (2017).

GPS48-SIRI link beginning at Tue, 03 Oct 2017 19:57:42 GMT; dt = 10s

GPS48-SIRI link beginning at Tue, 03 Oct 2017 19:58:12 GMT; dt = 10s; sigma = 0.0200 TECU

Figure 5.3.1: Prototype version of the VARION website. The real-time stream of data is continually processed using the VARION algorithm. The map shows the real-time estimated IPP locations. The blue time series represents the raw δTEC observations [TECU/s], the red time series displays the integrated and filtered TEC time series [TECU].

6

VARION and VADASE Contributions and Possible Evolutions

6.1 GNSS Tsunami Early Warning System

The real-time GNSS ionospheric measurement capability offered by VARION algorithm [81] can be consider an important step forward in the realization of accurate and cost effective tsunami early warning systems. In fact, in [81], we demonstrated the feasibility to use in real-time observations at middle to high elevations (e.g. Fig. 4.1.5), neglecting the contribution of the $\vec{V}_{ipp}$ with respect to the velocity of the tsunami (Eqn. 3.5).

The VARION algorithm implementation in the JPL's GDGPS was presented to the NASA funded GTEWS (GNSS Tsunami Early Warning System), July 25-27 2017 workshop held in Sendai, Japan.

There is still much work to be done to improve the accuracy and fidelity of this technique and to integrate this approach into a augmented tsunami warning system. In particular, we believe that extending this short-range model for low elevation angles and improving the related real-time filtering technique (FIR filter) would be a critical objective to detect natural hazards as far in advance as possible, and thereby reducing the time delay in the observations.

For this reason, next section 6.2 describes an extended sTEC observation model that will be use in future research activities to investigate:

1. use of observations from geostationary satellites
2. relationship between the *sTEC* observations and $\vec{V}_{ipp}$

6.2 EXTENDED sTEC OBSERVATION MODEL

In the frame of a linear theory, we need to consider Eqn. 3.5 in more detail and expand the *sTEC* variable into a background state $sTEC^b$ and a perturbation $sTEC^T$ caused by e.g., a tsunami. Eqn. 3.5 becomes:

$$\frac{d\,sTEC}{dt} = \frac{\partial sTEC^b}{\partial t} + \vec{V}_{ipp} \cdot \nabla sTEC^b + (\vec{V}_{ipp} - \vec{V}_T) \cdot \nabla sTEC^T \tag{6.1}$$

where $\vec{V}_T$ is the velocity of the ionospheric perturbation generated by a natural hazard. Our future goals will be to evaluate the contribution of the first and the second terms of the right-hand side of Eqn. 6.1, which represent the impact of the background ionospheric time-space variability in the *sTEC* observations, in order to remove these terms from the sTEC total derivative and to access the perturbation term due to the tsunami (or other natural hazards). In [81], we demonstrated the feasibility to use in real-time observations at middle to high elevations, neglecting the contribution of the $\vec{V}_{ipp}$ with respect to the velocity of the tsunami.

Section 3.4 describes the effects of the observation geometry in the *sTEC* observations. This aspect is crucial in order to compute in real time the term $\vec{V}_{ipp}$ ·

$\nabla sTEC^b$ of Eqn. 6.1, whose magnitude is significant below 40 degrees elevation angle. Section 3.4 also characterizes the correlation between the $\vec{V}_{ipp}$ magnitude and the $sTEC$ variations.

6.3 GNSS Seismology, Volcano Monitoring and Explosions Detection

As we have seen in chapter 2), the VADASE algorithm is capable to estimate in real-time ground velocities and displacements using stand-alone GNSS receivers, and for this reason it was eventually appointed as an effective strategy to contribute to GNSS seismology. For the 2015 Chile earthquake and tsunami Event (see Section 4.2), we have shown the benefits of using both VADASE and VARION approach in order to link in real-time the earthquake's ground shaking to the ionospheric perturbations.

Using a similar detection methodology, volcanic eruptions, geomagnetic storms, natural and man-made explosions will also be addressed in future studies. In fact, as discussed in Section 3.1, real-time GNSS monitoring of ionospheric dynamics through changes in Total Electron Content (TEC) could provide many important contributions to science and society because the ionosphere is strongly coupled to the dynamics of the Earth's surface, neutral atmosphere, and geomagnetic field.

References

[1] Bateman A. and W. Yates. *Digital Signal Processing Design*. Computer Science Press, Inc., 1989.

[2] J. Artru, P. Lognonne, and E. Blanc. Normal modes modelling of postseismic ionospheric oscillations. *Geophys. Res. Lett.*, 28, 2001. doi: 10.1029/2000GL000085. URL http://dx.doi.org/10.1029/2000GL000085.

[3] J. Artru, T. Farges, and P. Lognonné. Acoustic waves generated from seismic surface waves: propagation properties determined from doppler sounding observations and normal-mode modelling. *Geophys. J. Int.*, 158, 2004. doi: 10.1111/j.1365-246X.2004.02377.x. URL http://dx.doi.org/10.1111/j.1365-246X.2004.02377.x.

[4] Artru, J., V. Ducic, H. Kanamori, P. Lognonne, and M. Murakami. Ionospheric detection of gravity waves induced by tsunamis. *Geophys. J. Int.*, 20:840–848, 2005. doi: 10.1111/j.1365-246X.2005.02552.x. URL http://dx.doi.org/10.1111/j.1365-246X.2005.02552.x.

[5] Elvira Astafyeva and Kosuke Heki. Dependence of waveform of near-field coseismic ionospheric disturbances on focal mechanisms. *Earth, Planets and Space*, 61(7):939–943, Jul 2009. ISSN 1880-5981. doi: 10.1186/BF03353206. URL http://dx.doi.org/10.1186/BF03353206.

[6] Elvira Astafyeva, Kosuke Heki, Vladislav Kiryushkin, Edward Afraimovich, and Sergey Shalimov. Two-mode long-distance propagation of coseismic ionosphere disturbances. *Journal of Geophysical Research: Space Physics*, 114 (A10):n/a–n/a, 2009. ISSN 2156-2202. doi: 10.1029/2008JA013853. URL http://dx.doi.org/10.1029/2008JA013853. A10307.

[7] Hoffman-Wellenhof B., Lichtenegger H., and Wasle. *GNSS – Global Navigation Satellite Systems. GPS, GLONASS, Galileo and more*. Springer-Verlag, 2008.

[8] Kathleen Bailey, Christopher DiVeglio, and Ashley Welty. An examination of the june 2013 east coast meteotsunami captured by noaa observing systems. *NOAA Technical Report NOS CO-OPS 079*, 2014.

[9] Benedetti, E. et al. Global navigation satellite systems seismology for the 2012mw6.1 emilia earthquake: Exploiting the vadase algorithm. *Seism. Res. Lett.*, 85 no. 3:649–656, 2014. doi: 10.1785/0220130094. URL `http://dx.doi.org/10.1785/0220130094`.

[10] Bishop G., Walsh D., Daly P., Mazzella A., Holland E. Analysis of the temporal stability of GPS and GLONASS group delay correction terms seen in various sets of ionospheric delay data. *Proceedings of the 7th International Technical Meeting of the Satellite Division of The Institute of Navigation (ION GPS 1994)*, pages 1653–1661, 1994.

[11] G. Blewitt. 3.11 - GPS and Space-Based Geodetic Methods. In Gerald Schubert, editor, *Treatise on Geophysics (Second Edition)*, pages 307 – 338. Elsevier, Oxford, second edition edition, 2015. ISBN 978-0-444-53803-1. doi: https://doi.org/10.1016/B978-0-444-53802-4.00060-9. URL `https://www.sciencedirect.com/science/article/pii/B9780444538024000609`.

[12] Branzanti M., Colosimo G., Crespi M. and Mazzoni A. GPS near real-time coseismic displacements for the great Tohoku-Oki earthquake. *IEEE Geoscience and Remote Sensing Letters*, 2012. doi: 10.1109/LGRS.2012.2207704. URL `http://dx.doi.org/10.1109/LGRS.2012.2207704`.

[13] Maria Antonia Brovelli, Mattia Crespi, Francesca Fratarcangeli, Francesca Giannone, and Eugenio Realini. Accuracy assessment of high resolution satellite imagery orientation by leave-one-out method. *ISPRS Journal of Photogrammetry and Remote Sensing*, 63(4):427 – 440, 2008. ISSN 0924-2716. doi: https://doi.org/10.1016/j.isprsjprs.2008.01.006. URL `http://www.sciencedirect.com/science/article/pii/S0924271608000191`.

[14] Bosch W Brunini C, Meza A. Temporal and spatial variability of the bias between TOPEX- and GPS-derived total electron content. *J Geod*, 79, 2005. doi: 10.1007/s00190-005-0448-z. URL `http://dx.doi.org/10.1007/s00190-005-0448-z`.

[15] E. Calais and J. B. Minster. GPS, earthquakes, the ionosphere, and the space shuttle. *Phys. Earth Planet. Inter.*, 105, 1998. doi: 10.

1016/S0031-9201(97)00089-7. URL http://dx.doi.org/10.1016/S0031-9201(97)00089-7.

[16] Ciraolo L., Azpilicueta F., Brunini C., Meza A. and Radicella S.M. Calibration errors on experimental slant total electron content (tec) determined with GPS. *J Geodesy*, 2007. doi: 10.1007/s00190-006-0093-1. URL http://dx.doi.org/10.1007/s00190-006-0093-1.

[17] Coisson, P., P. Lognonne D. Walwer, and L. M. Rolland. First tsunami gravity wave detection in ionospheric radio occultation data. *Earth and Space Science*, 2:125–13, 2015. doi: 10.1002/2014EA000054. URL http://dx.doi.org/10.1002/2014EA000054.

[18] Colosimo G., Crespi M., and Mazzoni A. Real-time GPS seismology with a stand-alone receiver: A preliminary feasibility demonstration. *J. Geophys. Res.*, 116:B11 302, 2011. doi: 10.1029/2010JB007941. URL http://dx.doi.org/10.1029/2010JB007941.

[19] F. B. Daniels. Acoustic energy generated by ocean waves. *d. Acoust. Soc.*, 24: 83, 1952.

[20] Thomas Dautermann, Eric Calais, Philippe Lognonné, and Glen S. Mattioli. Lithosphere–atmosphere–ionosphere coupling after the 2003 explosive eruption of the soufriere hills volcano, montserrat. *Geophysical Journal International*, 179(3):1537–1546, 2009. ISSN 1365-246X. doi: 10.1111/j.1365-246X.2009.04390.x. URL http://dx.doi.org/10.1111/j.1365-246X.2009.04390.x.

[21] T. Neil Davis and Masahisa Sugiura. Auroral electrojet activity index ae and its universal time variations. *Journal of Geophysical Research*, 71(3):785–801, 1966. ISSN 2156-2202. doi: 10.1029/JZ071i003p00785. URL http://dx.doi.org/10.1029/JZ071i003p00785.

[22] V. Ducic, J. Artru, and P. Lognonne. Ionospheric remote sensing of the denali earthquake rayleigh surface waves. *Geophys. Res. Lett.*, 30, 2003. doi: 10.1029/2003GL017812. URL http://dx.doi.org/10.1029/2003GL017812.

[23] Calais E. and J. B. Minster. GPS detection of ionospheric perturbations following the january 17, 1994, northridge earthquake. *Geophys. Res. Lett.*, 22,

1995. doi: 10.1029/95GL00168. URL http://dx.doi.org/10.1029/95GL00168.

[24] Seeber G. *Satellite geodesy: foundations, methods, and applications, 2nd edition*. Walter de Gruyter, Berlin New York, 2003.

[25] Galileo. *European GNSS (Galileo) Open Service Signal-In-Space Interface Control Document Issue 1.3*. European Union, 2016.

[26] Galvan, D. A., A. Komjathy, M. P. Hickey, and A. J. Mannucci. The 2009 samoa and 2010 chile tsunamis as observed in the ionosphere using GPS total electron content. *J. Geophys. Res.*, 116:A06318, 2011. doi: 10.1029/2010JA016204. URL http://dx.doi.org/10.1029/2010JA016204.

[27] Galvan, D. A. et al. Ionospheric signatures of tohoku-oki tsunami of march 11, 2011: Model comparisons near the epicenter. *Radio Sci.*, 47:RS4003, 2012. doi: 10.1029/2012RS005023. URL http://dx.doi.org/10.1029/2012RS005023.

[28] GLONASS. *Global Navigation Satellite System GLONASS - Interface Control Document. Navigational radiosignal In bands L1, L2*. Russian Institute of Space Device Engineering, Moscow, 2008.

[29] GLONASS. *Global Navigation Satellite System GLONASS - Interface Control Document. General Description of Code Division Multiple Access Signal System*. Russian Institute of Space Device Engineering, Moscow, 2016.

[30] G. K. Hartmann and R. Leitinger. Range errors due to ionospheric and tropospheric effects for signal frequencies above 100 mhz. *Bulletin géodésique*, 58(2):109–136, Jun 1984. ISSN 1432-1394. doi: 10.1007/BF02520897. URL http://dx.doi.org/10.1007/BF02520897.

[31] K. Heki and J. Ping. Directivity and apparent velocity of the coseismic ionospheric disturbances observed with a dense gps array. *Earth Planet. Sci. Lett.*, 236, 2005. doi: 10.1016/j.epsl.2005.06.010. URL http://dx.doi.org/10.1016/j.epsl.2005.06.010.

[32] Toshiyuki Hibiya and Kinjiro Kajiura. Origin of the abiki phenomenon (a kind of seiche) in nagasaki bay. *Journal of the Oceanographical Society of Japan*, 38(3):172–182, 1982. ISSN 1573-868X. doi: 10.1007/BF02110288. URL https://doi.org/10.1007/BF02110288.

[33] Hickey, M. P., G. Schubert, and R. L. Walterscheid. Propagation of tsunami-driven gravity waves into the thermosphere and ionosphere. *J. Geophys. Res.*, 114:A08304, 2009. doi: 10.1029/2009JA014105. URL http://dx.doi.org/10.1029/2009JA014105.

[34] C. O. Hines. Internal atmospheric gravity waves at ionospheric heights. *Can. J. Phys.*, 38:14411481, 1960. doi: 10.1139/p60-150. URL http://dx.doi.org/10.1139/p60-150.

[35] C. O. Hines. Gravity waves in the atmosphere. *Nature*, 239:7378, 1972. doi: 10.1038/239073a0. URL http://dx.doi.org/10.1038/239073a0.

[36] Hung, R. J., T. Phan, and R. E. Smith. Observation of gravity waves during the extreme tornado outbreak of 3 april 1974. *J. Atmos. Terr. Phys.*, 40:831–843, 1978. doi: 10.1016/0021-9169(78)90033-8. URL http://dx.doi.org/10.1016/0021-9169(78)90033-8.

[37] J. D. Hunter. Matplotlib: A 2d graphics environment. *Computing In Science and Engineering*, 9(3):90–95, 2007. doi: 10.1109/MCSE.2007.55.

[38] Shuanggen Jin, Rui Jin, and D. Li. Gps detection of ionospheric rayleigh wave and its source following the 2012 haida gwaii earthquake. *Journal of Geophysical Research: Space Physics*, 122(1):1360–1372, 2017. ISSN 2169-9402. doi: 10.1002/2016JA023727. URL http://dx.doi.org/10.1002/2016JA023727.

[39] Jin, S., G. Occhipinti, R. Jin. Gnss ionospheric seismology: recent observation evidences and characteristics. *Earth-Science Reviews*, 147:54–64, 2015. doi: 10.1016/j.earscirev.2015.05.003. URL http://dx.doi.org/10.1016/j.earscirev.2015.05.003.

[40] JPO. *Navstar GPS Space Segment/ Navigation User Interfaces (IS-GPS-200), Revision D. Tech. rep.* GPS Navstar Joint Programme Office, El Segundo, CA, 2004.

[41] Kelley, M. C. In situ ionospheric observations of severe weather related gravity waves and associated small scale plasma structure. *J. Geophys. Res.*, 102:329–335, 1997. doi: 10.1029/96JA03033. URL http://dx.doi.org/10.1029/96JA03033.

[42] Kelley, M. C., R. Livingston, and M. McCready. Large amplitude thermospheric oscillations induced by an earthquake. *Geophys. Res. Lett.*, 12:577–580, 1985. doi: 10.1029/GL012i009p00577. URL `http://dx.doi.org/10.1029/GL012i009p00577`.

[43] Kherani E A, Lognonné P, Kamath N, Crespon F and Garcia R. Response of the ionosphere to the seismic trigerred acoustic waves: electron density and electromagnetic fluctuations. *Geophys. J. Int.*, 176:1–13, 2009. doi: 10.1111/j.1365-246X.2008.03818.x. URL `http://dx.doi.org/10.1111/j.1365-246X.2008.03818.x`.

[44] J. A. Klobuchar. Ionospheric time-delay algorithm for single-frequency GPS users. *IEEE Transactions on Aerospace and Electronic Systems*, AES-23(3): 325–331, May 1987. ISSN 0018-9251. doi: 10.1109/TAES.1987.310829. URL `http://dx.doi.org/10.1109/TAES.1987.310829`.

[45] A. Komjathy, D. A. Galvan, P. Stephens, M. D. Butala, V. Akopian, B. Wilson, O. Verkhoglyadova, A. J. Mannucci, and M. Hickey. Detecting ionospheric tec perturbations caused by natural hazards using a global network of gps receivers: The tohoku case study. *Earth, Planets and Space*, 64(12):24, Jan 2013. ISSN 1880-5981. doi: 10.5047/eps.2012.08.003. URL `http://dx.doi.org/10.5047/eps.2012.08.003`.

[46] Komjathy, A. et al. Review and perspectives: Understanding natural-hazards-generated ionospheric perturbations using GPS measurements and coupled modeling. *Radio Sci.*, 51:951–961, 2016. doi: 10.1002/2015RS005910. URL `http://dx.doi.org/10.1002/2015RS005910`.

[47] Komjathy, A., L. Sparks, B. D. Wilson, and A. J. Mannucci. Automated daily processing of more than 1000 ground-based GPS receivers for studying intense ionospheric storms. *Radio Sci.*, 40:RS6006, 2005. doi: 10.1029/2005RS003279. URL `http://dx.doi.org/10.1029/2005RS003279`.

[48] Lee, M. C. et al. Did tsunami-launched gravity waves trigger ionospheric turbulence over Arecibo? *J. Geophys. Res.*, 113:A01302, 2008. doi: 10.1029/2007JA012615. URL `http://dx.doi.org/10.1029/2007JA012615`.

[49] Haitao Liu, Feng Ding, Biqiang Zhao, Jianyong Li, Lianhuan Hu, Weixing Wan, and Baiqi Ning. Ionospheric response following the mw 7.8 gorkha earthquake on 25 april 2015. *Journal of Geophysical Research: Space Physics*,

2017. ISSN 2169-9402. doi: 10.1002/2016JA023079. URL http://dx.doi.org/10.1002/2016JA023079.

[50] F.K. Lutgens and E.J. Tarbuck. *The Atmosphere: An Introduction to Meteorology*. Pearson, 2013. ISBN 9780321756312. URL https://books.google.com/books?id=C5pJYAAACAAJ.

[51] Bellanger M. *Digital Processing of Signals: Theory and Practice*. John Wiley & Sons, 1984.

[52] Ross S. M. *Introduction to probability and statistics for engineers and scientists*. Academic Press, 2014.

[53] Mai, C.-L., and J.-F. Kiang. Modeling of ionospheric perturbation by 2004 sumatra tsunami. *Radio Sci.*, 44:RS3011, 2009. doi: 10.1029/2008RS004060. URL http://dx.doi.org/10.1029/2008RS004060.

[54] Mannucci, A. J. et al. A global mapping technique for GPS derived ionospheric total electron content measurements. *Radio Sci.*, 33:565–582, 1998. doi: 10.1029/97RS02707. URL http://dx.doi.org/10.1029/97RS02707.

[55] Mannucci, A. J. et al. GPS—based remote sensing of the geospace environment: Horizontal and vertical structure of the ionosphere and plasmasphere. *Proc. SPIE Int. Soc. Opt. Eng.*, 5660:1–13, 2004. doi: 10.1117/12.580048. URL http://dx.doi.org/10.1117/12.580048.

[56] Meng, X. et al. A new physics-based modeling approach for tsunami-ionosphere coupling. *Geophys. Res. Lett.*, 42:4736–4744, 2015. doi: 10.1002/2015GL064610. URL http://dx.doi.org/10.1002/2015GL064610.

[57] Doug Mercer, Jinyu Sheng, Richard Greatbatch, and Joško Bobanović. Barotropic waves generated by storms moving rapidly over shallow water. *Journal of Geophysical Research*, 107, 10 2002. doi: 10.1029/2001JC001140. URL http://dx.doi.org/10.1029/2001JC001140.

[58] Sebastià Monserrat, Climent Ramis, and Alan J. Thorpe. Large amplitude pressure oscillations in the western mediterranean. 18, 02 1991. doi: 10.1029/91GL00234. URL http://dx.doi.org/10.1029/91GL00234.

[59] Sebastià Monserrat, Ivica Vilibić, and Alexander Rabinovich. Meteotsunamis: Atmospherically induced destructive ocean waves in the tsunami frequency band. *Natural hazards and earth system sciences*, 03 2006.

[60] O. Montenbruck and E. Gill. *Satellite orbits: models, methods and applications*. Springer, 2000.

[61] Nicolls, M. J., M. C. Kelley, A. J. Coster, S. A. González, and J. J. Makela. Imaging the structure of a large scale tid using isr and tec data. *Geophys. Res. Lett.*, 31:L09812, 2004. doi: 10.1029/2004GL019797. URL http://dx.doi.org/10.1029/2004GL019797.

[62] Giovanni Occhipinti, Lucie Rolland, Philippe Lognonné, and Shingo Watada. From sumatra 2004 to tohoku-oki 2011: The systematic gps detection of the ionospheric signature induced by tsunamigenic earthquakes. *Journal of Geophysical Research: Space Physics*, 118(6):3626–3636, 2013. ISSN 2169-9402. doi: 10.1002/jgra.50322. URL http://dx.doi.org/10.1002/jgra.50322.

[63] Occhipinti, G., E. A. Kherani, and P. Lognonné. Geomagnetic dependence of ionospheric disturbances induced by tsunamigenic internal gravity waves. *Geophys. J. Int.*, 73:753765, 2008. doi: 10.1111/j.1365-246X.2008.03760.x. URL http://dx.doi.org/10.1111/j.1365-246X.2008.03760.x.

[64] Occhipinti, G. et al. Three-dimensional numerical modeling of tsunami-related internal gravity waves in the hawaiian atmosphere. *Earth Planets Space*, 63 (7):847–851, 2011.

[65] Occhipinti, G., P. Lognonné, E. A. Kherani, and H. Hbert. Threedimensional waveform modeling of ionospheric signature induced by the 2004 sumatra tsunami. *Geophys. Res. Lett.*, 33:L20104, 2006. doi: 10.1029/2006GL026865. URL http://dx.doi.org/10.1029/2006GL026865.

[66] Emile A. Okal. Seismic parameters controlling far-field tsunami amplitudes: A review. *Natural Hazards*, 1(1):67–96, 1988. ISSN 1573-0840. doi: 10.1007/BF00168222. URL https://doi.org/10.1007/BF00168222.

[67] Queney P. The problem of airflow over mountains. a summary of theoretical studies. *Bulletin of the American Meteorological Society*, (29):16–26, 1948.

[68] Peltier, W. R., and C. O. Hines. On the possible detection of tsunamis by a monitoring of the ionosphere. *J. Geophys. Res.*, 81 12:1995–2000, 1976.

[69] Percival, D.B. et al. Extraction of tsunami source coefficients via inversion of DART® buoy data. *Nat. Hazards*, 58 1:567–590, doi:10.1007/s11069–010–9688–1, 2011.

[70] Teukolsky S. A. Vetterling W. T. Press, W. H. and B. P. Flannery. *Numerical Recipes in C*. 2nd ed. Cambridge university press, 1992.

[71] J. Proudman. The effects on the sea of changes in atmospheric pressure. *Geophysical Journal International*, 2:197–209, 1929. ISSN 1365-246X. doi: 10.1111/j.1365-246X.1929.tb05408.x. URL http://dx.doi.org/10.1111/j.1365-246X.1929.tb05408.x.

[72] Holton J. R. *An Introduction to Dynamic Meteorology*. New York: Academic Press, 1992.

[73] Lionel Renault, Guillermo Vizoso, Agustin Jansá, John Wilkin, and Joaquin Tintoré. Toward the predictability of meteotsunamis in the balearic sea using regional nested atmosphere and ocean models. *Geophysical Research Letters*, 38(10), 2011. ISSN 1944-8007. doi: 10.1029/2011GL047361. URL http://dx.doi.org/10.1029/2011GL047361.

[74] Richmond, A. D., and S. Matsushita. Thermospheric response to a magnetic substorm. *J. Geophys. Res.*, 80:2839–2850, 1975. doi: 10.1029/JA080i019p02839. URL http://dx.doi.org/10.1029/JA080i019p02839.

[75] Lucie M. Rolland, Philippe Lognonné, Elvira Astafyeva, E. Alam Kherani, Naoki Kobayashi, Michèle Mann, and Hiroshi Munekane. The resonant response of the ionosphere imaged after the 2011 off the pacific coast of tohoku earthquake. *Earth, Planets and Space*, 63(7):62, Sep 2011. ISSN 1880-5981. doi: 10.5047/eps.2011.06.020. URL http://dx.doi.org/10.5047/eps.2011.06.020.

[76] Lucie M. Rolland, Philippe Lognonné, and Hiroshi Munekane. Detection and modeling of rayleigh wave induced patterns in the ionosphere. *Journal of Geophysical Research: Space Physics*, 116(A5), 2011. ISSN 2156-2202. doi: 10.1029/2010JA016060. URL http://dx.doi.org/10.1029/2010JA016060.

[77] Rolland, L. M., G. Occhipinti, P. Lognonné, and A. Loevenbruck. Ionospheric gravity waves detected offshore hawaii after tsunamis. *Geophys.*

Res. Lett., 37:L17101, 2010. doi: 10.1029/2010GL044479. URL http://dx.doi.org/10.1029/2010GL044479.

[78] Watada S. *Near-source acoustic coupling between the atmosphere and the solid earth during volcanic eruptions*. PhD Thesis California Institute of Technology, Pasadena, CA, 1995.

[79] Rius A. Sardon E. and N. Zarraoa. Estimation of the transmitter and receiver differential biases and the ionospheric total electron content from global positioning system observations. *Radio Sci*, 29:577–586, 1994.

[80] Zarraoa N Sardon E, Rius A. *Tsunami forecasting*, volume 15 of *Tsunamis*, chapter 12, page 371–400. Harvard University Press, Cambridge, MA and London, England, 2009.

[81] Giorgio Savastano, Attila Komjathy, Olga Verkhoglyadova, Augusto Mazzoni, Mattia Crespi, Yong Wei, and Anthony J. Mannucci. Real-time detection of tsunami ionospheric disturbances with a stand-alone gnss receiver: A preliminary feasibility demonstration. *Sci. Rep.*, 7:46607, 2017. URL http://dx.doi.org/10.1038/srep46607.

[82] Ksenia Shults, Elvira Astafyeva, and Sévan Adourian. Ionospheric detection and localization of volcano eruptions on the example of the april 2015 calbuco events. *Journal of Geophysical Research: Space Physics*, 121(10):10,303–10,315, 2016. ISSN 2169-9402. doi: 10.1002/2016JA023382. URL http://dx.doi.org/10.1002/2016JA023382.

[83] Mike Stewart and Maria Tsakiri. GLONASS broadcast orbit computation. *GPS Solutions*, 2(2):16–27, Oct 1998. ISSN 1080-5370. doi: 10.1007/PL00000032. URL https://doi.org/10.1007/PL00000032.

[84] Makoto Tahira. Acoustic resonance of the atmospheric at 3.7 hz. *Journal of the Atmospheric Sciences*, 52(15):2670–2674, 1995. doi: 10.1175/1520-0469(1995)052<2670:AROTAA>2.0.CO;2. URL https://doi.org/10.1175/1520-0469(1995)052<2670:AROTAA>2.0.CO;2.

[85] Tang, L., V.V. et al. Direct energy estimation of the 2011 japan tsunami using deep-ocean pressure measurements. *J. Geophys. Res.*, 117:C08008, 2012. doi: 10.1029/2011JC007635. URL http://dx.doi.org/10.1029/2011JC007635.

[86] Titov, V.V. et al. Real-time tsunami forecasting: Challenges and solutions. *Nat. Hazards*, 35(1):41–58, 2005.

[87] C. Torrence and G. P. Compo. A practical guide to wavelet analysis. *Bull. Amer. Meteor. Soc.*, 79:6178, 1998.

[88] Tsugawa, T., Y. Otsuka, A. J. Coster, and A. Saito. Medium scale traveling ionospheric disturbances detected with dense and wide tec maps over north america. *Geophys. Res. Lett.*, 34:L22101, 2007. doi: 10.1029/2007GL031663. URL http://dx.doi.org/10.1029/2007GL031663.

[89] Ivica Vilibić. Numerical simulations of the proudman resonance. *Continental Shelf Research*, 28(4):574 – 581, 2008. ISSN 0278-4343. doi: https://doi.org/10.1016/j.csr.2007.11.005. URL http://www.sciencedirect.com/science/article/pii/S027843430700310X.

[90] S.N. Ward. Relationships of tsunami generation and an earthquake source. *J. Phys. Earth*, 28:441–474, 1980.

[91] Wei, Y., C. Chamberlin, V. Titov, L. Tang, and E.N. Bernard. Modeling of the 2011 japan tsunami - lessons for near-field forecast. *Pure Appl. Geophys.*, 170(6–8):1309–1331, 2013. doi: 10.1007/s00024-012-0519-z. URL http://dx.doi.org/10.1007/s00024-012-0519-z.

[92] Wei, Y. et al. Real-time experimental forecast of the peruvian tsunami of august 2007 for u.s. coastlines. *Geophys. Res. Lett.*, 35:L04609, 2008. doi: 10.1029/2007GL032250. URL http://dx.doi.org/10.1029/2007GL032250.

[93] Xiao, Z., S. Xiao, Y. Hao, and D. Zhang. Morphological features of ionospheric response to typhoon. *J. Geophys. Res.*, 112:A04304, 2007. doi: 10.1029/2006JA011671. URL http://dx.doi.org/10.1029/2006JA011671.

[94] Yang, Y.-M. et al. Tohoku-oki earthquake caused major ionospheric disturbances at 450 km altitude over alaska. *Radio Sci.*, 49:1206–1213, 2014. doi: 10.1002/2014RS005580. URL http://dx.doi.org/10.1002/2014RS005580.

[95] Yang, Y.-M. et al. The 2013 chelyabinsk meteor ionospheric impact studied using GPS measurements. *Radio Sci.*, 49:341350, 2014. doi: 10.1002/2013RS005344. URL http://dx.doi.org/10.1002/2013RS005344.

Colophon

This thesis was typeset using LaTeX, originally developed by Leslie Lamport and based on Donald Knuth's TeX. The body text is set in 11 point Arno Pro, designed by Robert Slimbach in the style of book types from the Aldine Press in Venice, and issued by Adobe in 2007. A template, which can be used to format a PhD thesis with this look and feel, has been released under the permissive MIT (X11) license, and can be found online at github.com/suchow/ or from the author at suchow@post.harvard.edu.